The murine meninges acquire lymphoid tissue properties and harbour autoreactive B cells during chronic *Trypanosoma brucei* infection

Juan F. Quintana[1-3*], Matthew C. Sinton[1,4], Praveena Chandrasegaran[3], Lalit Kumar Dubey[5], John Ogunsola[3], Moumen Al Samman[3], Michael Haley[1,2], Gail McConnell[6], Nono-Raymond Kuispond Swar[7], Dieudonne Mumba Ngoyi[7], David Bending[8], Luis de Lecea[9], Annette MacLeod[3], Neil A. Mabbott[10]

[1]Lydia Becker Institute of Immunology and Inflammation, University of Manchester, UK. [3]Division of Immunology, Immunity to Infection and Health, Manchester Academic Health Science Centre, University of Manchester, UK. [3]School of Biodiversity, One Health, Veterinary Medicine (SBOHVM), College of Medical, Veterinary and Life Sciences, University of Glasgow, Glasgow UK. [4]Division of Cardiovascular Sciences, University of Manchester, UK. [5]Queen Mary University of London, London, UK. [6]Strathclyde Institute of Pharmacy and Biomedical Sciences (SIPBS), University of Strathclyde, Glasgow, UK. [7]Department of Parasitology, National Institute of Biomedical Research, Kinshasa, Democratic Republic of the Congo. [8]Institute of Immunology and Immunotherapy, College of Medical and Dental Sciences, University of Birmingham. [9]Stanford University School of Medicine, Stanford, CA, United States.[10]The Roslin Institute and Royal (Dick) School of Veterinary Studies, University of Edinburgh, Edinburgh, UK.

[*]Corresponding author: juan.quintana@glasgow.ac.uk

Keywords: sleeping sickness, African trypanosomes, neuroinflammation, meninges, fibroblasts.

Running title: Functional characterisation of the murine meninges during chronic *Trypanosoma brucei* infections

Abstract

The meningeal space is a critical brain structure providing immunosurveillance for the central nervous system, but the impact of infections on the meningeal immune landscape is far from being fully understood. The extracellular protozoan parasite *Trypanosoma brucei*, which causes Human African Trypanosomiasis (HAT) or sleeping sickness, accumulates in the meningeal spaces, ultimately inducing severe meningitis and resulting in death if left untreated. Thus, sleeping sickness represents an attractive model to study immunological dynamics in the meninges during infection. Here, by combining single cell transcriptomics and mass cytometry by time of flight (CyTOF) with *in vivo* interventions, we found that chronic *T. brucei* infection triggers the development of ectopic lymphoid aggregates (ELAs) in the murine meninges. These infection-induced ELAs were defined by the presence of ER-TR7^{+} fibroblastic reticular cells, CD21/35^{+} follicular dendritic cells, CXCR5^{+} PD1^{+} T follicular helper-like phenotype, GL7^{+} CD95^{+} GC-like B cells, and plasmablasts/plasma cells. Furthermore, the B cells found in the infected meninges produced high-affinity autoantibodies able to recognise mouse brain antigens, in a process dependent on LTβ signalling. A mid-throughput screening identified several host factors recognised by these autoantibodies, including myelin basic protein (MBP), coinciding with cortical demyelination and brain pathology. In humans, we identified the presence of autoreactive IgG antibodies in the cerebrospinal fluid of second stage HAT patients that recognised human brain lysates and MBP, consistent with our findings in experimental infections. Lastly, we found that the pathological B cell responses we observed in the meninges required the presence of *T. brucei* in the CNS, as suramin treatment before the onset of the CNS stage prevented the accumulation of GL7^{+} CD95^{+} GC-like B cells and brain-specific autoantibody deposition. Taken together, our data provide evidence that the meningeal immune response during chronic *T. brucei* infection results in the acquisition of lymphoid tissue-like properties, broadening our understanding of meningeal immunity in the context of chronic infections. These findings have wider implications for understanding the mechanisms underlying the formation ELAs during chronic inflammation resulting in autoimmunity in mice and humans, as observed in other autoimmune neurodegenerative disorders, including neuropsychiatric lupus and multiple sclerosis.

Introduction

The meningeal space is rapidly being recognised as a critical site for immunological responses in the central nervous system (CNS) under homeostasis[1–3], aging[4], and as a consequence of insults such as traumatic brain injury[5] and infection[6–8]. The extracellular protozoan parasite *Trypanosoma brucei*, which causes human African trypanosomiasis (HAT; sleeping sickness in humans) and animal African trypanosomiasis (Nagana in domestic animals) accumulates in the CNS and meningeal spaces triggering severe meningitis[9,10]. This culminates in the development of a wide range of debilitating neurological disorders[9,11–13]. These symptoms are diverse and include fatigue, altered sleep and circadian patterns, tremors, motor weakness, epilepsy, paralysis of one or more extremities, and Parkinson-like abnormal body movements[14–16]. Consistent with clinical data from humans, experimental trypanosomiasis in mice also results in chronic infection, leading to altered behaviour[17–20]. Thus, murine infection with *T. brucei* is a useful model to investigate meningeal responses to infection.

Chronic inflammatory processes are known to result in the formation of ectopic lymphoid aggregates (ELAs)[21–24]. Indeed, ELAs have been reported in a wide range of autoimmune disorders, including those affecting the CNS such as neuropsychiatric lupus[25] and multiple sclerosis[26]. The diverse cytokine and chemokine repertoire found in chronically inflamed tissues, including lymphotoxin-α/-β (LTα and LTβ) and CXCL13, help to the create interactive niches needed to generate such structures[21–24]. Stromal LTβ receptor (LTβR) signalling is important in generating the microarchitecture required for efficient antigen presentation and follicle organisation, which typically includes collagen-rich reticular cords that serve as channels for cellular trafficking, immunological synapses, and B cell affinity maturation[27]. Similarly, CXCL13 is an important chemokine for defining local gradients controlling B cell domains, typically in proximity to follicular dendritic cells (FDCs) and $CD4^+$ T follicular helper cells (T_{FH}) inducing the formation of germinal centres (GC), in which B cells undergo affinity maturation and somatic hypermutation to generate high affinity antibodies[21,23,25]. These reactions are typically restricted to secondary lymphoid organs such as the spleen and lymph nodes, but can occur ectopically in response to chronic inflammation, and may result in pathological consequences such as the formation of autoreactive antibodies, as recently described for multiple sclerosis and neuropsychiatric lupus[23,25,26,28].

104 In secondary lymphoid organs, including the spleen and lymph nodes, lymphatic vessels
105 act as conduits for the transport of tissue-derived antigens and dendritic cells to lymph
106 nodes, where naïve and memory T cells are optimally positioned for the detection of their
107 cognate antigen[29–31]. Similarly, immune complexes can be acquired by macrophages in
108 the subcapular space in lymph nodes and transferred directly to FDCs and B cells[32].
109 However, several key findings in recent years have led to a better understanding of the
110 role of lymphatic vessels in the dura mater layer of the meninges. For instance, the
111 meningeal lymphatic vessels can convey macromolecular complexes and immune cells
112 from the meninges and cerebrospinal fluid (CSF) to the deep cervical lymph nodes[4,33,34].
113 However, it is also plausible that extramedullary reactions may take place locally in the
114 meningeal spaces and brain borders, as reported recently in neuropsychiatric lupus[25] and
115 multiple sclerosism[28]. Whether the same extramedullar immunological reactions in the
116 brain and/or meninges, reminiscent of those taking place in secondary lymphoid tissues,
117 can be triggered by chronic, unresolved infections is uncertain.
118 Here, we investigated how the meningeal transcriptional environment is altered during *T.*
119 *brucei* infection, using a combination of single cell transcriptomics and mass cytometry
120 by time-of-flight (CyTOF). We found that chronic *T. brucei* infection in the meningeal
121 space results in a broad rearrangement of the immune landscape in the murine
122 meninges, with a significant increase in the frequency of innate (mononuclear phagocytes
123 and granulocytes) and adaptive (T, NKT, and B cells) immune cells. Furthermore, we
124 identified a population of autoreactive B cells in the meningeal spaces, including the
125 leptomeninges. These autoreactive B cels were able to recognise mouse brain antigens
126 and deposit high-affinity IgG antibodies in several brain areas including the hippocampus
127 and cortex, and this deposition was associated with cortical and white mater
128 demyelination. We also detected significant levels of autoreactive IgM and IgG antibodies
129 in the cerebrospinal fluid of HAT patients with inflammatory encephalopathy.
130 Furthermore, using a targeted screening approach we identified myelin basic protein as
131 one of the host antigens detected by autoreactive IgG antibodies in mouse serum and
132 human CSF collected during the chronic stage of the infection. Taken together, this study
133 demonstrates that the meningeal landscape acquires lymphoid tissue-like properties
134 resulting in the formation of autoreactive B cells. These results imply that the chronic
135 brain inflammation induced by African trypanosomes results in an autoimmune disorder
136 affecting the brain as observed in other neurological disorders of unknown aetiology such
137 as neuropsychiatric lupus and multiple sclerosis. We anticipate that the data presented

138 here will pave the way to understanding how chronic meningitis results in impaired
139 peripheral tolerance and the development of autoimmunity in the context of chronic
140 infections.

141 **Materials and methods**

142 **Ethical statement.** All animal experiments were approved by the University of Glasgow
143 Ethical Review Committee and performed in accordance with the Home Office guidelines,
144 UK Animals (Scientific Procedures) Act, 1986 and EU directive 2010/63/EU. All
145 experiments were conducted under SAPO regulations and UK Home Office project
146 licence number PP4863348 to Annette Macleod. The *in vivo* work presented in this study
147 was conducted at 30-days post-infection (dpi) and correlated with increased clinical
148 scores and procedural severity. The archived human CSF samples from gambiense HAT
149 patients from North Uganda used in this study were collected by Professor Wendy Bailey
150 (Liverpool School of Tropical Medicine, UK). Ethical approval was given to Prof. Bailey
151 by the Liverpool School of Tropical Medicine, UK, for sample collection and patients were
152 provided with a written consent. We received ethical approved by the University of
153 Glasgow MVLS Ethics Committee for Non-Clinical Research Involving Human Subjects
154 (Reference no. 200120043) for the use of human archived samples. The CSF from
155 healthy donors was obtained from the University of Edinburgh Brain and Tissue Bank
156 and received ethical approval from the University of Edinburgh (REC 21/ES/0087).

157 **Murine infections with *Trypanosoma brucei*.** Six- to eight-week-old female C57BL/6J
158 mice (JAX, stock 000664) and C57BL/6-Tg(Nr4a1-EGFP/Cre)820Khog/J strain, also
159 known as Nur77^{GFP} reporter mice (JAX, stock 016617), or the Nur77^{Tempo} reporter mouse
160 line (kindly provided by Dr. David Bending), were inoculated by intra-peritoneal injection
161 with ~2 x 10^3 parasites of strain *T. brucei brucei* Antat 1.1E[35]. Parasitaemia was
162 monitored by regular sampling from tail venesection and examined using phase
163 microscopy and the rapid "matching" method[36]. Uninfected mice of the same strain, sex
164 and age served as uninfected controls. Mice were fed *ad libitum* and kept on a 12 h light–
165 dark cycle. All the experiments were conducted between 8h and 12h. When using the
166 *Nur77*^{GFP} or the *Nur77*^{Tempo} reporter mice, sample acquisition and analysis was
167 conducted without *ex vivo* stimulation to preserve the TCR-dependent fluorescent
168 reporter signal found in the tissue. For sample collection, we focussed on 30 days post-
169 infection, as this has previously been shown to correlate with parasite infiltration in the
170 epidural space[10,11]. Culture-adapted *T. brucei* Antat 1.1E whole cell lysates were
171 prepared as followed. Parasites were cultured in HMI-9 supplemented with 10% FBS and

172 1% Penicillin/Streptomycin were grown at 37°C and 5% CO_2 and harvested during the
173 log phase. The parasites were harvested by centrifugation (800 g for 10 min at 4°C),
174 washed three times in 1X PBS (Gibco) supplemented with cOmplete protease Inhibitor
175 cocktail (Roche), and sonicated with 5 pulses of 10 seconds each. The resulting lysate
176 was cleared by centrifugation (3,000g for 10 min at 4°C to remove cell debris), and the
177 protein concentration of the cleared supernatant was measured using the Qubit protein
178 kit (Thermo) and kept at -80°C until usage for ELISPOT and ELISA. For LTBR-Ig
179 treatment, mice were inoculated with 1μg/μL of either LTBR-Ig or IgG2a i.p. (100
180 μl/mouse) for four consecutive days prior to infection, and then every seven days post-
181 infection until culling. Preparation of single cell suspension from skull meninges for single-
182 cell RNA sequencing
183 **Tissue processing and preparation of single cell suspension.** Single-cell
184 dissociations for scRNAseq experiments were performed as follow. Animals were
185 infected for 30 days (*n* = 2 mice/pool, 2 independent pools per experimental condition),
186 after which skullcap meninges were harvested for preparation of single cell suspensions.
187 Uninfected animals were also included as naive controls (*n* = 3 mice/pool, 2 pools
188 analysed). Briefly, all mice were killed by rapid decapitation following isoflurane
189 anaesthesia, within the same time (between 7:00 and 9:00 AM). To discriminate
190 circulating versus brain-resident immune cells, we performed intravascular staining of
191 peripheral $CD45^+$ immune cells, as previously reported[37]. Briefly, a total of 2 μg of anti-
192 CD45-PE antibody (in 100 μl of 1X PBS) was injected intravenously 3 minutes prior
193 culling. Mice were euthanised as described above and transcardially perfused with ice-
194 cold 0.025% (wt/vol) EDTA in 1X PBS. The excised meninges were enzymatically
195 digested with Collagenase P (1 mg/ml) and DNAse I (1 mg/ml; Sigma) in 1X PBS (HSBB)
196 (Invitrogen) for ~30 min at 37 °C. Single-cell suspensions were passed through 70 μm
197 nylon mesh filters to remove any cell aggregates, and the circulating $CD45\text{-}PE^+$ cells
198 were removed from the single cell suspension using magnetic sorting with anti-PE
199 microbeads (Miltenyi Biotec) according to manufacturer's recommendations (**S1A**
200 **Figure**).
201 **Mass cytometry sample processing**
202 Single cell suspension from meninges were prepared as described above and
203 resuspended in Dubecco's Modified Eagle Medium (DMEM) to a concentration of 1 x 10^6
204 cells/mL. Cells were activated for 6 h in a round-bottom 96-well plate using Cell Activation

205 Cocktail (containing with Brefeldin A) (BioLegend, San Diego, USA) as per the
206 manufacturer's recommendations. Plates were then centrifuged at 300 x g for 5 min and
207 the pellets resuspended in 50 µL of Cell-ID™ Cisplatin-195Pt viability reagent (Standard
208 BioTools, San Francisco, USA), and incubated at room temperature for 2 min. Cells were
209 washed twice in Maxpar® Cell Staining Buffer (Standard BioTools, San Francisco, USA),
210 and centrifuged at 300 x g at room temperature for 5 min. The CD16/CD32 receptors
211 were then blocked by incubating with a 1/50 dilution of TruStain FcX™ (BioLegend, San
212 Diego, USA) in PBS at room temperature for 15 min. An antibody cocktail was prepared
213 from the Maxpar® Mouse Sp/LN Phenotyping Panel Kit (Standard BioTools, San
214 Francisco, USA), with and additional antibody against IgM. Cells were incubated with
215 antibodies for 60 min, on ice before washing 3 times in Maxpar® Cell Staining Buffer
216 (Standard BioTools, San Francisco, USA) as previously. Following staining, cells were
217 fixed in 2% paraformaldehyde (PFA) overnight at 4°C. Cells were then washed twice with
218 1X eBioscience™ Permeabilization Buffer (Invitrogen, Waltham, USA) at 800 x g at room
219 temperature for 5 min. The pellets were resuspended in intracellular antibody cocktail
220 and incubated at room temperature for 45 min. Cells were washed 3 times in Maxpar®
221 Cell Staining Buffer (Standard BioTools, San Francisco, USA) at 800 x g. The cells were
222 then resuspended in 4% PFA at room temperature for 15 min, before collecting the cells
223 at 800 x g and resuspending in Cell-ID™ Intercalator-Ir (Standard BioTools, San
224 Francisco, USA). Finally, the cells were barcoded by transferring the stained cells to a
225 fresh tube containing 2 µL of palladium barcode from the Cell-ID™ 20-Plex Pd Barcoding
226 Kit (Standard BioTools, San Francisco, USA). Cells were then frozen in a freezing
227 solution (90% FBS and 10% DMSO), before shipping to the Flow Cytometry Core Facility
228 at the University of Manchester for data acquisition. Sample analysis was conducted
229 using Cytobank and custom-built, python-based analysis scripts developed in house
230 (**S1B and 1C Figure for QC results**). The antibodies used for labelling were as follow
231 (Standard Biotools, cat No. 201306): Ly6G/C [Gr1] (141^{Pr}, clone RB6-8C5, 1/100), CD11c
232 (142^{Nd}, clone N418, 1/100), CD69 (145^{Nd}, clone H1.2F3, 1/100), CD45 (147^{Sm}, clone 30-F11,
233 1/200), CD11b (148^{Nd}, clone M1/70, 1/100), CD19 (149^{Sm}, clone 6D5, 1/100), CD3e (152^{Sm}, clone
234 145-2C11, 1/100), TCRβ (169^{Tm}, clone H57-597, 1/100), CD44 (171^{Yb}, clone IM7, 1/100), CD4
235 (172^{Yb}, clone RM4-5, 1/100), IgM (151^{Eu}, clone RMM-1, 1/100), IFNγ (165^{Ho}, clone XMG1.2,
236 1/100).

237 **Single cell transcriptomics analysis of murine meninges**

238 The single cell suspension obtained from murine meninges after the CD45-PE depletion
239 step was diluted to ~1,000 cells/μl (in 1X phosphate buffered saline supplemented with
240 0.04% BSA) and kept on ice until single-cell capture using the 10X Chromium platform.
241 The single cell suspensions were loaded onto independent single channels of a
242 Chromium Controller (10X Genomics) single-cell platform. Briefly, ~25,000 single cells
243 were loaded for capture using 10X Chromium NextGEM Single cell 3 Reagent kit v3.1
244 (10X Genomics). Following capture and lysis, complementary DNA was synthesized and
245 amplified (12 cycles) as per the manufacturer's protocol (10X Genomics). The final library
246 preparation was carried out as recommended by the manufacturer with a total of 14
247 cycles of amplification. The amplified cDNA was used as input to construct an Illumina
248 sequencing library and sequenced on a Novaseq 6000 sequencers by Glasgow
249 polyomics.
250 **Read mapping, data processing, and integration.** For FASTQ generation and
251 alignments, Illumina basecall files (*.bcl) were converted to FASTQs using bcl2fastq.
252 Gene counts were generated using Cell Ranger v.6.0.0 pipeline against a combined *Mus*
253 *musculus* (mm10) and *Trypanosoma brucei* (TREU927) transcriptome reference. After
254 alignment, reads were grouped based on barcode sequences and demultiplexed using
255 the Unique Molecular Identifiers (UMIs). The mouse-specific digital expression matrices
256 (DEMs) from all six samples were processed using the R (v4.1.0) package Seurat
257 v4.1.0[38]. Additional packages used for scRNAseq analysis included dplyr v1.0.7,
258 RColorBrewer v1.1.2 (http://colorbrewer.org), ggplot v3.3.5, and sctransform v0.3.3[39].
259 We initially captured 20,621 cells mapping specifically against the *M. musculus* genome
260 across all conditions and biological replicates, with an average of 30,407 reads/cell and
261 a median of ~841 genes/cell (**S1 Table and S1D Figure**). The number of UMIs was then
262 counted for each gene in each cell to generate the digital expression matrix (DEM). Low
263 quality cells were identified according to the following criteria and filtered out: *i*) nFeature
264 <200 or >4,000 genes, *ii*) nCounts <200 or >4,000 reads, *iii*) >20% reads mapping to
265 mitochondrial genes, and *iv*) >40% reads mapping to ribosomal genes, v) genes detected
266 < 3 cells. After applying this cut-off, we obtained a total of 19,690 high quality mouse-
267 specific cells with an average of 950 genes/cell (**S1 Table and S1D Figure**). High-quality
268 cells were then normalised using the *SCTransform* function, regressing out for total UMI
269 and genes counts, cell cycle genes, and highly variable genes identified by both Seurat
270 and Scater packages, followed by data integration using *IntegrateData* and

271 *FindIntegrationAnchors*. For this, the number of principal components were chosen using
272 the elbow point in a plot ranking principal components and the percentage of variance
273 explained (30 dimensions) using a total of 5,000 genes, and SCT as normalisation
274 method.
275 **Cluster analysis, marker gene identification, sub-clustering, and cell-cell**
276 **interaction analyses.** The integrated dataset was then analysed using *RunUMAP* (10
277 dimensions), followed by *FindNeighbors* (10 dimensions, reduction = "pca") and
278 *FindClusters* (resolution = 0.7). The resolution was chosen based on in silico analysis
279 using *Clustree*[40] (**S1E Figure**). With this approach, we identified a total of 19 cell clusters
280 The cluster markers were then found using the *FindAllMarkers* function (logfc.threshold
281 = 0.25, assay = "RNA"). To identify cell identity confidently, we employed a supervised
282 approach. This required the manual inspection of the marker gene list followed by and
283 assignment of cell identity based on the expression of putative marker genes expressed
284 in the unidentified clusters. This was particularly relevant for immune cells detected in our
285 dataset that were not found in the reference atlases used for mapping. A cluster name
286 denoted by a single marker gene indicates that the chosen candidate gene is selectively
287 and robustly expressed by a single cell cluster and is sufficient to define that cluster (e.g.,
288 *Cd79a, Cd4, C1qa, Cldn5*, among others). When manually inspecting the gene markers
289 for the final cell types identified in our dataset, we noted the co-occurrence of genes that
290 could discriminate two or more cell types (e.g., DCs, mononuclear phagocytes,
291 fibroblasts). To increase the resolution of our clusters to help resolve potential mixed cell
292 populations embedded within a single cluster and, we subset fibroblasts, DCs, and
293 mononuclear phagocytes and analysed them individually using the same functions
294 described above. In all cases, upon subsetting, the resulting objects were reprocessed
295 using the functions *FindVariableFeatures, RunUMAP, FindNeighbors*, and *FindClusters*
296 with default parameters. The number of dimensions used in each cased varied depending
297 on the cell type being analysed but ranged between 5 and 10 dimensions. Cell type-level
298 differential expression analysis between experimental conditions was conducted using
299 the *FindMarkers* function (*min.pct* = 0.25, *test.use* = Wilcox) and (*DefaultAssay* = "SCT").
300 For cell-cell interaction analyses, we used CellPhoneDB[41] and NicheNet[42] with default
301 parameters using "mouse" as a reference organism, comparing differentially expressed
302 genes between experimental conditions (*condition_oi* = "Infected", *condition_reference* =
303 "Uninfected"). Pathways analysis for mouse genes were conducted using STRING [26] with
304 default parameters. Module scoring were calculated using the *AddModuleScore* function

305 to assign scores to groups of genes of interest (*Ctrl* = 100, *seed* = NULL, *pool* =NULL),
306 and the scores were then represented in feature plots. This tool measures the average
307 expression levels of a set of genes, subtracted by the average expression of randomly
308 selected control genes. The complete gene list used for module scoring derived from
309 previous publications[25] or from the MatrisomeDB[43]. Once defined, the collated gene list
310 was used to build the module scoring. Raw data and scripts used for data analysis will
311 be made publicly available after peer review.
312 **Whole mount meningeal preparation and immunofluorescence.** After euthanasia,
313 the skull caps were carefully removed using fine tweezers and scissors and placed
314 immediately in 10% neutral buffered Formalin (NFB) for 10 minutes at room temperature.
315 Coronal brain sections were also fixed as above, embedded in paraffin, and processed
316 for Luxol Fast blue used as a proxy to measure the levels of myelin. Following fixation of
317 the skull caps, for immunofluorescence staining, the meninges were detached from the
318 skull caps using a stereotactic microscope and kept at 4°C in 1X PBS containing 0.025%
319 sodium azide until imaging (no longer than one week). For histological analysis, the dura
320 meninges were left attached to the skull and the samples were decalcified prior to
321 embedding in paraffin using neutral EDTA. 2-3 μm skull sections were then prepared for
322 in situ hybridisation experiments or for Masson's trichrome staining. For
323 immunofluorescence staining, sections were blocked with blocking buffer (1X PBS
324 supplemented with 5% foetal calf serum and 0.2% Tween 20) and incubated with the
325 following primary antibodies at 4°C overnight: REAfinity anti-mouse FITC CD21/35
326 (Miltenyi, 1:50), rat anti-mouse ER-TR7 (Novus Biologicals, 1:100), REAfinity anti-mouse
327 PE CD3 (Miltenyi, 1:100), REAfinity anti-mouse APC B220 (Miltenyi, 1:100), anti-mouse
328 CD138 PE (BD Bioscience, 1:100). For the detection of ER-TR7, we used an anti-rat
329 antibody coupled with PE (Thermo, 1:500) for 1 hour at room temperature. All the
330 antibodies were diluted in blocking buffer. Slides were mounted with Vectashield
331 mounting medium containing DAPI for nuclear labelling (Vector Laboratories) and were
332 visualized using an Axio Imager 2 (Zeiss). Single molecule fluorescent *in situ*
333 hybridisation (smFISH) experiments were conducted as follow. Briefly, to prepare tissue
334 sections for smFISH, infected animals and naïve controls were anesthetized with
335 isoflurane, decapitated and the skull caps containing the dura mater layer of the
336 meninges were dissected and place on ice-cold 1X HBSS. The skulls were then fixed
337 with 4% paraformaldehyde (PFA) at 4 °C for 15 min, and then dehydrated in 50, 70 and

338 100% ethanol. After fixation, the skulls caps were decalcified, cut coronally and
339 embedded in paraffin. 5 μm skull cap sections were RNAscope 2.5 Assay (Advanced Cell
340 Diagnostics) was used for all smFISH experiments according to the manufacturer's
341 protocols. We used RNAscope probes against mouse *Rarres2* on channel 1 (Cat No.
342 572581), *Cxcl13* on channel 2 (Cat. No. 406311-C2), and Ly6a on channel 3 (Cat. No
343 427571-C3). All RNAscope smFISH probes were designed and validated by Advanced
344 Cell Diagnostics. For image acquisition, 16-bit laser scanning confocal images were
345 acquired with a 63x/1.4 plan-apochromat objective using an LSM 710 confocal
346 microscope fitted with a 32-channel spectral detector (Carl Zeiss). Lasers of 405nm,
347 488nm and 633 nm excited all fluorophores simultaneously with corresponding beam
348 splitters of 405nm and 488/561/633nm in the light path. 9.7nm binned images with a pixel
349 size of 0.07um x 0.07um were captured using the 32-channel spectral array in Lambda
350 mode. Single fluorophore reference images were acquired for each fluorophore and the
351 reference spectra were employed to unmix the multiplex images using the Zeiss online
352 fingerprinting mode. All fluorescent images were acquired with minor contrast
353 adjustments where needed, and converted to grayscale, to maintain image consistency.
354 **Flow cytometry analysis and *ex vivo* stimulation of meningeal-dwelling T cells.** To
355 discriminate circulating versus brain-resident immune cells, we performed intravascular
356 staining of peripheral $CD45^+$ immune cells, as previously reported[37]. Briefly, a total of 2
357 μg of anti-CD45-APC-Cy7 antibody (clone 30-F11, in 100 μl of 1X PBS) was injected
358 intravenously ~3 minutes prior culling. Mice were euthanised as described above and
359 transcardially perfused with ice-cold 0.025% (wt/vol) EDTA in 1X PBS. Whole meninges
360 were enzymatically digested with Collagenase P (1 mg/ml) and DNAse I (1 mg/ml; Sigma)
361 in 1X PBS (HSBB) (Invitrogen) for ~30 min at 37 °C, according to previously published
362 protocols[44]. Single-cell suspensions were passed through 70 μm nylon mesh filters to
363 remove any cell aggregates. The cell suspension was cleaned up and separated from
364 myelin debris using a Percoll gradient. The resulting fraction was then gently harvested
365 and used as input for *ex vivo* T cell stimulation or used as input for downstream flow
366 cytometry analysis. Briefly, the resulting cell fraction was diluted to a final density of
367 ~$1x10^6$ cells/ml and seeded on a 96 well plate and stimulated with 1X cell Stimulation
368 cocktail containing phorbol 12-myristate 13-acetate (PMA), Ionomycin, and Brefeldin A
369 (eBioSciences™) for 5 hours at 37°C and 5% CO_2. Upon stimulation, the cells were
370 analysed for the expression of IL-21 and PD-1.

371 For flow cytometry analysis, meningeal single cell suspensions were resuspended in ice-
372 cold FACS buffer (2 mM EDTA, 5 U/ml DNAse I, 25 mM HEPES and 2.5% Foetal calf
373 serum (FCS) in 1X PBS) and stained for extracellular markers. The list of flow cytometry
374 antibodies used in this study were obtained from Biolegend and are presented in the table
375 below. Samples were run on a flow cytometer LSRFortessa (BD Biosciences) and
376 analysed using FlowJo software version 10 (Treestar). For intracellular staining, single-
377 cell isolates from brain were stimulated as above in Iscove's modified Dulbecco's media
378 (supplemented with 1X non-essential amino acids, 50 U/ml penicillin,
379 50 μg/ml streptomycin, 50 μM β-mercaptoethanol, 1 mM sodium pyruvate and 10% FBS.
380 Gibco). Cells were then permeabilized with a Foxp3/Transcription Factor Staining Buffer
381 Set (eBioscience) and stained for 30 min at 4 °C. The anti-mouse GP38 (1:100) and the
382 LTβ (monoclonal antibody BBF6[45]; 10 μg/ml) antibodies were kindly provided by Dr. Lalit
383 Kumar Dubey (QMUL). For the detection of LTβ in $CD4^+$ T cells, we used a goat anti-
384 hamster (Armenian) IgG coupled to FITC as secondary antibody (Biolegend; 1:200). For
385 the detection of GP38 we used a Syrian hamster-anti mouse GP38 followed by anti-
386 Syrian hamster secondary antibody coupled to APC/alexa647 (Jackson
387 ImmunoResearch; 1:100). We used the following commercially available antibodies from
388 Biolegend: CD45-APC-Cy7 (clone 30-F11, 2 μg/100 μl 1X PBS i.v.), TER-119-APC-Cy7
389 (clone TER-119; 1/400), CD19-APC-Cy7 (clone 1D3/CD19; 1/400), F4/80-APC-Cy7
390 (clone BM8; 1/400), F4/80-PE Dazzle 594 (clone BM8; 1/400), CD3-APC (clone 17A2;
391 1/400), CD4-FITC (clone GK1.5; 1/400), PD1-BV711 (clone 29F.1A12; 1/400), CXCR5-
392 BV421 (clone L138D7; 1/200), IL-21-PE (clone 3A3-N2; 1/200), CD45-BV711 (clone 30-
393 F11; 1/400), CD31-BV421 (clone 8.1.1; 1/100), CD21/35-PE Dazzle 594 (clone 7E9;
394 1/100), MAdCAM-1-Alexa Fluor 488 (clone MECA-367; 1/100), CD19- Alexa Fluor 488
395 (clone 6D5; 1/400), CD138-PE (clone 281-2; 1/200), IgG-BV421 (clone Poly4053; 1/200),
396 IgM-BV711 (clone RMM-1; 1/200), CD8a-BV421 (clone QA17A07; 1/400), I-A/I-E-PerCP-
397 Cy5.5 (clone M5/114.15.2; 1/400)

398 **ELISPOT assays**

399 ELISPOT tests to measure *ex vivo* the frequency of meningeal antibody secreting cells
400 (ASCs) was performed using the ELISpot Flex IgM- and IgG-HRP (Mabtech) as followed.
401 After generating single cell suspensions from meningeal preparations, a total of 50,000
402 cells per well were seeded on 96-wells multiscreen-HA filter plates (Millipore) coated with
403 50 μg/ml of either whole *T. brucei*, prepared in house, or mouse brain lysate (Novus

404 Biologicals) to determine the presence of *T. brucei*- and mouse brain-reactive antibody
405 secreting cells, respectively. Wells coated with 50 μg/ml BSA (Sigma) were also included
406 as negative controls. After seeding the cells, the plates were incubated for 16 hours at
407 37°C, and 5%CO_2 covered in foil to avoid evaporation. In parallel, plates coated with 15
408 μg/ml affinity-purified goat anti-mouse IgM and IgG were also analysed in parallel to
409 measure the frequency of total IgM and IgG ASCs. For this, we used a total of 25,000
410 cells per well and incubated as before. Spots were enumerated with an Immunospot
411 analyser (CTL, Germany).

412 **Detection of autoreactive IgM and IgG by ELISA**

413 Serum samples from naïve and infected animals at 30 days post-infection were used to
414 examine the presence of mouse brain lysate-specific IgM and IgG using a colorimetric
415 approach. For this purpose, polysorb ELISA plates (Biolegend) were coated overnight
416 with 50 μg/ml either *T. brucei* Antat 1.1E whole cell lysate prepared in house, or mouse
417 brain lysate (Novus Biologicals) in 1X coating buffer (Biolegend). After extensive washes
418 with 1X ELISA washing buffer (Biolegend), total mouse IgM or IgG were detected in
419 mouse serum (1:50 to 1:10,000 dilution in 1X PBS) or human CSF (1:400 in 1X PBS) by
420 using Horseradish peroxidase-conjugated antibodies specific for mouse IgM (Thermo) or
421 IgG (all isotypes; Sigma) using the recommended concentrations, and the resulting
422 absorbance was detected at 450 nm using an ELISA Multiskan plate reader (Thermo).

423 **Detection of host antigens detected by autoantigens**

424 Blood samples were collected by cardiac puncture from naïve mice (*n* = 3 mice) or at
425 30dpi (*n* = 3 mice) were and place on EDTA tubes, from which serum was obtained. In
426 parallel, we screened CSF samples collected from 1st stage sleeping sickness patients
427 (*n* = 3 patients) and 2nd stage patients (*n* = 4 patients). Due to ethical constraints, we did
428 not have access to CSF samples from African healthy donors. Therefore, we obtained
429 CSF samples from healthy Caucasian donors (*n* = 2 donors) from the University of
430 Edinburgh Brain and Tissue Bank. Autoantibodies were assessed using a commercial
431 microarray-based platform (GeneCopoeia). Briefly, mouse serum or human CSF
432 samples were hybridised to distinct microarray spots containing 120 native host and viral
433 antigens spotted onto nitrocellulose fibers (adhered to glass slides). Next, the slides were
434 incubated with fluorescently-coupled anti-IgG or anti-IgM secondary antibodies, and
435 microarrays were scanned using a GenePix 4400A microarray scanner. Raw

fluorescence data was normalized to PBS controls on each slide. The data presented in the heatmaps are normalised signal-to-noise ratios.

Data availability

The transcriptome data generated in this study have been deposited in the Gene Expression Omnibus (GSE229436; Reviewer's token: mzitckmgbtmtxqz). The processed transcript count data and cell metadata generated in this study, as well as the code for analysis, are available at Zenodo (https://doi.org/10.5281/zenodo.7814657). Additional data and files can also be sourced via Supplementary Tables.

Code availability

The processed transcript count data and cell metadata generated in this study, as well as the code for analysis, are available at Zenodo (DOI: 10.5281/zenodo.7814657).

Statistical analysis

All statistical analyses were performed using Graph Prism Version 8.0 for Windows or macOS, GraphPad Software (La Jolla California USA). The data distribution was determined by normality testing using the Shapiro-Wilks test. Where indicated, data were analysed by unpaired Student's t-test, Mann-Whitney test, or one-way analysis of variance (ANOVA). Data were considered to be significant where $p < 0.05$. For the *in vivo* experiments, we matched sex and age of the mice in experimental batches using a block design including randomisation of experimental units. Data collection and analysis were not performed blindly to the conditions of the experiment due to the specific requirements of the UK Home Office project licence.

470 **Results**

471 **The murine meninges are colonised by a diversity of immune cells during chronic**
472 ***T. brucei* infection**

473 We and others have shown an increase in meningeal infiltration and meningitis during
474 the chronic stage (25dpi onwards) in experimental infections with *T. brucei*[10,13]. Previous
475 studies have shown that mouse meninges are colonised by $CD2^+$ T cells and $CD11c^+$
476 dendritic cells (DCs) during chronic *T. brucei* infection[9], although a catalogue of the
477 immune interactions spanning beyond these compartments is lacking. To fill this gap in
478 knowledge, we used an integrative multi-omics approach that combined CyTOF and 10X
479 Chromium single cell transcriptomics (**Figure 1A**) to understand the complexity of the
480 immune interactions taking place in the meningeal space during chronic *T. brucei*
481 infection. In addition to unbiasedly cataloguing the cells involved in this process, this
482 approach also allowed us to identify transcriptional pathways involved in the anti-parasitic
483 responses in the meninges with as much resolution as possible. We focussed on
484 characterising the dura mater as this has been previously shown to contain the vast
485 majority of the meningeal $CD45^+$ immune cells[42], as well as parasites during the chronic
486 stages of the infection[9]. To ensure we captured the diversity of resident immune cells and
487 meningeal stroma with as much confidence as possible, we selectively removed all
488 circulating $CD45^+$ immune cells using a magnetic sorting approach (**Figure 1A and S1A**
489 **Figure**). In brief, we labelled circulating $CD45^+$ cells by intravenous injection with an anti-
490 $CD45^+$ antibody coupled to phycoerythrin (PE). All the circulating $CD45^+$ were then
491 isolated using an anti-PE antibody coupled to magnetic beads. After extensive perfusion,
492 the remaining circulating (PE^+ cells) cells were removed leaving behind resident $CD45^+$
493 cells (PE^- cells), as well as stromal cells, including fibroblasts and cells associated with
494 the vasculature and the lymphatic system.

495 Firstly, we decided to explore the broad immunological landscape in the meninges of
496 mice at 30dpi, when infection in the CNS is well established[9–13]. For this reason and given
497 the scarcity of cells typically obtained from the meninges, CyTOF was used as this
498 approach enables detection of a wide range of cell types. Our CyTOF data was
499 composed of T cells ($CD4^+$ and $CD8^+$ T cells, including $IFN\gamma^+$ subsets, NK and $\gamma\delta$ T cells),
500 B cells (including IgM^{High} B cells and $CD11c^+$ B cells), and myeloid cells including
501 neutrophils and macrophages (**Figure 1B-D, S1B and S1C Figure**), consistent with
502 previous work[2]. Overall, we detected a significant increase in the number of $CD45^+$ cells

503 (**Figure 1E**), and an increased in number of the various immune subsets in the murine
504 meninges at 30dpi compared to naïve controls (**Figure 1F**), without noticeable changes
505 in cell frequency **(Figure 1G**). Together, these data suggested the expansion and/or
506 recruitment of resident immune cells into the meninges in response to infection.
507 To gain an understanding of the transcriptional responses triggered in the meninges in
508 response to infection, and to identify potential interactions between various meningeal
509 cells during infection, we performed single cell RNA sequencing of meningeal
510 preparations from mice at 30 dpi (*n* = 2 pools; 2 mice/pool) and naive controls (*n* = 2
511 pools; 2 mice/pool). Using this approach and after removing cells catalogued as low
512 quality (**Materials and Methods**), we obtained a total of 19,690 high quality cells, from
513 which 1,834 cells derived from naïve meninges and 17,856 cells from infected meninges,
514 with an average of 605 genes per cell from naïve samples and 1,297 genes per cell from
515 infected samples (**Figure 2A, Figure S1D and S1E, and Materials and Methods**). As
516 expected, our single cell meningeal atlas encompasses stromal and immune cells, most
517 of which have previously been reported in the murine meninges[2,46]. Within the stromal
518 compartment, we identified two populations of *Col1a1*$^{+}$ fibroblasts, *Ccl19*$^{+}$ *Rarres2*$^{+}$ mural
519 cells, and *Wvf*$^{+}$ *Pecam1*$^{+}$ endothelial cells (**Figure 2A and 2B**). Within the immune
520 compartment, we identified five populations of mononuclear phagocytes (MNPs 1 to 5),
521 characterised by the expression of putative myeloid cell markers genes such as *Ccl8,*
522 *C1qa, Aif1, Adgre1* and *Cd14*, amongst others, as well as conventional DCs (cDCs; *Xcr1,*
523 *Zbtb46, Clec9a, Flt3* and *Itgae*) (**Figure 2A and 2B**)**.** Additionally, we also detected T
524 cells (*Trac, Cd3g, Cd3e, Cd4, Icos, Cd8a, Gzmb, Gzmk*), granulocytes, including
525 *S100a8*$^{+}$ *Ngp*$^{+}$ *Cd177*$^{+}$ neutrophils, and two populations of B cells (*Cd79a, Cd79b*) that
526 expressed markers of canonical plasma cell markers (e.g., *Sdc1*) (**Figure 2A and 2B**)**.**
527 Lastly, we detected a small proportion of cells (<0.5%) with high expression levels of
528 haemoglobin (*Hba-a1, Hbb-bt*) and genes typically related to neurons (*Neurod1,*
529 *Neurod4*) (**Figure 2A, 2B, and S2 Table**). Notably, we observed a robust increase in the
530 frequency of most of the cells within the immune compartment (**Figure 2C**) consistent
531 with the CyTOF dataset. Together, these analyses are consistent with profound
532 alterations in the cellular makeup of the murine meninges during chronic *T. brucei*
533 infection.
534 **Meningeal *Rarres2*$^{+}$ *Ly6a*$^{+}$ fibroblasts acquire lymphoid tissue stroma-like**
535 **properties during chronic *T. brucei* infection.**

536 Next, we focussed on the meningeal fibroblasts. The meningeal fibroblasts are a
537 heterogeneous cell population encompassing transcriptionally, spatially, and potentially
538 functionally distinct units critical for meningeal immunity[47–50], but their responses to
539 chronic protozoan infections remains to be elucidated. Therefore, we first asked whether
540 the three fibroblast clusters (Fibroblast 1, Fibroblast 2, and mural cells) identified in figure
541 2 contained discreet clusters of cell populations that were not resolved by the top-level
542 clustering. After sub-clustering, we identified 2,088 cells (547 and 1,541 cells from naïve
543 and infected meningeal preparations, respectively), distributed across eight discrete
544 subsets (**Figure 3A**). These clusters expressed marker genes putatively associated with
545 fibroblasts from the dura mater, including *Mgp, Gja1, Fxyd5 and Col18a1* (**Figure 3B**)[48],
546 but low or undetectable levels of markers proposed to be associated with arachnoid mater
547 fibroblasts (e.g, *Clnd11, Tbx18, Tagln*) or pia mater (e.g., *Lama2, S100a6, Ngfr*) (**Figure**
548 **3B**)[48]. These observations suggested that the majority of the fibroblasts within our dataset
549 were likely to be derived from the dura mater layer of the meninges[51]. These fibroblast
550 clusters also expressed *Col1a1, Col1a2, Pdgfra* and *Pdgfrb* to various degrees but lacked
551 *Pecam1* (encoding for CD31), suggesting that these cells are of mesenchymal origin
552 rather than endothelial[50,51] (**Figure 3C**). Furthermore, cells within clusters 0 to 5
553 expressed *Rarres2*, suggesting that these are meningeal pericyte-like fibroblasts[50], in
554 addition to *Ly6a* (which encodes for the Stem Cell antigen-1, *Sca1*) (**Figure 3C**),
555 suggesting they are likely to retain progenitor properties[50]. We thus classified these cells
556 as *Ly6a*$^+$ fibroblasts (**Figure 3A to 3C**). Clusters 0 to 3 also expressed *Pdpn*, which
557 encodes for GP38, and *Col6a2*, which is recognised by the antibody ER-TR7[52], and were
558 thus defined as fibroblast reticular cells (FRCs)-like *Ly6a*$^+$ fibroblasts 1 to 4 (**Figure 3C**).
559 Cells within cluster 4 expressed high levels of the antioxidant protein Fth1 in addition to
560 *Rarres2* and *Ly6a* and were labelled as *Fth1*$^+$ *Ly6a*$^+$ fibroblasts (**Figure 3C**). Cells within
561 cluster 5 also expressed *Ccl19* and *Aldh1a2,* recently shown to be associated with
562 lymphoid stroma in the milky spots[53], in addition to *Ly6a*, and were thus classified as
563 *Aldh1a2*$^+$ *Ccl19*$^+$ fibroblasts (**Figure 3C**). Cells within cluster 6 expressed high levels of
564 *Acta2* (which encodes for α-smooth muscle actin), as well as *Tnn, Postn*, and *Mmp13*,
565 and were thus classified as myofibroblasts[50]. Lastly, cells within cluster 7 expressed
566 *Slc38a2* and *Slc47a1*, consistent with the phenotype of dura and leptomeningeal
567 fibroblasts[54,55,56] recently reported to be enriched in several transporters, and were thus
568 assigned as *Ly6a*$^-$ dura fibroblasts (**Figure 3C**).

569 We also found heterogeneous responses to infection within the meningeal fibroblast
570 subset, including cells that display features of FRC and B cell zone reticular cells (BCRs)
571 in response to infection. Cells within cluster 0, 1, 2, 3, and to a lesser extent cells within
572 cluster 5 upregulated genes associated with FRCs[57] in response to infection, including
573 *Pdpn, Pdgfra, Pdgrfb, Vim*, and *Col6a3*, as well as secreted factors such as *Vefga* and
574 *Tnfsf13b* (encoding for BAFF) (**S3A Figure**). Cells within clusters 3, 5, and 6 upregulated
575 genes associated with BRCs[58] during infection, including *Cxcl13* (Cluster 5), *Itga7, Ltbr*
576 (cluster 5 and 6)*, Madcam1* (cluster 5), *Cr2* (cluster 3 and 6)*,* and *Tnfsf11* (encoding for
577 RANKL) in cluster 3 (**Figure 3C and S3B Figure**). Based on the expression pattern
578 observed across the fibroblast subset in response to infection, we catalogued clusters 0,
579 1, 2, and 3 as FRC-like cells, and cells within clusters 5 and 6 as BRC-like cells (**S3C**
580 **Figure**). Lastly, cells within cluster 2, described as a mature population of pericytes, were
581 exclusively detected in the infected meninges and were characterised by the expression
582 of genes associated with blood vessel development (*Fgfr, Thbs1, Fgf2*), as well as
583 leukocyte chemotaxis and myeloid differentiation (*Cxcl19*) (**Figure 3C and S3 Table**),
584 suggesting *de novo* expansion in response to infection. Additionally, all of the FRC-like
585 pericytes are predicted to be involved in extracellular matrix (ECM) remodelling in the
586 meninges, including collagen and proteoglycan deposition, as well as secretion of factors
587 involved in ECM production, as demonstrated by module scoring analysis using the
588 MatrisomeDB database[43] (**Figure S3D Figure**), which encompasses a curated proteomic
589 dataset of ECM derived from a wide range of murine tissues. Consistent with these *in*
590 *silico* predictions, we observed a consistent pattern of fibroblastic reactions and collage
591 deposition in the dura meninges from infected mice compared to naïve controls (**S3E**
592 **Figure**), further indicating an extensive meningeal ECM remodelling triggered in
593 response to infection.
594 Our results so far indicate that the dura mater layer of the meninges contains a diverse
595 population of stromal cells, including GP38^{+} and GP38^{-} stromal cells that resemble the
596 stroma of other lymphoid tissues and ECM remodelling. Consistent with our scRNAseq
597 data, using flow cytometry, we observed a significant expansion of GP38^{+} FRCs, and a
598 distinctive population of MAdCAM1^{+} CD21/CD35^{+} cells indicative of the presence of
599 FDC-like cells in the infected murine meninges compared to naïve controls (**Figure 3E-**
600 **F; Gating strategy in 2A Figure**), without significant changes in the lymphatic
601 endothelial cells (LECs) or blood endothelial cells (BECs) (**Figure 3E-F**). Furthermore,
602 using module scoring analysis, which allows us to assess global gene signatures

603 associated with a gene set or pathway (in this case, ectopic lymphoid tissue signatures),
604 we were able to identify that cells within cluster 5 were enriched for genes associated
605 with FDC-like function and stromal lymphoid tissues, including *Ccl19 and Cxcl13*,
606 compared to the other fibroblast clusters (**Figure 3H**), and may be derived from *Ly6a*$^{+}$
607 pericytes with a precursor capacity as previously reported[59,60]. Indeed, using *in situ*
608 hybridisation on independent tissue sections, we were able to confirm the presence of
609 *Ly6a*$^{+}$ *Rarres2*$^{+}$ cells that expressed *Cxcl13*$^{+}$ during infection (**Figure 3I**). Together, our
610 data demonstrate the presence of a rich diverse fibroblast population, encompassing
611 *Ly6a*$^{+}$ *Rarres2*$^{+}$ FRC-like pericytes, including *Aldh1a2*$^{+}$ *Ccl19*$^{+}$ FRC-like pericytes,
612 myofibroblasts, *Fth1*$^{+}$ fibroblasts, and perivascular dura fibroblasts. Our data also
613 suggests that chronic *T. brucei* infection induces an extensive remodelling of the
614 meningeal stroma compartment, resulting in the expansion of FRCs and FDC-like cells
615 without significant changes in the vasculature (LECs and BECs).

616 **Meningeal mononuclear phagocytes are predicted to be involved in antigenic**
617 **presentation and chemotaxis during chronic *T. brucei* infection**

618 The cells within the myeloid compartment in the murine meninges act as a critical first
619 line of defence against insults and were clearly expanded during the chronic stage of the
620 infection (**Figure 1 and 2**). To resolve the mononuclear phagocyte (MNPs) compartment
621 in more detail, we analysed these populations individually. In total, we obtained 10,760
622 cells organised into five major clusters: cluster 0 (33.8%), cluster 1 (25.04%), cluster 2
623 (19.7%), cluster 3 (13.4%), and cluster 4 (8.10%) (**Figure 4A**). Since clusters 0 and 2
624 expressed high levels of *Mrc1* (encoding for CD206) and the anti-inflammatory molecule
625 *Il18bp*, and *Siglec1* (encoding for CD169), we labelled these clusters as *Cd206*$^{+}$ border-
626 associated macrophages (BAMs) (**Figure 4B and S4 Table**). Clusters 1 and 3 contained
627 the immune sensors *Cd14* and *Tlr2*, in addition to *Mertk, Adgre1*, and *Ly6c2*. We
628 therefore labelled these clusters as monocyte-derived macrophages (MDMs). Lastly,
629 cells within cluster 4 expressed high levels of mitochondrial-associated transcripts (e.g.,
630 *mt-Co1, mt-Co2, mt-Atp6*), in addition *Itgal*, *Sirpa, Cd274, Nfkbia, Sell*, and *Cd44* (**Figure**
631 **4B and S4 Table**), and were labelled as metabolically active mononuclear phagocytes
632 (maMNPs) (**Figure 4A and B**). We also observed that *Cd206*$^{+}$ BAMs and cells within the
633 MDMs 1 cluster expressed high levels of *H2-Aa, Sirpa, Csf1r, Cxcl16,* and *Adgre1,* which
634 encodes for F4/80[61] (**Figure 4B and S4 Table**). Under homeostatic conditions, the
635 murine meninges were dominated by *Cd206*$^{+}$ BAMs, in agreement with previous reports[62]
636 (**Figure 4C**). However, during infection, there was a significant expansion of MDMs

637 (**Figure 4C**), suggesting that the murine meninges were populated by circulating
638 monocytes during chronic *T. brucei* infection, consistent with previous reports[10]. Cell-cell
639 interaction analyses predicted that meningeal MNPs establish significant interactions with
640 other cell types, including T cells, *via* antigenic presentation (**Figure 4D to 4F**), likely
641 driving T cell activation locally, as previously proposed[2,10]. Consistent with our *in silico*
642 predictions, based on the expression level of F4/80, we identified two populations of
643 CD11b$^+$ myeloid cells, that we defined as CD11b$^+$ F4/80^{high} (resembling *Cd206*$^+$ BAMs
644 and MDMs 1) and CD11b$^+$ F4/80^{low} (resembling MDMs 2 and maMNPs) (**Figure 4B, 4G,**
645 **and 4H**). During infection, there was a significant increase in the frequency of CD11b$^+$
646 F4/80^{low} MNPs, whereas the CD11b$^+$ F4/80^{high} MNPs population decreased in frequency
647 (**Figure 4G and 4H; Gating strategy in S2B Figure**). However, in both cases, we noted
648 a significant increase in the expression of MHC-II in both CD11b$^+$ F4/80^{high} and CD11b$^+$
649 F4/80^{low} MNPs (**Figure 4G and 4H**). Together, our results indicate that the resident
650 population of meningeal myeloid cells expand upon infection (e.g., either as a result of
651 local myeloid proliferation or *via* the recruitment of monocytes to the meningeal space)
652 likely driving both cell recruitment *via* chemotaxis and antigen presentation to CD4$^+$ T
653 cells. Our data are consistent with and complementary to independent reports focusing
654 on the ontogeny and dynamics of BAMs and MNPs under homeostasis[2] and during the
655 onset and resolution of *T. brucei* infection[10].

656 **The murine meninges contain T_{FH}-like cells during chronic *T. brucei* infection**

657 The accumulation of inflammatory T cell subsets in the meninges has been reported in
658 CNS infections with *T. brucei*[9], but their features and effector functions remain
659 unresolved. Our top level single cell analysis identified three discreet T cell clusters based
660 on the expression of *Trac, Cd3e, Cd3g, Cd4*, and *Cd8a* (**Figure 2A**). To resolve the
661 meningeal T cell compartment in more detail, we re-clustered the T cells and repeated
662 the dimensionality reduction analysis. Within the resident meningeal T cell compartment,
663 we identified four main transcriptional clusters, characterised by the expression of *Trbc1,*
664 *Cd4* (cluster 0, 1, and 2), and *Cd8a* (cluster 3) (**Figure 5A and 5B, and and S5 Table**).
665 Several of the genes observed in the CD4$^+$ T cells were putatively associated with a T_{FH}
666 like phenotype, including *Icos, Pdcd1* (encoding for PD-1), *Cxcr4, Ctla4, Maf*, *Nr4a1,*
667 *Csf1*, *Tox2, Cxcr5, Bcl6*, as well as the cytokines *Ifng* and *Il21* (**Figure 5B and 5C**). To
668 confirm this, we first examined the presence of T_{FH}-like T cells in the meninges *in vivo*
669 using flow cytometry. Consistent with our *in silico* predictions, we detected a significant
670 increase in the frequency of resident CXCR5$^+$ PD1$^+$ CD4$^+$ T cells in the murine meninges

671 in response to chronic *T. brucei* infection compared to naïve controls (**Figure 5D and 5E;**
672 **Gating strategy in S2C Figure**). Furthermore, *ex vivo* stimulation assays demonstrated
673 that chronic *T. brucei* infection results in a significant expansion of meningeal PD1$^+$ CD4$^+$
674 T that express IL-21 compared to naïve controls (**Figure 5F and 5G**), further indicating
675 their T_{FH}-like phenotype.
676 Our data so far also indicate that meningeal ecosystems promote T cell activation *via*
677 antigen presentation (**Figure 4D**). Indeed, both our *in silico* prediction and flow cytometry
678 experiments demonstrated an expansion of CD69$^+$ CD4$^+$ T cells in the infected meninges
679 compared to naïve controls (**Figure 5B, 5H, and 5I**), strongly suggesting local activation.
680 To examine whether meningeal T cells were activated *in situ* during infection, we initially
681 utilised Nur77^{GFP} reporter mice[63]. In this model, GFP expression is used as a proxy for
682 MHC-dependent TCR engagement resulting in T cell activation[63]. We observed a
683 significant increase in the frequency of *Nur77*-GFP$^+$ CD4$^+$ and CD8$^+$ T cells (**Figure 5J,**
684 **5K; Gating strategy in S2C Figure**), indicating local T cell activation within the murine
685 meninges. To further resolve whether T cell activation occurs *in situ*, we used the newly
686 reported *Nur77*^{Tempo} mice, a novel murine reporter line in which the expression of a
687 fluorescent timer (FT) protein is driven by *Nur77* expression[64,65]. This model enabled the
688 discrimination of newly activated (FT blue$^+$), persistent (FT blue$^+$ red$^+$), and arrested (FT
689 red$^+$) T cells based on MHC-dependent TCR engagement[64,65]. We observed a significant
690 increase in the frequency of newly activated and persistent CD4$^+$ T cells, and a
691 concomitant reduction in the frequency of arrested CD4$^+$ T cells in the meninges in
692 response to infection compared to naïve controls (**Figure 5L and 5M**), indicating that
693 most CD4$^+$ T cells are actively partaking in the local immune response, likely via antigenic
694 presentation. We also observed a significant increase in the frequency of newly activated
695 meningeal CD8$^+$ T cells, but a reduction in both persistent and arrested CD8$^+$ T cells,
696 perhaps indicating that the CD8$^+$ T cell responses are transitory (**S4A and S4B Figure**).
697 This pattern of local T cell activation was also detected in the CD69$^+$ CD4$^+$ T cells, in
698 which we detected a higher frequency of newly activated CD69$^+$ CD4$^+$ T cells and less of
699 arrested CD69$^+$ CD4$^+$ T cells (**S4C and S4D Figure),** altogether indicating the meningeal
700 T cells are newly activated in the meninges *in situ*. These observations are consistent
701 with previous studies showing that CD4$^+$ T cells actively patrol the meningeal landscape[2].
702 Taken together, these results demonstrate that the meningeal CD4$^+$ T cell population
703 undergoes newly and persistent MHC-dependent TCR engagement in the meninges,
704 promoting local responses *in situ*, but the CD8$^+$ T cell responses seem more transitory.

705 These responses are likely to provide all the necessary signals for activation, likely
706 resulting in T cell differentiation towards the observed a T_{FH}-like phenotype during chronic
707 *T. brucei* infection.

708 **The murine meninges contain plasmablasts/plasma cells and GL7$^+$ CD95$^+$ GC-like**
709 **B cells during chronic infection**

710 Previous studies have demonstrated that B cells represent a major immune population
711 in the meninges[42,46], although their dynamics during chronic infection are not yet
712 understood. We previously observed the expression of *Cxcl12* in dura and arachnoid
713 meningeal fibroblasts, which is critical for the differentiation and survival of early B cells
714 in the bone marrow[66,67]. Thus, we next explored the diversity of B cells in our dataset.
715 The majority of meningeal B cells detected in our dataset derived from the infected
716 meninges (1,688 cells out of 1,742 total B cells) (**Figure 2**). These cells expressed high
717 levels of genes associated with plasmablasts and plasma cells such as such as *Jchain*,
718 *Prdm1* (which encodes for BLIMP-1)*, Sdc1* (encoding CD138), *Ighm*, and *Irf4* (**Figure**
719 **6A**). Flow cytometry experiments further confirmed that the vast majority of the meningeal
720 B cells correspond to plasmablasts and plasma cells, and to a lesser extent CD19$^+$ B
721 cells (**Figure 6B; Gating strategy in S2D Figure**). Some of the marker genes identified
722 within the B cell clusters, such as *Pcna, Mki67, Ub2c and Ighg2* and *Ighg3*, are typically
723 associated with cell replication and class-switched B cells (**S2 Table**). These genes are
724 critical for affinity maturation and class switching during GC reactions[68]. Because the
725 transcriptional signatures observed within the B cell clusters were consistent with the
726 presence of extrafollicular GC-like reactions, we next examined this at the protein level.
727 We first exploited the Nur77^{GFP} reporter mouse line to measure BCR engagement within
728 the meninges. Given that Nur77^{GFP} expression in GC B cells is proposed to be markedly
729 reduced compared to activated B cells *in vivo*[69], and that *Nur77* restrains B cell clonal
730 dominance during GC reactions[70], this reporter line can be used to examine extrafollicular
731 GC-like reactions. In line with these studies, we detected significantly fewer GFP$^+$ CD19$^+$
732 B cells during infection compared to naïve controls (**Figure 6C and 6D, and S2D Figure**),
733 implying that upon infection, the meningeal B cells undergo GC-like reactions.
734 Intriguingly, the meningeal B cells also expressed *Cd38* and *Fas* (**Figure 6A**), similar to
735 dark zone (GFP^{low}) GC B cells[69]. Consistent with these observations, we detected a
736 significant accumulation of GL7$^+$ CD95/Fas$^+$ cells within the CD19+ B cell compartment
737 (**Figure 6E and 6F**), further corroborating the presence of GC-like B cells in the murine
738 meninges. Consistent with the GC-like and the transcriptional profile, we observed an

739 increase in the frequency of IgG$^+$ CD19$^+$ B cells in the murine meninges at 30dpi
740 compared to naïve controls (**Figure 6G and 6H**). In the spatial context, we observed
741 clusters of CD3$^+$ T cells, B220$^+$ B cells and CD21/35$^+$ FDCs in the murine meninges that
742 were not readily detectable in naïve animals (**Figure 6I and S5 Figure**), suggesting the
743 presence of immunological aggregates similar to those observed in tertiary lymphoid
744 tissues[26,27]. Together, our data indicates the presence of class-switched plasma
745 cells/plasmablasts as well as GC-like CD19$^+$ B cells in close proximity to CD3$^+$ T cells
746 and CD21$^+$/CD35$^+$ FDC-like cells in the murine meninges in response to *T. brucei*
747 infection.

748 ***T. brucei* infection results in the accumulation of meningeal autoreactive B cells**

749 The accumulation of meningeal B cells has been reported in several autoimmune
750 disorders such as neuropsychiatric lupus[25] and multiple sclerosis[28] where they are
751 responsible for the generation of autoantibodies that are linked to the pathology
752 associated with these disorders. However, it is unclear whether chronic *T. brucei* infection
753 also results in the accumulation of autoreactive B cells in the meningeal spaces. We
754 reasoned that in addition to generating B cell clones able to generate antibodies specific
755 to *T. brucei*, these local GC-like reactions taking place within the meningeal space might
756 also result in the development of autoreactive B cells. To directly test this hypothesis, we
757 examined the presence of meningeal resident IgG$^+$ antibody secreting cells (ASCs) able
758 to recognise *T. brucei* and mouse brain lysates using ELISpot. We observed a significant
759 accumulation of total IgG$^+$ ASCs in the murine meninges (**Figure 7A and 7B**), consistent
760 with our flow cytometry data (**Figure 6G-H**). We also detected a significant accumulation
761 of IgG$^+$ ASCs able to recognise *T. brucei* and mouse brain but not BSA (**Figure 7A and**
762 **7B**), indicative of the presence of autoreactive ASCs in the murine meninges during
763 infection. Interestingly, splenocytes from animals at 30dpi or naïve controls did not
764 contain autoreactive IgG$^+$ ASCs (**S6A Figure**), suggesting that the mouse brain-specific
765 autoreactive ASCs may arise locally within the meninges or within the CNS environment.
766 Histological analysis of the corresponding murine brain sections revealed extensive IgG
767 deposition in the infected brain compared to naïve controls, in particular in the
768 leptomeninges and the cortex (**Figure 7C**). The IgG antibody deposition observed in the
769 cerebral cortex in response to chronic infection was accompanied by a significant
770 demyelination, particularly in the cerebral cortex, internal capsule, and thalamic tracts
771 (**Figure 7D, and S6B and S6C Figure**). Additionally, we detected the presence of high
772 IgM and IgG titres in the serum of infected animals able to react to mouse brain antigens

773 compared to naïve controls (**Figure 7E**), further corroborating our histological and
774 ELISpot findings. It is important to note that the binding of circulating IgG antibodies to
775 the murine brain does not seem to be restricted to areas with high parasite accumulation
776 (e.g., lateral ventricles) (**Figure 7F**). In humans, in the cerebrospinal fluid of 2nd stage
777 *gambiense* HAT patients from North Uganda we observed significant levels of
778 autoreactive IgM and IgG antibodies able to recognise human brain lysates, but not BSA
779 (**Figure 7G, and S6 Table**), consistent with our findings in experimental infections. Taken
780 together, our data suggest that meningeal B cells undergo affinity maturation locally
781 within the meninges or the CNS space to generate IgG$^+$ ASCs directed against both *T.*
782 *brucei* and the mouse brain (and in gambiense HAT patients), is associated with cortical
783 and white matter demyelination, and results in autoimmunity.

784 **LTβ receptor signalling controls the accumulation of meningeal FDCs and**
785 **autoreactive B cells during chronic *T. brucei* infection.**

786 LTβ receptor (LTβR) signalling is critical for the formation, induction, and maintenance of
787 lymphoid tissues under homeostasis and disease[71–73]. This process requires interactions
788 between the LT$\alpha_1\beta_2$ heterodimer and its cognate receptor LTβR to induce broad effects
789 on FDC maintenance, promoting a favourable microenvironment promoting GC reactions
790 on B cells[71–73]. Furthermore, expression of LTα in the meninges causes *de novo* ectopic
791 lymphoid tissue formation and neurodegeneration in a model of myelin oligodendrocyte
792 glycoprotein-induced experimental autoimmune encephalitis[74]. Our data so far indicate
793 that the murine meninges develop ectopic lymphoid aggregates that display many
794 features of LTβ-driven lymphoid tissue formation, including the presence of FDCs like
795 structures, T_{FH} T cells, and GC-like B cells with evidence of somatic hypermutation. Thus,
796 we hypothesised that LTβR-signalling plays a similar role in the formation of meningeal
797 lymphoid aggregates and coordinating the meningeal responses to chronic *T. brucei*
798 infection. The gene which encodes the LTβR, *Ltbr,* was expressed myeloid cells,
799 endothelial cells, granulocytes, and fibroblasts in the meninges (**Figure 8A**), indicating
800 that LTβR signalling may occur at multiple levels within the murine meninges. Similarly,
801 LTβ (encoded by *Ltb*) is primarily expressed by the CD4$^+$ T cell clusters and to a lesser
802 extent by cDCs, neutrophils, CD8$^+$ T cells, and B cells (**Figure 8A**). Using flow cytometry,
803 we detected a significant increase in the frequency of CD4$^+$ T cells expressing
804 LTβ (**Figure 8B and 8C**), consistent with their T_{FH} phenotype[27]. Next, we investigated
805 the role of LTβR-signalling in the maintenance of local immunological responses within

806 the meningeal stroma. For this, mice were treated prior and during *T. brucei* infection with
807 a LTβR-Ig fusion protein to prevent the interaction of the ligands $LT\alpha_1\beta_2$ and LIGHT
808 (encoded by *Tnfsf14*) with LTβR (**Figure 8D**)[75]. LTβR-Ig treatment resulted in mice
809 unable to control systemic parasitaemia as efficiently as mice treated with an irrelevant
810 antibody or untreated mice (**S7A Figure**), and in a worsening in the clinical scoring (**S7B**
811 **Figure**), mirroring previous work using *Ltb*$^{-/-}$ mice infected with *T. brucei* in the context of
812 intradermal infections[76]. Furthermore, LTβR-Ig treatment significantly impaired the
813 expansion of meningeal FDCs (**Figure 8E and 8F**), and a significant accumulation of
814 meningeal LECs compared to naïve controls, which can be attributed to changes in
815 frequencies within other stromal compartments (**Figure 8E and 8F**). Using ELISpot, we
816 observed that LTβR-Ig treatment significantly impaired the expansion of both IgM^+
817 (**Figure 8G and S7C-E Figure**) and IgG^+ ASCs, including *T. brucei*- and mouse brain-
818 specific ASCs (**Figure 8G**), consistent with a central role for LTβR-signalling in the
819 formation of B cell follicles and GCs within secondary lymphoid organs and ectopic
820 lymphoid tissues[59,60,71,76]. Lastly, LTβR-Ig treatment significantly impaired the formation
821 of perivascular FDC-B cell clusters (**Figure 8H**), consistent with previous reports[59,60], and
822 prevented the cortical demyelination typically observed in response to chronic infection
823 (**Figure 8I and S7E Figure**). Together, these data demonstrate that LTβR signalling is
824 required for stromal responses and B cell accumulation and maturation in the meninges
825 during infection with *T. brucei*, further highlighting that the meninges depend on classical
826 lymphoid tissue-associated signalling pathways to coordinate local immune responses to
827 infections. Furthermore, the fact that LTβR-Ig treatment rescued the cortical
828 demyelination observed in response to infection suggests that the meningeal ectopic
829 lymphoid aggregates are indeed pathogenic.

830 **Infection-induced autoantibodies recognise a broad range of host antigens,**
831 **including myelin basic protein**

832 Given that our data so far indicate that chronic *T. brucei* infection results in the generation
833 of autoantibodies, we next decided to examine the nature of antigens recognised by these
834 autoantibodies. To achieve this, we employed a targeted array of 120 antigens known to
835 be identified in autoimmune disorders, from systemic lupus erythematous to multiple
836 sclerosis. Our data indicates that circulating IgG autoantibodies found in infected samples
837 significantly recognised a total of 18 antigens (15% of the antigen array), including
838 structural proteins (e.g., collagen VI, vitronectin, nucleolin, Histone H3), cytokines (e.g.,

839 GM-CSF), components of the complement system (e.g., C3, C1q), intracellular antigens
840 (e.g., ssDNA, ssRNA, mitochondrial antigen), and most importantly myelin basic protein
841 (MBP) (**Figure 9A, S7 Table, and S8A Figure**). To further understand whether the same
842 pattern of autoreactive antibodies is observed in sleeping sickness patients, we screened
843 CSF samples collected from patients during the 1st (haemolymphatic) stage and 2nd
844 (meningoencephalitic) stage. As observed in mice, our results highlighted a broad range
845 of host antigens recognised by IgG autoantibodies in the CSF exclusively detected during
846 the 2nd stage of the disease (**Figure 9B, S7 Table, and S8B Figure**). More specifically,
847 we detected reactivity against 51 antigens (42.5% of the antigen array), including several
848 structural proteins, cytokines (e.g., TGFβ1, TNFα, IL-12, TPO), intracellular antigens
849 (e.g., histones, nucleosome-related proteins, mitochondrial antigen), structural proteins
850 (e.g., collagens, vitronectin), amongst others (**Figure 9B**). Interestingly, as observed in
851 mice, we also detected the presence of autoantigens able to bind host proteins
852 associated with either parasite control or pathology, such as proteins of the complement
853 system (e.g., C1q, C3a) and nervous system-associated proteins (e.g., MBP and
854 muscarinic receptor) (**Figure 9B**). Indeed, a total of 8 antigens (13.1% of the antigen
855 array) were commonly identified by autoreactive antibodies in infected mouse serum and
856 human CSF from 2nd stage sleeping sickness patients, which are known to be diagnostic
857 markers of autoimmune disorders such as systemic lupus erythematosus, Sjogren's
858 syndrome, scleroderma, rheumatoid arthritis, and multiple sclerosis[77–79] (**Figure 9C**). To
859 further validate our findings, we examined the presence of circulating antibodies against
860 MBP in an independent cohort of sleeping sickness patients from DRC that included both
861 patients with an active infection ("cases") and samples obtained from patients post-
862 treatment ("treated) (**Figure 9D**). Consistent with the data obtained from CSF biopsies,
863 we observed that sleeping sickness patients with an active infection have significantly
864 higher titres of serum IgG against MBP compared to healthy African controls (**Figure 9D**).
865 Interestingly, most of the samples obtained from patients post-treatment display basal
866 levels of anti-MBP antibody titres and show no significant differences with healthy African
867 controls, suggesting that treatment with anti-parasitic chemotherapy prevents the
868 accumulation of anti-MBP autoantibodies in humans. However, we noted that 30% of the
869 treated patients maintained higher titres of anti-MBP antibodies in circulation, which might
870 be due to: a) failure to effectively clear parasites post-treatment and thus considered to
871 be relapsing cases; b) the presence of memory B cells that sustain anti-MBP

872 autoantibody secretion; c) or a combination of both. Taken together, our mid-throughput
873 targeted screening identified a myriad of host antigens recognised by infection-induced
874 autoantibodies in both chronically infected mice and 2nd stage sleeping sickness patients,
875 potentially indicative of a complex autoimmune disorder affecting several organs
876 including the CNS.

877 **The accumulation of meningeal GL7$^+$ CD95$^+$ GC-like B cells and autoreactive**
878 **antibodies depends upon parasite accumulation in the CNS**

879 Our data so far demonstrate that chronic *T. brucei* infection results in the accumulation
880 of autoreactive B cells that display a GL7$^+$ CD95$^+$ GC-like phenotype, likely resulting in
881 the generation of autoreactive antibodies and subsequent local IgG deposition in the
882 brain. We also identified MBP, a highly abundant CNS protein, to be one of the host
883 antigens recognised by these infection-induced IgG autoantibodies in both mice and
884 humans during chronic infections, potentially explaining the local antibody deposition
885 observed in the brain in our histological analyses. Given that at least 30% of 2nd stage
886 sleeping sickness patients displayed elevated levels of anti-MBP autoantibodies in
887 circulation post-treatment, likely as a result of treatment failure, we next decided to
888 explore whether suramin treatment, used in experimental infections to clear *T. brucei*
889 infections[18,80], prevented the accumulation of GL7$^+$ CD95$^+$ GC-like phenotype and IgG
890 deposition in the brain. In other words, whether an active CNS colonisation is necessary
891 to trigger local B cell responses. We tried several treatment strategies based on recent
892 studies[18,80], the majority of which resulted in mice relapsing to the infection. This was
893 particularly evident when treatment was started after 14dpi. In our hands, the most
894 effective treatment regime consisted of three consecutive doses of suramin (20 mg/kg)
895 i.p. at 5, 6, and 7dpi, consistent with previous studies[80] (**Figure 10A**). Using this model,
896 we observed ~50% of mice relapsing and ~50% of the animals completely clearing the
897 disease, as determined by qPCR against the *T. brucei*-specific gene *Pfr2* used here as a
898 proxy to quantify parasite tissue burden, alongside immunohistochemistry staining
899 against the *T. brucei*-specific antigen BiP (**Figure 10B and 10C**). Interestingly, in the
900 relapsing animals, we noted a significantly higher parasite burden in the brain compared
901 to infected but untreated controls. Using flow cytometry, we detected a significant
902 expansion of GL7$^+$ CD95$^+$ GC-like B cells in the meninges of infected animals that
903 remained high in the relapsing animals (**Figure 10D and 10E**). However, in cured mice,
904 the frequency of GL7$^+$ CD95$^+$ GC-like B cells in the meninges returned to basal levels
905 (**Figure 10D and 10E**). Furthermore, we observed a reduction in the IgG deposition in

906 the brain of cured mice (**Figure 10F**), reduced serum antibody titres of anti-brain IgG
907 autoantibodies in cured mice compared to infected or relapsing animals (**Figure 10G**),
908 and less cortical demyelination in cured mice compared to infected and relapsing animals
909 (**Figure 10H and 10I**), indicating that an active CNS infection is required to induce the
910 pathological antibody responses and cortical demyelination observed in response to
911 chronic infection. However, it is worth noting that cured mice still showed signs of
912 antibody deposition and serum levels of anti-brain IgG autoantibodies, albeit to a lesser
913 extent to infected or relapsing animals. Taken together, our results suggest that the
914 presence of parasites in the CNS either directly or indirectly promotes the expansion of
915 meningeal GL7$^+$ CD95$^+$ GC-like B cells and antibody deposition in the brain during
916 chronic infection.

917 **Discussion**

918 Here, we set out to characterise the local immune responses taking place within the
919 murine meninges in response to chronic infection with *T. brucei*. Our results demonstrate
920 that the murine meninges are dynamic structures able to support a wide range of immune
921 responses that are triggered upon infection with *T. brucei*, resulting in the acquisition of
922 ectopic lymphoid tissue-like signatures including the development of FDC-like cells, T_{FH}
923 cells, and GC-like B cells undergoing class switching. We also showed that during *T.*
924 *brucei* infection, the murine meninges also harbour a distinctive population of
925 autoreactive B cells that generate IgG$^+$ antibodies able to bind parasite and murine brain
926 antigens, including MBP. Furthermore, we demonstrated that the rearrangement of the
927 meningeal stroma, as well as the accumulation of autoreactive B cells, depend upon
928 LTβR signalling, consistent with its lymphoid tissue properties. Lastly, we demonstrated
929 the presence of IgG$^+$ antibodies in the CSF of 2nd stage gambiense HAT patients (when
930 the parasites accumulate in the meninges and CNS) able to recognise human brain
931 lysates and MBP, indicating that the observations using experimental infections are likely
932 to be conserved in humans.

933 Focussing on the stroma, we identified several populations of meningeal fibroblasts,
934 mostly derived from the dura mater layer of the meninges that express *bona fide* markers
935 of mesenchymal precursor cells (*Ly6a*$^+$). Interestingly, this population of meningeal
936 fibroblasts shares many transcriptional features with omental *Aldh1a2*$^+$ FRCs that are
937 known to play a critical role in modulating lymphocyte recruitment and local immune
938 responses in the peritoneum[53]. It is tempting to speculate that there exists a pre-defined

939 populations of fibroblasts with precursor capacity (e.g., Ly6a/Sca1^{+}) in several body
940 cavities, including the meninges, that are able to quickly sense and adapt to inflammatory
941 responses to efficiently coordinate local immune responses[81–83]. In this context, it is
942 plausible that the population of lymphoid stromal cells residing in the dura layer of the
943 meninges sense the presence of *T. brucei* (e.g., *via* TLR or cytokine signalling) to
944 promote local immunological responses, as recently proposed[84]. We propose that these
945 populations meningeal *Ly6a*$^{+}$ fibroblast precursors could adapt to chronic inflammatory
946 conditions, resulting in the development of stromal structures required to sustain long-
947 lasting immunological responses *in situ*, including FRC- and FDC-like cells, as well as *de*
948 *novo* angiogenesis. These observations are consistent with the idea that chronic
949 neuroinflammation results in lymphangionesis in the CNS[85]. All of these populations
950 participate in changes in the ECM during infection, including collagen and proteoglycan
951 deposition and regulation of the ECM, highlighting the extensive ECM remodelling taking
952 place in the meninges during chronic infection. The ontogeny of the meningeal FDC-like
953 cells that we detected under chronic infection with *T. brucei*, and whether they play an
954 active role in the neuroinflammatory process in this infection setting[86], requires further
955 investigation. Nevertheless, to our knowledge, this is the first report characterising the
956 response of meningeal fibroblasts to chronic infections with a protozoan parasite, which
957 has important implications for understanding how dynamic and adaptable the meningeal
958 stroma is under chronic inflammatory processes.
959 Additionally, we predicted that meningeal MNPs are involved in chemotaxis and antigen
960 presentation to CD4^{+} T cells. Consistent with recent studies characterising the dynamics
961 of myeloid cells within the brain borders in response to *T. brucei* infection[9,10], we identified
962 several subsets of MNPs and conventional DCs that play a wide range of roles, from
963 inflammatory responses to chemotaxis and antigenic presentation. Overall, all these
964 myeloid subsets might offer a first line of defence against incoming parasites, and
965 together with the meningeal stroma, might promote the recruitment and activation of
966 adaptive immune cells required to support an efficient local immune response. It also
967 remains to be determined whether the lymphatic structures present within the meninges
968 play an active role in the induction of ectopic lymphoid tissues during chronic *T. brucei*
969 infection.
970 We also detected an accumulation of autoreactive B cells able to produce high affinity
971 antibodies against both *T. brucei* and the mouse brain, resembling the pathology
972 observed under autoimmune neurological disorders including MS[87]. Previous work has

973 demonstrated the presence of autoreactive antibodies in HAT patients and during
974 experimental infections[88–92], some of which are able to recognise a wide variety of heat
975 shock proteins and ribosomal proteins[88,90] that might be evolutionarily conserved
976 between parasites and host. However, the local generation of autoreactive B cells in the
977 murine meninges able to recognise murine brain lysates in response to chronic infection
978 with *T. brucei* has not been reported before. These observations indicate that the local
979 immunological responses in the meninges could result in the (uncontrolled) production of
980 autoreactive antibodies, explaining their presence in the CSF of 2nd stage *gambiense*
981 HAT patients as shown in this study. Nevertheless, the mechanisms resulting in the
982 development of local autoantibodies remains to be determined.
983 Based on our dataset and *in vivo* experimental approaches, we conclude that the
984 formation of meningeal ELAs during chronic *T. brucei* infections relies on LTβR signalling.
985 This in turn is likely to supports the expansion of meningeal FDC-like fibroblasts and the
986 accumulation of GC-like autoreactive B cell clones and brain deposition of high-affinity
987 antibodies, potentially aided by the local activation and development of CXCR5$^+$ PD1$^+$
988 T_{FH}-like CD4$^+$ T cells expressing high levels of *Il21*. In this context, our data demonstrate
989 that chronic meningeal inflammation leads to the formation of plasma cells/FDC-like
990 cell/CD3$^+$ T cell aggregates, resembling those within the B cell follicle in lymph nodes and
991 spleen but lacking their typical microarchitecture, to sustain the production of high affinity
992 antibodies locally. It is important to note that the majority of the cells within the B cell
993 compartment were assigned as IgM$^+$ and IgG$^+$ plasma cells as shown before[2,42,46,93,94],
994 although their composition (IgA$^+$ vs IgM$^+$ and/or IgG$^+$) differs slightly from previous
995 elegant work describing the diversity of meningeal B cells compartment during fungal
996 infection[46]. Interestingly, in an experimental autoimmune encephalomyelitis (EAE) model,
997 the frequency of *Igha*$^+$ B cells found in the homeostatic dura mater decreased significantly
998 followed by a significant expansion of *Ighm* and *Ighg* expression in B cells during
999 inflammation[93], in a process similar to the results presented in this study. These
1000 differences might be attributed to technical differences between studies (e.g., depth of
1001 coverage) or biological differences due to intrinsic differences between disease
1002 conditions. It is important to note that, in addition to the autoreactive IgG$^+$ ASCs residing
1003 in the meninges and identified by ELISpot, vascular leakage (allowing the passage of IgG
1004 through the blood-brain barrier) reported in this model[95–97] may also contribute to the IgG
1005 deposition detected within the brain. However, at present we cannot directly assess the

1006 relative contribution of each process separately. Irrespective of the routes by which
1007 autoreactive antibodies reach the meningeal barrier and/or brain parenchyma, further
1008 work is required to identify whether they arise as a result of molecular mimicry (e.g.,
1009 shared epitopes between *T. brucei* and mice) or *via* bystander activation (e.g., continues
1010 TLR stimulation on B cells[98,99]). It remains unclear, however, whether the emergence of
1011 autoreactive B cells depends upon T cell-mediated responses (antigen-specific) or
1012 whether it results from T cell-independent processes (e.g., polyclonal activation, antigen-
1013 independent). In the context of T cell-dependent responses, future work is required to
1014 determine the nature of the antigens driving such specific responses, as well as the
1015 precise ontogeny of T_{FH} T cells (e.g., derived from T_H17 T cells as recently proposed[100])
1016 to the generation of high affinity autoreactive antibodies in the context of chronic
1017 infections remains to be delineated in more detail. It is likely that brain antigens such as
1018 MBP might be one (of several) antigen driving T cell-specific responses, in a similar
1019 process to experimental autoimmune encephalitis[101,102].
1020 The histological features related to antibody deposition in the meningeal and cortical
1021 spaces during chronic *T. brucei* infection are associated with cortical and white matter
1022 demyelination, which are reminiscent of the histopathological features observed in MS
1023 and other neurological autoimmune disorders[103–105]. However, it is unclear whether the
1024 cortical pathology observed in our infection model results in primary (B cells generating
1025 antibodies against myelin) or secondary demyelination, as a result of neuronal death.
1026 Importantly, *Aid*$^{-/-}$ mice, in which B cells are unable to undergo affinity maturation, are
1027 better at controlling *T. brucei* infections due to an increase in circulating (low affinity) IgM,
1028 suggesting that class-switching might indeed be an unfavourable process for the host[106],
1029 both in terms of parasite control and tissue immunopathology. Based on our data, local
1030 B cell affinity maturation and class-switching results in autoimmunity. In this scenario, it
1031 is tempting to speculate that most of the neuropathological features associated with
1032 chronic *T. brucei* infection derive from a disruption in peripheral tolerance resulting in
1033 maladaptive antibody responses, as recently demonstrated in variable immune
1034 deficiency patients with autoimmune manifestations[107]. Further studies are required to
1035 determine the type of antigens detected by the autoreactive antibodies generated
1036 specifically in the meninges, and to determine whether they share epitopes with *T. brucei*
1037 antigens due to molecular mimicry, as reported for EBV-induced MS[87]. Similarly, it is
1038 important to determine if B cell depletion strategies (e.g., B cell depletion
1039 approaches[108,109], including treatment with anti-CD20 treatment[110]) or chemotherapy

interventions to treat the infection ameliorate disease progression, meningeal inflammation, and cortical pathology during chronic *T. brucei* infection, similar to MS[109]. Lastly, our observations in both experimental infections and human studies indicate that sleeping sickness results in an autoimmune disorder affecting the CNS (and likely other organs), but it remains unclear whether these autoimmune disorders have an impact of sleep, contributing to the known sleep disruptions caused by this parasitic infection. In this regard, sleep disturbances are commonly reported in patients with autoimmune encephalitis[111–113], and in narcoleptic patients[114,115], potentially supporting a link between these pathologies. However, this remains to be further tested and the mechanisms elucidated.

Together, our data provide a novel perspective for understanding the cellular and molecular mediators that lead to the development of autoimmunity during chronic *T. brucei* infection. Furthermore, our results support the notion that the meningeal spaces are dynamic structures able to support a wide range of immunological responses, including those resulting in pathological outcomes such as autoreactive antibody deposition at the brain borders. In this context, we propose that experimental infections with African trypanosomes can be exploited to address basic questions regarding infection-induced autoimmunity and brain pathology, which could be leveraged for the treatment of complex neurological disorders of unknown aetiology such as MS in addition to the meningoencephalitic stage of sleeping sickness. Our results also highlight that chronic sleeping sickness in patients also results in the accumulation of autoreactive antibodies in the CNS, potentially driving pathology even after anti-parasitic chemotherapy. In this context, it becomes clear that a better understanding of the sequalae of the infection in human and animal health is critical but remains unsolved.

Funding and acknowledgments.

We gratefully acknowledge the contributions given by the tissue donors and their families from the Edinburgh Brain and Tissue Bank (REC 21/ES/0087). We thank Julie Galbraith and Pawel Herzyk (Glasgow Polyomics, University of Glasgow) for their technical support with library preparation and sequencing, and the technical staff at the University of Glasgow Biological Services for their assistance in maintaining optimal husbandry conditions and comfort for the animals used in this study. Similarly, we would like to thank the histopathology unit at the University of Glasgow veterinary school (In particular Frazer Bell and Lynn Stevenson) for their technical assistance with sample processing and preparation. We also thanks Professor Wendy Bailey (Liverpool School of Tropical

1074 Medicine, UK) for providing CSF samples from gambiense HAT patients from North
1075 Uganda, and Dr. Barry Bradford (Roslin Institute, UK) for his technical assistance with
1076 LFB image quantification. The authors would also like to thank the III Flow cytometry
1077 facility for their support with flow cytometry analysis, Dr. Gareth Howell (university of
1078 Manchester) for technical support with the mass cytometry experiments, and Dr. Chiara
1079 Pirillo (Beatson Institute) for technical assistance with the ELISpot assay. This work was
1080 funded by a Sir Henry Wellcome postdoctoral fellowship (221640/Z/20/Z to JFQ). AML is
1081 a Wellcome Trust Senior Research fellow (209511/Z/17/Z). PC and MCS are supported
1082 by a Wellcome Trust Senior Research fellowship (209511/Z/17/Z) awarded to AML. DB
1083 is funded by an MRC fellowship MR/V009052/1 and a Lister Institute Fellowship. NAM is
1084 supported by project Institute Strategic Programme Grant funding from the BBSRC
1085 (BBS/E/D/20002174 and BB/X010937/1). The authors declare that the research was
1086 conducted in the absence of any commercial or financial relationships that could be
1087 construed as a potential conflict of interest.

1088 **Author contributions**

1089 **Conceptualisation:** JFQ, NAM. **Methodology:** JFQ, MCS, LKD, PC, DB, JO, GM, MAS.
1090 **Sample collection in the field:** NRKS, DMN. **Formal analysis**: JFQ, MCS, PC, MH.
1091 **Writing – original draft:** JFQ**. Writing – reviewing and editing:** JFQ, MCS, LKD, GM,
1092 DB, AM, LDL, NAM. **Funding acquisition:** JFQ. All authors approved the current version
1093 of this manuscript. The authors declare that they have no competing interests,
1094 commercial or otherwise. Correspondence and requests for materials should be
1095 addressed to Juan F. Quintana (juan.quintana@glasgow.ac.uk).

1096 **Figures**

1097 **Figure 1. CyTOF confirms the expansion of innate and adaptive immune cells in**
1098 **the murine meninges during chronic *T. brucei* infection.**

1099 **A)** Overview of the experimental approach applied in this work. An anti-CD45-PE
1100 antibody was injected *i.v.* prior to cull, followed by magnetic sorting using anti-PE
1101 antibodies to obtain a fraction of resident meningeal cells that were used as input for
1102 single cell transcriptomics using the 10X Chromium platform. **B)** Uniform manifold
1103 approximation and projection (UMAP) visualisation of the CyTOF immunophenotyping in
1104 murine meninges from naïve and animals at 30dpi. The UMAP plot represents pooled
1105 data from n = 5-6 mice/group. **C)** Normalised protein expression level of markers used to
1106 define T cells and NK cells (TCRβ, TCRγδ, NK1.1), B cells (CD19, B220, IgM), and

1107 myeloid cells (CD11b, Ly6G/C, and CD11c). **E)** Quantification of $CD45^+$ cells in the
1108 murine meninges by CyTOF at 30dpi (*n* = 5 mice/group). Parametric two-sided *T* student
1109 test: a *p* value < 0.05 was considered significant. **D)** Unsupervised cell annotation from
1110 CyTOF data using a combination of several marker genes. The expression level is
1111 normalised to the average of the expression within the group. **F)** Quantification of the
1112 different populations of immune cells in the naïve and infected murine meninges (*n* = 5-
1113 6 mice/group). A parametric ANOVA test with multiple comparison was used to estimate
1114 statistically significant pairwise comparisons. A *p* value < 0.05 is considered significant.
1115 Data in all panels are expressed as mean ± SD. Data points indicate biological replicates
1116 for each panel. **G)** Bar chart depicting the frequency of the different immune populations
1117 identified in the murine meninges by CyTOF.

1118 **Figure 2. Single cell atlas of the murine meninges during chronic *T. brucei***
1119 **infection.**

1120 **A)** A total of 19,690 high-quality cells were used for dimensionality reduction, resulting in
1121 uniform manifold approximation and projection (UMAP) for the single cell transcriptome
1122 profiling from naïve (n = 2 pools; 1,834 high quality cells in total) and infected meninges
1123 (n = 2 pools; 17,856 high quality cells in total). **B)** Dotplot representing the expression
1124 levels of top marker genes used to catalogue the diversity of cell types in our single cell
1125 dataset. **C)** Frequency of the different cell types detected in the murine meninges
1126 analysed in this study.

1127 **Figure 3. The meningeal stromal compartment acquires lymphoid-like properties**
1128 **and provide cues for immune cell recruitment during chronic *T. brucei* infection**

1129 **A)** Uniform manifold approximation and projection (UMAP) of 2,088 high-quality cells
1130 within the fibroblast clusters were re-analysed to identify a total eight subclusters. **B)** Dot
1131 plot representing the expression levels of marker genes previously reported to be
1132 enriched in fibroblasts from different meningeal layers, including dura mater, pia mater,
1133 and arachnoid mater. **C)** Dot Plot representing the expression levels of top marker genes
1134 used to catalogue the diversity of cell types in our single cell dataset. **D)** Frequency plot
1135 the different fibroblast clusters detected in the murine meninges in naïve and infected
1136 samples (*n* = 2 pools per experimental condition). **E)** Representative flow cytometry
1137 analysis of meningeal stromal cells from naïve and infected meningeal preparations (left
1138 panel), and the corresponding quantification **(F)**. A The data in all panels is expressed as
1139 mean ± SD. Data points indicate biological replicates for each panel. A parametric T test
1140 was employed to assess significance between experimental groups. A *p* value < 0.05 is

1141 considered significant. FRC, fibroblast reticular cells; LECs, lymphatic endothelial cells;
1142 BECs, blood endothelial cells; FDCs, follicular dendritic cells. **G)** Module scoring for
1143 genes typically associated with lymphoid tissues. **H)** Violin plot depicting the expression
1144 of two chemokines associated with lymphoid tissues such as *Ccl19* and *Cxcl13*. **I)** Single
1145 molecule fluorescent *in situ* hybridisation (smFISH) demonstrating the presence of *Ly6a*$^{+}$
1146 *Rarres2*$^{+}$ cells that express *Cxcl13* in the dura mater of the meninges of infected mice.
1147 DAPI is included as a nuclear marker. The skull bone, the bone marrow (BM), and the
1148 meninges are indicated. Scale bar, 50 μm.

1149 **Figure 4. Heterogeneity of meningeal mononuclear phagocytes during chronic T.**
1150 **brucei infection.**

1151 **A)** Uniform manifold approximation and projection (UMAP) of 10,760 high-quality
1152 mononuclear phagocytes (MNPs) from naïve (n = 54 cells) and infected meninges (n =
1153 10,706 cells). **B)** Expression level of top genes defining different populations of meningeal
1154 MNPs. **C)** Frequency plot depicting the relative abundance of the five MNPs subclusters
1155 identified in the murine meninges during *T. brucei* infection. **D)** Cell-cell interaction
1156 network via MCH-II signalling axis. **E)** Violin plot depicting the expression level of *H2-D1*
1157 and *H2-Ab1*, two of the most upregulated MHC-II associated genes within the myeloid
1158 compartment. **F)** Cell-cell interaction network *via Cxcl* signalling axis. **G)** Representative
1159 flow cytometry analysis and quantification (**H**) of CD11b^{+} F4/80^{High} and F4/80^{Low} myeloid
1160 cell populations, as well as MHC-II^{+} myeloid cells, in the murine meninges in response to
1161 *T. brucei* infection. Data in all panels are representative from two independent
1162 experiments and is expressed as mean ± SD (*n* = 5 mice/experimental group). Data
1163 points indicate biological replicates for each panel. A parametric T test was employed to
1164 assess significance between experimental groups. A *p* value < 0.05 was considered
1165 significant.

1166 **Figure 5. Accumulation of PD1^{+} CXCR5^{+} T_{FH}-like CD4^{+} T cells in the meninges**
1167 **during chronic *T. brucei* infection**

1168 **A)** Uniform manifold approximation and projection (UMAP) of 1,742 high-quality T cells
1169 from naïve (n = 147 cells) and infected meninges (n = 2,691 cells). **B)** Dot plot depicting
1170 the expression level of marker genes for all the T cell subsets identified in (**A**). The dot
1171 size corresponds to the proportion of cells expressing the marker genes, whereas the
1172 colour indicates the level of expression. **C)** as in (B) but depicting marker genes
1173 associated with T_{FH} cells. The dot size corresponds to the proportion of cells expressing

1174 the marker genes, whereas the colour indicates the level of expression. **D)**
1175 Representative flow cytometry analysis and quantification (**E**) the presence of CXCR5^{+}
1176 PD1^{+} CD4^{+} T cells in the murine meninges from naïve and 30dpi (*n* = 5 mice/group). Data
1177 points indicate biological replicates for each panel. A parametric T test was employed to
1178 assess significance between experimental groups. A *p* value < 0.05 is considered
1179 significant. **F)** *Ex vivo* T cell activation from naïve and infected murine meninges to
1180 measure the expression of PD-1 and IL-21. Unstimulated controls are also included. **G)**
1181 Quantification of the flow cytometry data from the *ex vivo* stimulation assay in (F). Data
1182 points indicate biological replicates for each panel and are representative from two
1183 independent experiments. A parametric T test was employed to assess significance
1184 between experimental groups. A *p* value < 0.05 was considered significant. **H)**
1185 Representative flow cytometry analysis and quantification **(I)** of the frequency of CD69^{+}
1186 CD4^{+} T cells in the murine meninges in response to infection. Data points indicate
1187 biological replicates for each panel and is representative from two independent
1188 experiments. A parametric T test was employed to assess significance between
1189 experimental groups. A *p* value < 0.05 was considered significant. **J)** Representative flow
1190 cytometry analysis to determine TCR engagement in CD4^{+} (top panel) and CD8^{+} (bottom
1191 panel) T cells *in situ* in the meninges during chronic infection with *T. brucei* using the
1192 Nur77^{GFP} reporter mouse line. **K)** Quantification of the flow cytometry data from **(J)**. A *p*
1193 value < 0.05 is considered significant. Data points indicate biological replicates for each
1194 panel and are representative from two independent experiments. A parametric T test was
1195 employed to assess significance between experimental groups. A *p* value < 0.05 is
1196 considered significant. **L)** Representative flow cytometry analysis to determine TCR
1197 engagement in CD4^{+} (top panel) in the Nur77^{Tempo} reporter mouse line. In this model, T
1198 cell activation dynamics can be discriminated between *de novo* (FT blue^{+}) versus
1199 historical (FT red^{+}) MHC-dependent TCR engagement. **M)** Quantification of the flow
1200 cytometry data from **(L)**. Data points indicate biological replicates for each panel and are
1201 representative from two independent experiments. A parametric T test was employed to
1202 assess significance between experimental groups. A *p* value < 0.05 was considered
1203 significant.

1204 **Figure 6. The murine meninges contain class-switched B cells in proximity to FDC-**
1205 **like cells.**

1206 **A)** Dotplot representing the expression level of top marker genes for the meningeal B
1207 cells, including *bona fide* markers of plasma cells (*Jchain, Prdm1, Sdc1, Xbp1, Ighm)* as

1208 well as activation and GC-like phenotype (*Cd24a, Cd38, Tnfrsf13c, Fas*). The dot size
1209 corresponds to the proportion of cells expressing the marker genes, whereas the colour
1210 indicates the level of expression. **B) Left panel;** Representative flow cytometry analysis
1211 (left panel) and quantification (right panel) to measure meningeal B cells ($CD19^+$ $CD138^-$
1212 cells), plasmablasts ($CD19^+$ $CD138^+$), and plasma cells ($CD19^-$ $CD138^+$). **Right panel;**
1213 quantification of flow cytometry data showing the expansion of meningeal $CD138^+$
1214 plasma cells in response to infection (*n* = 5 mice/group). Data points indicate biological
1215 replicates for each panel and are representative from two independent experiments. A
1216 parametric T test was employed to assess significance between experimental groups. A
1217 *p* value < 0.05 was considered significant. **C)** Representative flow cytometry analysis to
1218 determine BCR engagement on meningeal B cells *in situ* during chronic infection with *T.*
1219 *brucei* using the *Nur77*^{GFP} reporter mouse line. **D)** Quantification of flow cytometry data
1220 showing the reduction in the frequency of *Nur77*$^{GFP+}$ $CD19^+$ B cells in the meninges in
1221 response to infection (*n* = 5 mice/group). Data points indicate biological replicates for
1222 each panel and are representative from two independent experiments. A parametric T
1223 test was employed to assess significance between experimental groups. A *p* value < 0.05
1224 was considered significant. **E)** Representative flow cytometry analysis to determine the
1225 presence of GC-like B cells in the murine meninges based on the co-expression of GL7
1226 and CD95. **D)** Quantification of $GL7^+$ $CD95^+$ GC-like $CD19^+$ B cells in the meninges in
1227 response to infection (*n* = 5 mice/group). Data points indicate biological replicates for
1228 each panel and are representative from two independent experiments. A parametric T
1229 test was employed to assess significance between experimental groups. A *p* value < 0.05
1230 was considered significant. **G)** Representative flow cytometry analysis to determine the
1231 presence of IgG^+ $CD19^+$ B cells in the murine meninges in response to infection. **H)**
1232 Quantification of $GL7^+$ $CD95^+$ GC-like $CD19^+$ B cells in the meninges in response to
1233 infection (*n* = 4 mice/group). Data points indicate biological replicates for each panel and
1234 are representative from two independent experiments. A parametric T test was employed
1235 to assess significance between experimental groups. A *p* value < 0.05 was considered
1236 significant. **I)** Representative imaging analysis of whole-mount meninges from naïve (left)
1237 and infected (right) of $CD21/CD35^+$ follicular dendritic cells (green), as well as $CD3d^+$ T
1238 cells (red) and $B220^+$ B cells (purple). DAPI was included as nuclear staining. Scale = 50
1239 μm.

1240 **Figure 7. The murine meninges contain autoreactive IgG$^+$ antibody secreting cells**
1241 **(ASCs) during chronic *T. brucei* infection.**
1242 **A)** Representative ELISpot images depicting mouse brain-specific IgG$^+$ ASCs from naïve
1243 and infected murine meninges after 30dpi with *T. brucei*. **B)** Quantification of ELISpot
1244 results including total IgG$^+$, *T. brucei*-specific IgG$^+$, and mouse brain-specific IgG$^+$
1245 antibody secreting cells. Wells coated with BSA were included as negative controls. A p
1246 value < 0.05 was considered significant. **C)** Immunohistochemistry analysis to determine
1247 IgG$^+$ deposition in the mouse brain from naïve (left) and infected (right) mouse brain
1248 sagittal sections. The sections were stained with an anti-mouse IgG antibody coupled to
1249 HRP to measure the overall distribution of IgG in the brain. The asterisks denote areas
1250 of intense IgG deposition in the leptomeningeal space, as well as in the upper layers of
1251 the cerebral cortex, exclusively detected in the infected brain. Lm, leptomeninges; Ctx,
1252 cerebral cortex. **D) Left panel:** Representative Luxol fast blue (LFB) staining from naïve
1253 (left) and infected (right) animals at 30dpi as a proxy to measure myelin. Lower panels
1254 show the tissue heatmap of the mean pixel intensity. **Right panel:** Percentage of
1255 demyelination, calculated here as a reduction in the average of the relative LFB intensity,
1256 was calculated from three independent experiments (n = 3-4 mice/repeat). A parametric
1257 T test was employed to assess significance between experimental groups. A *p* value <
1258 0.05 was considered significant. **E)** Serum titters of mouse brain-specific IgM and IgG
1259 antibodies in naïve and infected samples as measured by ELISA. The dotted line
1260 represents the average of the optical density detected in naïve controls. A *p* value < 0.05
1261 was considered significant. **F)** Immunohistochemistry analysis to determine the presence
1262 of circulating brain autoreactive IgG antibodies in serum from naïve (top panels) and
1263 infected animals (middle panels) in the mouse brain from naïve (left) and infected (right)
1264 mouse coronal brain sections. Staining with the *T. brucei*-specific protein BiP (bottom
1265 panels) is also included to highlight accumulation of parasites in the lateral ventricles
1266 (arrowheads). **G)** ELISA analysis of human brain-autoreactive IgM and IgG antibodies in
1267 cerebrospinal fluid (CSF) from sleeping sickness patients from 1st stage and 2nd stage
1268 HAT (CSF dilution 1:400). Wells coated with BSA (5μg/ml) were included as controls. A
1269 *p* value < 0.05 was considered significant.
1270 **Figure 8. LTβ receptor signalling is critical to sustain FDC-like networks and**
1271 **autoreactive B cells in the murine meninges in response to *T. brucei* infection.**

1272 **A)** Dot plot depicting the expression level of *Ltb*, and its cognate receptors *Traf2* and *Ltbr*.
1273 The dot size corresponds to the proportion of cells expressing the marker genes, whereas
1274 the colour indicates the level of expression. **B)** Representative flow cytometry analysis
1275 depicting the expression of LTβ in $CD4^+$ T cells in naïve and mice chronically infected
1276 with *T. brucei* (30dpi). **C)** Quantification of flow cytometry analysis (n = 4 mice/group). A
1277 *p* value < 0.05 is considered significant. **D)** Overview of the experimental approach
1278 applied to block LTβR signalling *in vivo* during chronic *T. brucei* infection. **E)**
1279 Representative flow cytometry analysis of the murine meningeal stroma in naïve and
1280 mice chronically infected with *T. brucei* (30dpi). FDC-like cells were gated from the double
1281 $CD45^-$ mesenchymal cells. **F)** Quantification of the different components of the stroma in
1282 naïve and infected meningeal preparations (n = 4 mice/group). A *p* value < 0.05 was
1283 considered significant. FRC, fibroblast reticular cell; LEC, lymphatic endothelial cell; BEC,
1284 blood endothelial cell; DN, double negative. **G)** Quantification of ELISpot results including
1285 total IgG^+ (left panel), *T. brucei*-specific IgG^+ (middle panel), and mouse brain-specific
1286 IgG^+ antibody secreting cells (right panel) in naïve mice, mice treated with an irrelevant
1287 IgG2a antibody, and mice treated with LTBR-Ig (*n* = 4 - 9 mice/group). A *p* value < 0.05
1288 was considered significant. **H)** Representative immunofluorescence analysis of whole
1289 mount meningeal preparation labelling $CD138^+$ plasma cells (red) and $CD21/CD35^+$
1290 FDC-like cells (green) in naïve or at 30 days post-infection. Each of the fluorescent
1291 channels are shown individually, and DAPI was included to detect cell nuclei. Scale bar
1292 = 50 μm. **I) Left panel:** Representative Luxol fast blue (LFB) staining from naïve (left)
1293 and infected (right) animals at 30dpi as a proxy to measure myelin. **Middle panel:** The
1294 tissue heatmap of the mean pixel intensity is also shown. **Right panel:** Percentage of
1295 demyelination, calculated here as a reduction in the mean grey intensity of the LFB
1296 staining, was calculated from two independent experiments (n = 4-5 mice/experiment).
1297 A parametric ANOVA with multiple comparisons was employed to assess significance
1298 between experimental groups. A *p* value < 0.05 was considered significant.

1299 **Figure 9. Targeted antigen screening identified shared host antigens detected by**
1300 **autoreactive antibodies in mouse serum and human CSF in response to *T. brucei***
1301 **infection.**

1302 **A)** Heatmap depicting the normalised fluorescent signal-to-noise ratio for 18 antigens
1303 significantly detected by mouse serum from infected animals at 30dpi (*n* = 3 mice)
1304 compared to naïve controls (*n* = 3 mice). The selected genes were chosen based on

1305 significant level in pairwise comparisons between naïve and infected samples using a
1306 parametric two-sided *T* test. Pairwise comparisons resulting in a *p* value < 0.05 were
1307 considered to be significant. **B)** As in (A) but depicting a total of 51 antigens significantly
1308 and exclusively detected in the cerebrospinal fluid (CSF) from 2nd stage sleeping sickness
1309 patients (*n* = 4 patients) compared to both 1st stage sleeping sickness patients (*n* = 3
1310 patients) and healthy donors (*n* = 2 donors). **C)** Ven diagram depicting host antigens
1311 identified in this screening that were commonly detected by autoreactive IgG antibodies
1312 in both mouse serum and human CSF, as well as those antigens that showed specie-
1313 specific responses. A table summarising the common host antigens and the disease they
1314 are often associated with is also included. **D)** ELISA analysis to examine the presence of
1315 anti-MBP IgG autoantibodies in human serum from patients with an active *T. brucei*
1316 gambiense infection ("cases") or post-treatment ("treated"), as well as healthy African
1317 controls ("controls"). A parametric ANOVA test with multiple comparison was used to
1318 estimate statistically significant pairwise comparisons. A *p* value < 0.05 was considered
1319 significant.

1320 **Figure 10. Suramin treatment prevents the expansion of GL7$^+$ CD95$^+$ GC-like B cells**
1321 **and the IgG deposition in the mouse brain.**

1322 **A)** Overview of the experimental approach applied to prevent the CNS stage of the
1323 disease using suramin. **B)** Estimation of *T. brucei* burden in the murine brain using RT-
1324 PCR analysis to detect the parasite-specific *Pfr2* gene in naïve brain specimens and
1325 infected but untreated animals (*n* = 5 mice/group), as well as cured (*n* = 4 mice) and
1326 relapsing animals (*n* = 4 mice). These data are representative of two independent
1327 experiments. A parametric ANOVA test with multiple comparison was used to estimate
1328 statistically significant pairwise comparisons. A *p* value < 0.05 was considered significant.
1329 **C)** Immunohistochemistry staining of the *T. brucei*-specific protein BiP in brain sections
1330 from the same experimental groups as in (B). **D)** Representative flow cytometry analysis
1331 of GL7$^+$ CD95$^+$ GC-like CD19$^+$ B cells in the murine meninges from the same
1332 experimental groups as in (B). The gating strategy to identify meningeal B cells is shown
1333 in S2C figure. **E)** Quantification of GL7$^+$ CD95$^+$ GC-like CD19$^+$ B cells in the murine
1334 meninges from the same groups as in (B). A parametric ANOVA test with multiple
1335 comparison was used to estimate statistically significant pairwise comparisons. A *p* value
1336 < 0.05 was considered significant. **F)** Representative immunohistochemistry micrographs
1337 comparing IgG$^+$ deposition in brains from naïve mice and infected but untreated mice, as
1338 well as cured and relapsed mice post suramin-treatment. Images are representative from

1339 two independent experiments. Scale bar = 1 mm. **G)** ELISA test to determine serum IgG
1340 titters of mouse brain-specific autoantibodies in the experimental groups in (B). Data are
1341 representative from two independent experiments. A parametric ANOVA test with
1342 multiple comparison was used to estimate statistically significant pairwise comparisons.
1343 A *p* value < 0.05 was considered significant. **H) Upper panel**: representative Luxol fast
1344 blue (LFB) staining as a proxy to measure myelin in brain specimens from naïve and
1345 infected mice, as well as infected mice treated with suramin, including relapsed and cured
1346 animals. Lower panel: Tissue heatmap representing the mean grey value (MGV) for the
1347 LFB staining. The calibration bar was set up so that the lowest level is 0 and the maximum
1348 MGV is 255. Scale bar = 1 mm. **I)** Percentage of demyelination, calculated here as a
1349 reduction in the mean grey intensity of the LFB staining, was calculated from two
1350 independent experiments (n = 4-10 mice/experiment). Parametric pairwise comparisons
1351 using one-sided *T* test was employed to assess significance between experimental
1352 groups. A *p* value < 0.05 was considered significant.
1353
1354 **Supplementary figures**
1355 **Supplementary figure 1. Quality control measurements of the murine single cell**
1356 **CyTOF and transcriptomics dataset. A)** Representative flow cytometry analysis of the
1357 input and flowthrough for the removal of circulating $CD45^+$ immune cells using magnetic
1358 sorting. **B)** Identification of $CD45^+$ cells in the CyTOF murine meninges dataset. C)
1359 Uniform manifold approximation and projection (UMAP) of the CyTOF dataset from
1360 samples (left panel; BC10-BC15: naïve; BC11-BC20: 30dpi) experimental groups (right
1361 panel) after $CD45^+$ cell clustering. **D)** Number of Unique molecular identifies (UMIs),
1362 genes, mitochondrial reads, and library complexity (Log10 UMIs/gene) after applying
1363 filtering parameters. **E)** Clustree output representing the relationship between different
1364 cell clusters at various levels of resolution using the function *FindClusters*.
1365 **Supplementary figure 2. Gating strategies for flow cytometry analysis.** Gating
1366 strategies to identification stromal cells (**A**), resident myeloid cells (**B**), resident $CD4^+$ and
1367 $CD8^+$ $\alpha\beta$ T cells (**C**), and B cells/plasma cells (**D**).
1368 **Supplementary figure 3. Expression of lymphoid stromal cells marker genes within**
1369 **the dura fibroblasts. A) Left:** Expression level of Marker genes typically associated with
1370 fibroblast reticular cells (FRCs). **Right:** Expression level of genes encoding for secreted
1371 factors resealed by FRCs. **B)** Marker genes moderately (left) or lowly (right) expressed

1372 typically associated with B zone reticular cells (BRC). **C)** Broad classification of the
1373 various fibroblasts clusters as FRC- or BRC-like clusters based on the marker genes
1374 shown in (A) and (B). In all cases, the size of the dot represents the proportion of cells
1375 expressing the markers indicated in each plot. **D)** Feature plots depicting the results from
1376 module scoring of the different categories within the MatrisomeDB including collagen and
1377 proteoglycan production and deposition, and secreted factors. **E**) Masson's trichrome
1378 staining depicting collagen deposition (blue), and keratin (pink) in sagittal skull sections
1379 containing dura meninges from naïve and infected animals. Scale bar = 50 μm.
1380 **Supplementary figure 5. Local T cell activation in the meninges in response to T.**
1381 **brucei infection using the *Nur77*^{Tempo} reporter mice. A)** Representative flow cytometry
1382 analysis to determine TCR engagement in CD8$^+$ T cells in the *Nur77*^{Tempo} reporter mouse
1383 line. In this model, T cell activation dynamics can be discriminated between *de novo* (FT
1384 blue$^+$) versus historical (FT red$^+$) MHC-dependent TCR engagement. **B)** Quantification of
1385 the flow cytometry data from **(A)** focusing exclusively on FT blue$^+$ or FT red$^+$ CD8$^+$ T cells.
1386 Data points indicate biological replicates for each panel and are representative from two
1387 independent experiments. A two-sided, parametric T test was employed to assess
1388 significance between experimental groups. A p value < 0.05 was considered significant.
1389 **C)** Representative flow cytometry analysis to determine TCR engagement in CD69$^+$ CD4$^+$
1390 T cells in the *Nur77*^{Tempo} reporter mouse line. **D)** Quantification of the flow cytometry data
1391 from **(A)** focusing exclusively on FT blue$^+$ or FT red$^+$ CD69$^+$ CD4$^+$ T cells. Data points
1392 indicate biological replicates for each panel and are representative from two independent
1393 experiments. A two-sided, parametric T test was employed to assess significance
1394 between experimental groups. A p value < 0.05 was considered significant.
1395 **Supplementary figure 5. Meningeal lymphoid-like aggregates in response to *T.***
1396 ***brucei* infection.** Additional imaging analysis of whole-mount meninges from naïve (left)
1397 and infected (right) of CD21/CD35$^+$ follicular dendritic cells (green), as well as CD3d$^+$ T
1398 cells (red) and B220$^+$ B cells (purple). The data correspond to data obtained from two
1399 independent meningeal preparations; Replicate 1 and 2 shown in top and bottom panels,
1400 respectively. DAPI was included as nuclear staining. Scale = 100 μm.
1401 **Supplementary figure 6. Chronic *T. brucei* infection induces demyelination in the**
1402 **CNS. A) Left:** Representative ELISpot images depicting mouse brain-specific IgG$^+$ ASCs
1403 from naïve and infected murine meninges and splenocytes after 30dpi with *T. brucei*.
1404 **Right:** Quantification of ELISpot results from mouse brain-specific IgG$^+$ ASCs in

1405 meningeal preps and splenocytes (n = 4 mice/group). A p value < 0.05 is considered
1406 significant. Luxol Fast blue staining to determine myelination in naïve (**B**) and infected
1407 (**C**) coronal brain sections. Insets how areas of the cortex (Ctx), internal capsule (IC), and
1408 thalamus (Th).

1409 **Supplementary figure 7. LTβR signalling blockade results in uncontrolled**
1410 **parasitaemia and IgM$^+$ B cell accumulation in the meninges.** Parasitaemia (**A**) and
1411 clinical scoring (**B**) of *T. brucei*-infected mice treated with the LTβR-Ig fusion protein (blue
1412 line). *T. brucei*-infected mice alone (green line) or infected mice treated with an irrelevant
1413 IgG2a antibody (orange line) were used as controls. For parasitaemia, an ANOVA test
1414 with multiple comparisons was conducted. For clinical scoring, pairwise comparisons
1415 were conducted using a non-parametric T test. In all cases, a p value < 0.05 was
1416 considered significant. Representative ELISpot results for meningeal IgM$^+$ (**C**) and IgG$^+$
1417 (**D**) antibody secreting cells (ASCs), including total ASCs (top panel), *T. brucei*-specific
1418 ASCs (middle panel), and mouse brain-specific ASCs (bottom panel). The number of
1419 spots detected by the automated analysis software is also included. **E**) Quantification of
1420 ELISpot results including total IgM$^+$ (left panel), *T. brucei*-specific IgM$^+$ (middle panel),
1421 and mouse brain-specific IgM$^+$ antibody secreting cells (right panel) in naïve mice, mice
1422 treated with an irrelevant IgG2a antibody, and mice treated with LTβR-Ig (n = 4 – 9
1423 mice/group). A p value < 0.05 was considered significant. F) Luxol Fast blue (LFB)
1424 staining to determine myelination in sagittal brain sections from infected mice treated with
1425 LTBR-Ig or with an irrelevant IgG2a antibody control naïve (2 replicates per condition).
1426 Insets how selected cortical areas. Ctx, Cortex. Scale bar: 1mm (whole image) or 50 μm
1427 (insets).

1428 **Supplementary figure 8. Targeted antigen screening identified shared host**
1429 **antigens detected by autoreactive antibodies in mouse serum and human CSF in**
1430 **response to *T. brucei* infection.** Heatmap depicting the normalised signal-to-noise ratio
1431 for IgG binding against a panel of 120 host antigens. The data was acquired from naïve
1432 and infected murine serum (**A**) at 30dpi (n = 3 mice/group), and human CSF (B) from
1433 healthy donors (n = 2 donors), 1st stage sleeping sickness patients (n = 3 samples), and
1434 2nd stage sleeping sickness patients (n = 4 samples). The asterisks denote samples that
1435 were statistically significant in a pairwise comparison analysis using parametric T test. A
1436 p value < 0.05 is considered significant.

1437 **Supplementary Tables**

1438 **Table S1.** Quality control including mean reads per cell and median genes per cell before
1439 and after filtering out low quality cell types.
1440 **Table S2.** Overview of the major cell types detected in the single cell dataset (resolution
1441 of 0.7). The total number of cells per cluster, percentages, and marker genes are also
1442 included.
1443 **Table S3.** Marker genes identified for the cells within the fibroblast clusters obtained after
1444 subsetting (resolution = 0.6). The total number of cells per cluster, percentages, and
1445 marker genes are also included.
1446 **Table S4.** Marker genes identified for the cells within the mononuclear phagocytes (MNP)
1447 cluster obtained after subsetting (resolution = 0.3). The total number of cells per cluster,
1448 percentages, and marker genes are also included.
1449 **Table S5.** Marker genes identified for the cells within the T cell cluster obtained after
1450 subsetting (resolution = 0.7). The total number of cells per cluster, percentages, and
1451 marker genes are also included.
1452 **Table S6.** Metadata associated with the human cerebrospinal fluid samples included for
1453 autoantibodies against human brain lysates by ELISA.
1454 **Table S7.** Normalised signal-to-noise ratio (SNR) of targeted host antigen screening
1455 conducted using mouse serum and human CSF. The SNR values for each of the 120
1456 antigens are included, as well as a parametric T test conducted to determine the level of
1457 significant in pairwise comparisons between infected mice and naïve controls, or between
1458 2nd stage sleeping sickness CSF samples and 1st stage sleeping sickness or healthy
1459 donors.
1460

1461 **Bibliography**

1462 1. Jacob, L. *et al.* Conserved meningeal lymphatic drainage circuits in mice and
1463 humans. *J. Exp. Med.* **219**, e20220035 (2022).
1464 2. Rustenhoven, J. *et al.* Functional characterization of the dural sinuses as a
1465 neuroimmune interface. *Cell* **184**, 1000-1016.e27 (2021).
1466 3. Antila, S. *et al.* Development and plasticity of meningeal lymphatic vessels. *J. Exp.*
1467 *Med.* **214**, 3645–3667 (2017).

1468 4. Rustenhoven, J. *et al.* Age-related alterations in meningeal immunity drive impaired
1469 CNS lymphatic drainage. *J. Exp. Med.* **220**, e20221929 (2023).
1470 5. Bolte, A. C. *et al.* The meningeal transcriptional response to traumatic brain injury
1471 and aging. *eLife* **12**, e81154 (2023).
1472 6. Ma, T., Wang, F., Xu, S. & Huang, J. H. Meningeal immunity: Structure, function
1473 and a potential therapeutic target of neurodegenerative diseases. *Brain. Behav.*
1474 *Immun.* **93**, 264–276 (2021).
1475 7. Merlini, A. *et al.* Distinct roles of the meningeal layers in CNS autoimmunity. *Nat.*
1476 *Neurosci.* **25**, 887–899 (2022).
1477 8. Ampie, L. & McGavern, D. B. Immunological defense of CNS barriers against
1478 infections. *Immunity* **55**, 781–799 (2022).
1479 9. Coles, J. A. *et al.* Intravital Imaging of a Massive Lymphocyte Response in the
1480 Cortical Dura of Mice after Peripheral Infection by Trypanosomes. *PLoS Negl. Trop.*
1481 *Dis.* **9**, e0003714 (2015).
1482 10. Vlaminck, K. D. *et al.* Differential plasticity and fate of brain-resident and recruited
1483 macrophages during the onset and resolution of neuroinflammation. *Immunity* **55**,
1484 2085-2102.e9 (2022).
1485 11. Coles, J. A., Stewart-Hutchinson, P. J., Myburgh, E. & Brewer, J. M. The mouse
1486 cortical meninges are the site of immune responses to many different pathogens,
1487 and are accessible to intravital imaging. *Methods San Diego Calif* **127**, 53–61
1488 (2017).
1489 12. Rodgers, J., Bradley, B. & Kennedy, P. G. E. Delineating neuroinflammation,
1490 parasite CNS invasion, and blood-brain barrier dysfunction in an experimental
1491 murine model of human African trypanosomiasis. *Methods San Diego Calif* **127**, 79–
1492 87 (2017).

1493 13. Quintana, J. F. *et al.* Single cell and spatial transcriptomic analyses reveal
1494 microglia-plasma cell crosstalk in the brain during Trypanosoma brucei infection.
1495 *Nat. Commun.* **13**, 5752 (2022).
1496 14. Blum, J., Schmid, C. & Burri, C. Clinical aspects of 2541 patients with second stage
1497 human African trypanosomiasis. *Acta Trop.* **97**, 55–64 (2006).
1498 15. Kazumba, L. M., Kaka, J.-C. T., Ngoyi, D. M. & Tshala-Katumbay, D. Mortality
1499 trends and risk factors in advanced stage-2 Human African Trypanosomiasis: A
1500 critical appraisal of 23 years of experience in the Democratic Republic of Congo.
1501 *PLoS Negl. Trop. Dis.* **12**, e0006504 (2018).
1502 16. Mudji, J. *et al.* Gambiense Human African Trypanosomiasis Sequelae after
1503 Treatment: A Follow-Up Study 12 Years after Treatment. *Trop. Med. Infect. Dis.* **5**,
1504 10 (2020).
1505 17. Rijo-Ferreira, F. *et al.* Sleeping Sickness Disrupts the Sleep-Regulating Adenosine
1506 System. *J. Neurosci. Off. J. Soc. Neurosci.* **40**, 9306–9316 (2020).
1507 18. Rijo-Ferreira, F. *et al.* Sleeping sickness is a circadian disorder. *Nat. Commun.* **9**, 62
1508 (2018).
1509 19. Lundkvist, G. B., Hill, R. H. & Kristensson, K. Disruption of Circadian Rhythms in
1510 Synaptic Activity of the Suprachiasmatic Nuclei by African Trypanosomes and
1511 Cytokines. *Neurobiol. Dis.* **11**, 20–27 (2002).
1512 20. Cornford, E. M., Freeman, B. J. & MacInnis, A. J. Physiological Relationships and
1513 Circadian Periodicities in Rodent Trypanosomes. *Trans. R. Soc. Trop. Med. Hyg.*
1514 **70**, 238–243 (1976).
1515 21. Manzo, A. *et al.* Systematic microanatomical analysis of CXCL13 and CCL21 in situ
1516 production and progressive lymphoid organization in rheumatoid synovitis. *Eur. J.*
1517 *Immunol.* **35**, 1347–1359 (2005).

1518 22. Chang, A. *et al.* In situ B cell-mediated immune responses and tubulointerstitial
1519 inflammation in human lupus nephritis. *J. Immunol. Baltim. Md 1950* **186**, 1849–
1520 1860 (2011).
1521 23. Fridman, W. H. *et al.* B cells and tertiary lymphoid structures as determinants of
1522 tumour immune contexture and clinical outcome. *Nat. Rev. Clin. Oncol.* **19**, 441–457
1523 (2022).
1524 24. Pitzalis, C., Jones, G. W., Bombardieri, M. & Jones, S. A. Ectopic lymphoid-like
1525 structures in infection, cancer and autoimmunity. *Nat. Rev. Immunol.* **14**, 447–462
1526 (2014).
1527 25. Stock, A. D. *et al.* Tertiary lymphoid structures in the choroid plexus in
1528 neuropsychiatric lupus. *JCI Insight* **4**, e124203.
1529 26. Pikor, N. B., Prat, A., Bar-Or, A. & Gommerman, J. L. Meningeal Tertiary Lymphoid
1530 Tissues and Multiple Sclerosis: A Gathering Place for Diverse Types of Immune
1531 Cells during CNS Autoimmunity. *Front. Immunol.* **6**, (2016).
1532 27. Rodriguez, A. B. *et al.* Immune mechanisms orchestrate tertiary lymphoid structures
1533 in tumors via cancer-associated fibroblasts. *Cell Rep.* **36**, 109422 (2021).
1534 28. Ransohoff, R. M. Multiple sclerosis: role of meningeal lymphoid aggregates in
1535 progression independent of relapse activity. *Trends Immunol.* **44**, 266–275 (2023).
1536 29. Jalkanen, S. & Salmi, M. Lymphatic endothelial cells of the lymph node. *Nat. Rev.*
1537 *Immunol.* **20**, 566–578 (2020).
1538 30. Krishnamurty, A. T. & Turley, S. J. Lymph node stromal cells: cartographers of the
1539 immune system. *Nat. Immunol.* **21**, 369–380 (2020).
1540 31. von Andrian, U. H. & Mempel, T. R. Homing and cellular traffic in lymph nodes. *Nat.*
1541 *Rev. Immunol.* **3**, 867–878 (2003).

1542 32. Phan, T. G., Grigorova, I., Okada, T. & Cyster, J. G. Subcapsular encounter and
1543 complement-dependent transport of immune complexes by lymph node B cells. *Nat.*
1544 *Immunol.* **8**, 992–1000 (2007).
1545 33. Da Mesquita, S., Fu, Z. & Kipnis, J. The Meningeal Lymphatic System: A New
1546 Player in Neurophysiology. *Neuron* **100**, 375–388 (2018).
1547 34. Louveau, A. *et al.* CNS lymphatic drainage and neuroinflammation are regulated by
1548 meningeal lymphatic vasculature. *Nat. Neurosci.* **21**, 1380–1391 (2018).
1549 35. Le Ray, D., Barry, J. D., Easton, C. & Vickerman, K. First tsetse fly transmission of
1550 the 'AnTat' serodeme of Trypanosoma brucei. *Ann. Soc. Belg. Med. Trop.* **57**, 369–
1551 381 (1977).
1552 36. Herbert, W. J. & Lumsden, W. H. Trypanosoma brucei: a rapid 'matching' method
1553 for estimating the host's parasitemia. *Exp. Parasitol.* **40**, 427–431 (1976).
1554 37. Intravascular staining for discrimination of vascular and tissue leukocytes | Springer
1555 Nature Experiments.
1556 https://experiments.springernature.com/articles/10.1038/nprot.2014.005.
1557 38. Hao, Y. *et al.* Integrated analysis of multimodal single-cell data. *Cell* **184**, 3573-
1558 3587.e29 (2021).
1559 39. Hafemeister, C. & Satija, R. Normalization and variance stabilization of single-cell
1560 RNA-seq data using regularized negative binomial regression. *Genome Biol.* **20**,
1561 296 (2019).
1562 40. Clustering trees: a visualization for evaluating clusterings at multiple resolutions |
1563 GigaScience | Oxford Academic.
1564 https://academic.oup.com/gigascience/article/7/7/giy083/5052205.

1565 41. Efremova, M., Vento-Tormo, M., Teichmann, S. A. & Vento-Tormo, R.
1566 CellPhoneDB: inferring cell-cell communication from combined expression of multi-
1567 subunit ligand-receptor complexes. *Nat. Protoc.* **15**, 1484–1506 (2020).
1568 42. Brioschi, S. *et al.* Heterogeneity of meningeal B cells reveals a lymphopoietic niche
1569 at the CNS borders. *Science* **373**, eabf9277 (2021).
1570 43. Shao, X., Taha, I. N., Clauser, K. R., Gao, Y. (Tom) & Naba, A. MatrisomeDB: the
1571 ECM-protein knowledge database. *Nucleic Acids Res.* **48**, D1136–D1144 (2020).
1572 44. Manglani, M., Gossa, S. & McGavern, D. B. Leukocyte Isolation from Brain, Spinal
1573 Cord, and Meninges for Flow Cytometric Analysis. *Curr. Protoc. Immunol.* **121**, e44
1574 (2018).
1575 45. Browning, J. L. *et al.* Characterization of lymphotoxin-alpha beta complexes on the
1576 surface of mouse lymphocytes. *J. Immunol. Baltim. Md 1950* **159**, 3288–3298
1577 (1997).
1578 46. Fitzpatrick, Z. *et al.* Gut-educated IgA plasma cells defend the meningeal venous
1579 sinuses. *Nature* **587**, 472–476 (2020).
1580 47. Dorrier, C. E., Jones, H. E., Pintarić, L., Siegenthaler, J. A. & Daneman, R.
1581 Emerging roles for CNS fibroblasts in health, injury and disease. *Nat. Rev.*
1582 *Neurosci.* **23**, 23–34 (2022).
1583 48. DeSisto, J. *et al.* Single-Cell Transcriptomic Analyses of the Developing Meninges
1584 Reveal Meningeal Fibroblast Diversity and Function. *Dev. Cell* **54**, 43-59.e4 (2020).
1585 49. Jones, H. E. *et al.* Meningeal origins and dynamics of perivascular fibroblast
1586 development on the mouse cerebral vasculature. 2023.03.23.533982 Preprint at
1587 https://doi.org/10.1101/2023.03.23.533982 (2023).
1588 50. Di Carlo, S. E. & Peduto, L. The perivascular origin of pathological fibroblasts. *J.*
1589 *Clin. Invest.* **128**, 54–63.

1590 51. The origin of subdural neomembranes. I. Fine structure of the dura-arachnoid
1591 interface in man. - PMC. https://www.ncbi.nlm.nih.gov/pmc/articles/PMC2018597/.
1592 52. Schiavinato, A., Przyklenk, M., Kobbe, B., Paulsson, M. & Wagener, R. Collagen
1593 type VI is the antigen recognized by the ER-TR7 antibody. *Eur. J. Immunol.* **51**,
1594 2345–2347 (2021).
1595 53. Aldh1a2+ fibroblastic reticular cells regulate lymphocyte recruitment in omental
1596 milky spots | Journal of Experimental Medicine | Rockefeller University Press.
1597 https://rupress.org/jem/article/220/5/e20221813/213908/Aldh1a2-fibroblastic-
1598 reticular-cells-regulate.
1599 54. DeSisto, J. *et al.* A cellular atlas of the developing meninges reveals meningeal
1600 fibroblast diversity and function. 648642 Preprint at https://doi.org/10.1101/648642
1601 (2019).
1602 55. Remsik, J. *et al.* Characterization, isolation, and in vitro culture of leptomeningeal
1603 fibroblasts. *J. Neuroimmunol.* **361**, (2021).
1604 56. Pietilä, R. *et al.* Molecular anatomy of adult mouse leptomeninges. *Neuron* (2023)
1605 doi:10.1016/j.neuron.2023.09.002.
1606 57. Cinti, I. & Denton, A. E. Lymphoid stromal cells—more than just a highway to
1607 humoral immunity. *Oxf. Open Immunol.* **2**, iqab011 (2021).
1608 58. Conserved stromal–immune cell circuits secure B cell homeostasis and function |
1609 Nature Immunology. https://www.nature.com/articles/s41590-023-01503-3.
1610 59. Krautler, N. J. *et al.* Follicular Dendritic Cells Emerge from Ubiquitous Perivascular
1611 Precursors. *Cell* **150**, 194–206 (2012).
1612 60. McCulloch, L. *et al.* Follicular Dendritic Cell-Specific Prion Protein (PrPc) Expression
1613 Alone Is Sufficient to Sustain Prion Infection in the Spleen. *PLOS Pathog.* **7**,
1614 e1002402 (2011).

1615 61. Waddell, L. A. *et al.* ADGRE1 (EMR1, F4/80) Is a Rapidly-Evolving Gene Expressed
1616 in Mammalian Monocyte-Macrophages. *Front. Immunol.* **9**, 2246 (2018).
1617 62. Van Hove, H. *et al.* A single-cell atlas of mouse brain macrophages reveals unique
1618 transcriptional identities shaped by ontogeny and tissue environment. *Nat. Neurosci.*
1619 **22**, 1021–1035 (2019).
1620 63. Moran, A. E. *et al.* T cell receptor signal strength in Treg and iNKT cell development
1621 demonstrated by a novel fluorescent reporter mouse. *J. Exp. Med.* **208**, 1279–1289
1622 (2011).
1623 64. Elliot, T. A. E. *et al.* Nur77-Tempo mice reveal T cell steady state antigen
1624 recognition. *Discov. Immunol.* **1**, kyac009 (2022).
1625 65. Jennings, E. *et al.* Nr4a1 and Nr4a3 Reporter Mice Are Differentially Sensitive to T
1626 Cell Receptor Signal Strength and Duration. *Cell Rep.* **33**, 108328 (2020).
1627 66. Barinov, A. *et al.* Essential role of immobilized chemokine CXCL12 in the regulation
1628 of the humoral immune response. *Proc. Natl. Acad. Sci. U. S. A.* **114**, 2319–2324
1629 (2017).
1630 67. Cheng, Q. *et al.* CXCR4–CXCL12 interaction is important for plasma cell homing
1631 and survival in NZB/W mice. *Eur. J. Immunol.* **48**, 1020–1029 (2018).
1632 68. Pilzecker, B. & Jacobs, H. Mutating for Good: DNA Damage Responses During
1633 Somatic Hypermutation. *Front. Immunol.* **10**, (2019).
1634 69. Mueller, J., Matloubian, M. & Zikherman, J. An in vivo reporter reveals active B cell
1635 receptor signaling in the germinal center. *J. Immunol. Baltim. Md 1950* **194**, 2993–
1636 2997 (2015).
1637 70. Brooks, J. F. *et al.* Negative feedback by NUR77/Nr4a1 restrains B cell clonal
1638 dominance during early T-dependent immune responses. *Cell Rep.* **36**, 109645
1639 (2021).

1640 71. Lymphotoxin-Dependent B Cell-FRC Crosstalk Promotes De Novo Follicle
1641 Formation and Antibody Production following Intestinal Helminth Infection -
1642 PubMed. https://pubmed.ncbi.nlm.nih.gov/27160906/.
1643 72. Tang, H., Zhu, M., Qiao, J. & Fu, Y.-X. Lymphotoxin signalling in tertiary lymphoid
1644 structures and immunotherapy. *Cell. Mol. Immunol.* **14**, 809–818 (2017).
1645 73. Koroleva, E. P., Fu, Y.-X. & Tumanov, A. V. Lymphotoxin in physiology of lymphoid
1646 tissues - implication for antiviral defense. *Cytokine* **101**, 39–47 (2018).
1647 74. James Bates, R. E. *et al.* Lymphotoxin-alpha expression in the meninges causes
1648 lymphoid tissue formation and neurodegeneration. *Brain* **145**, 4287–4307 (2022).
1649 75. Browning, J. L. *et al.* Lymphotoxin-β Receptor Signaling Is Required for the
1650 Homeostatic Control of HEV Differentiation and Function. *Immunity* **23**, 539–550
1651 (2005).
1652 76. Alfituri, O. A., Bradford, B. M., Paxton, E., Morrison, L. J. & Mabbott, N. A. Influence
1653 of the Draining Lymph Nodes and Organized Lymphoid Tissue Microarchitecture on
1654 Susceptibility to Intradermal Trypanosoma brucei Infection. *Front. Immunol.* **11**,
1655 1118 (2020).
1656 77. Pisetsky, D. S. Pathogenesis of autoimmune disease. *Nat. Rev. Nephrol.* **19**, 509–
1657 524 (2023).
1658 78. Zhang, F., Gao, X., Liu, J. & Zhang, C. Biomarkers in autoimmune diseases of the
1659 central nervous system. *Front. Immunol.* **14**, (2023).
1660 79. Theofilopoulos, A. N., Kono, D. H. & Baccala, R. The multiple pathways to
1661 autoimmunity. *Nat. Immunol.* **18**, 716–724 (2017).
1662 80. Amin, D. N., Masocha, W., Ngan'dwe, K., Rottenberg, M. & Kristensson, K. Suramin
1663 and minocycline treatment of experimental African trypanososmiasis at an early
1664 stage of parasite brain invasion. *Acta Trop.* **106**, 72–74 (2008).

1665 81. Buechler, M. B. *et al.* Cross-tissue organization of the fibroblast lineage. *Nature* **593**,
1666 575–579 (2021).
1667 82. Lendahl, U., Muhl, L. & Betsholtz, C. Identification, discrimination and heterogeneity
1668 of fibroblasts. *Nat. Commun.* **13**, 3409 (2022).
1669 83. Plikus, M. V. *et al.* Fibroblasts: Origins, definitions, and functions in health and
1670 disease. *Cell* **184**, 3852–3872 (2021).
1671 84. Targeting TLR4 during vaccination boosts MAdCAM-1+ lymphoid stromal cell
1672 activation and promotes the aged germinal center response | Science Immunology.
1673 https://www.science.org/doi/10.1126/sciimmunol.abk0018.
1674 85. Hsu, M. *et al.* Neuroinflammation-induced lymphangiogenesis near the cribriform
1675 plate contributes to drainage of CNS-derived antigens and immune cells. *Nat.*
1676 *Commun.* **10**, 229 (2019).
1677 86. Blockade of VEGFR3 signaling leads to functional impairment of dural lymphatic
1678 vessels without affecting autoimmune neuroinflammation | Science Immunology.
1679 https://www.science.org/doi/10.1126/sciimmunol.abq0375.
1680 87. Longitudinal analysis reveals high prevalence of Epstein-Barr virus associated with
1681 multiple sclerosis | Science. https://www.science.org/doi/10.1126/science.abj8222.
1682 88. Guillaume, M.-P., Hermanus, N., Demulder, A., Servais, G. & Karmali, R. Specific
1683 autoantibodies of SLE, such as anti-Ku, anti-ribosome Po and anti-membrane DNA
1684 autoantibodies, in a case of human African trypanosomiasis. *Rheumatology* **42**,
1685 1568–1569 (2003).
1686 89. Radwanska, M. *et al.* Antibodies raised against the flagellar pocket fraction of
1687 Trypanosoma brucei preferentially recognize HSP60 in cDNA expression library.
1688 *Parasite Immunol.* **22**, 639–650 (2000).

1689 90. Radwanska, M. *et al.* Comparative Analysis of Antibody Responses against HSP60,
1690 Invariant Surface Glycoprotein 70, and Variant Surface Glycoprotein Reveals a
1691 Complex Antigen-Specific Pattern of Immunoglobulin Isotype Switching during
1692 Infection by *Trypanosoma brucei*. *Infect. Immun.* **68**, 848–860 (2000).
1693 91. Ayed, Z. *et al.* Detection and Characterization of Autoantibodies Directed against
1694 Neurofilament Proteins in Human African Trypanosomiasis. *Am. J. Trop. Med. Hyg.*
1695 **57**, 1–6 (1997).
1696 92. Kazyumba, G., Berney, M., Brighouse, G., Cruchaud, A. & Lambert, P. H.
1697 Expression of the B cell repertoire and autoantibodies in human African
1698 trypanosomiasis. *Clin. Exp. Immunol.* **65**, 10–18 (1986).
1699 93. Schafflick, D. *et al.* Single-cell profiling of CNS border compartment leukocytes
1700 reveals that B cells and their progenitors reside in non-diseased meninges. *Nat.*
1701 *Neurosci.* **24**, 1225–1234 (2021).
1702 94. Kovacs, M. A. *et al.* Meningeal lymphatic drainage promotes T cell responses
1703 against Toxoplasma gondii but is dispensable for parasite control in the brain. *eLife*
1704 **11**, e80775 (2022).
1705 95. De Niz, M. *et al.* Organotypic endothelial adhesion molecules are key for
1706 Trypanosoma brucei tropism and virulence. *Cell Rep.* **36**, 109741 (2021).
1707 96. Philip, K. A., Dascombe, M. J., Fraser, P. A. & Pentreath, V. W. Blood-brain barrier
1708 damage in experimental African trypanosomiasis. *Ann. Trop. Med. Parasitol.* **88**,
1709 607–616 (1994).
1710 97. Rodgers, J. *et al.* Magnetic resonance imaging to assess blood-brain barrier
1711 damage in murine trypanosomiasis. *Am. J. Trop. Med. Hyg.* **84**, 344–350 (2011).
1712 98. Fillatreau, S., Manfroi, B. & Dörner, T. Toll-like receptor signalling in B cells during
1713 systemic lupus erythematosus. *Nat. Rev. Rheumatol.* **17**, 98–108 (2021).

1714 99. Hua, Z. & Hou, B. TLR signaling in B-cell development and activation. *Cell. Mol.*
1715 *Immunol.* **10**, 103–106 (2013).
1716 100. Hartlehnert, M. *et al.* Bcl6 controls meningeal Th17–B cell interaction in murine
1717 neuroinflammation. *Proc. Natl. Acad. Sci.* **118**, e2023174118 (2021).
1718 101. Baxter, A. G. The origin and application of experimental autoimmune
1719 encephalomyelitis. *Nat. Rev. Immunol.* **7**, 904–912 (2007).
1720 102. Fletcher, J. M., Lalor, S. J., Sweeney, C. M., Tubridy, N. & Mills, K. H. G. T cells
1721 in multiple sclerosis and experimental autoimmune encephalomyelitis. *Clin. Exp.*
1722 *Immunol.* **162**, 1–11 (2010).
1723 103. Lopez, J. A., Denkova, M., Ramanathan, S., Dale, R. C. & Brilot, F.
1724 Pathogenesis of autoimmune demyelination: from multiple sclerosis to neuromyelitis
1725 optica spectrum disorders and myelin oligodendrocyte glycoprotein antibody-
1726 associated disease. *Clin. Transl. Immunol.* **10**, e1316 (2021).
1727 104. Lucchinetti, C. F. *et al.* Inflammatory Cortical Demyelination in Early Multiple
1728 Sclerosis. *N. Engl. J. Med.* **365**, 2188–2197 (2011).
1729 105. Cikes, N., Bosnic, D. & Sentic, M. Non-MS autoimmune demyelination. *Clin.*
1730 *Neurol. Neurosurg.* **110**, 905–912 (2008).
1731 106. Nguyen, H. T. T., Guevarra, R. B., Magez, S. & Radwanska, M. Single-cell
1732 transcriptome profiling and the use of AID deficient mice reveal that B cell activation
1733 combined with antibody class switch recombination and somatic hypermutation do
1734 not benefit the control of experimental trypanosomosis. *PLoS Pathog.* **17**, e1010026
1735 (2021).
1736 107. Friman, V. *et al.* Defective peripheral B cell selection in common variable
1737 immune deficiency patients with autoimmune manifestations. *Cell Rep.* **42**, (2023).

108. Magliozzi, R., Marastoni, D. & Calabrese, M. The BAFF / APRIL system as therapeutic target in multiple sclerosis. *Expert Opin. Ther. Targets* **24**, 1135–1145 (2020).

109. Lee, D. S. W., Rojas, O. L. & Gommerman, J. L. B cell depletion therapies in autoimmune disease: advances and mechanistic insights. *Nat. Rev. Drug Discov.* **20**, 179–199 (2021).

110. Florou, D., Katsara, M., Feehan, J., Dardiotis, E. & Apostolopoulos, V. Anti-CD20 Agents for Multiple Sclerosis: Spotlight on Ocrelizumab and Ofatumumab. *Brain Sci.* **10**, 758 (2020).

111. Blattner, M. S., de Bruin, G. S., Bucelli, R. C. & Day, G. S. Sleep disturbances are common in patients with autoimmune encephalitis. *J. Neurol.* **266**, 1007–1015 (2019).

112. Blattner, M. S. & Day, G. S. Sleep Disturbances in Patients with Autoimmune Encephalitis. *Curr. Neurol. Neurosci. Rep.* **20**, 28 (2020).

113. Yin, D., Chen, S. & Liu, J. Sleep Disturbances in Autoimmune Neurologic Diseases: Manifestation and Pathophysiology. *Front. Neurosci.* **15**, 687536 (2021).

114. Bonvalet, M., Ollila, H. M., Ambati, A. & Mignot, E. Autoimmunity in narcolepsy. *Curr. Opin. Pulm. Med.* **23**, 522–529 (2017).

115. Mignot, E. *et al.* Complex HLA-DR and -DQ Interactions Confer Risk of Narcolepsy-Cataplexy in Three Ethnic Groups. *Am. J. Hum. Genet.* **68**, 686–699 (2001).

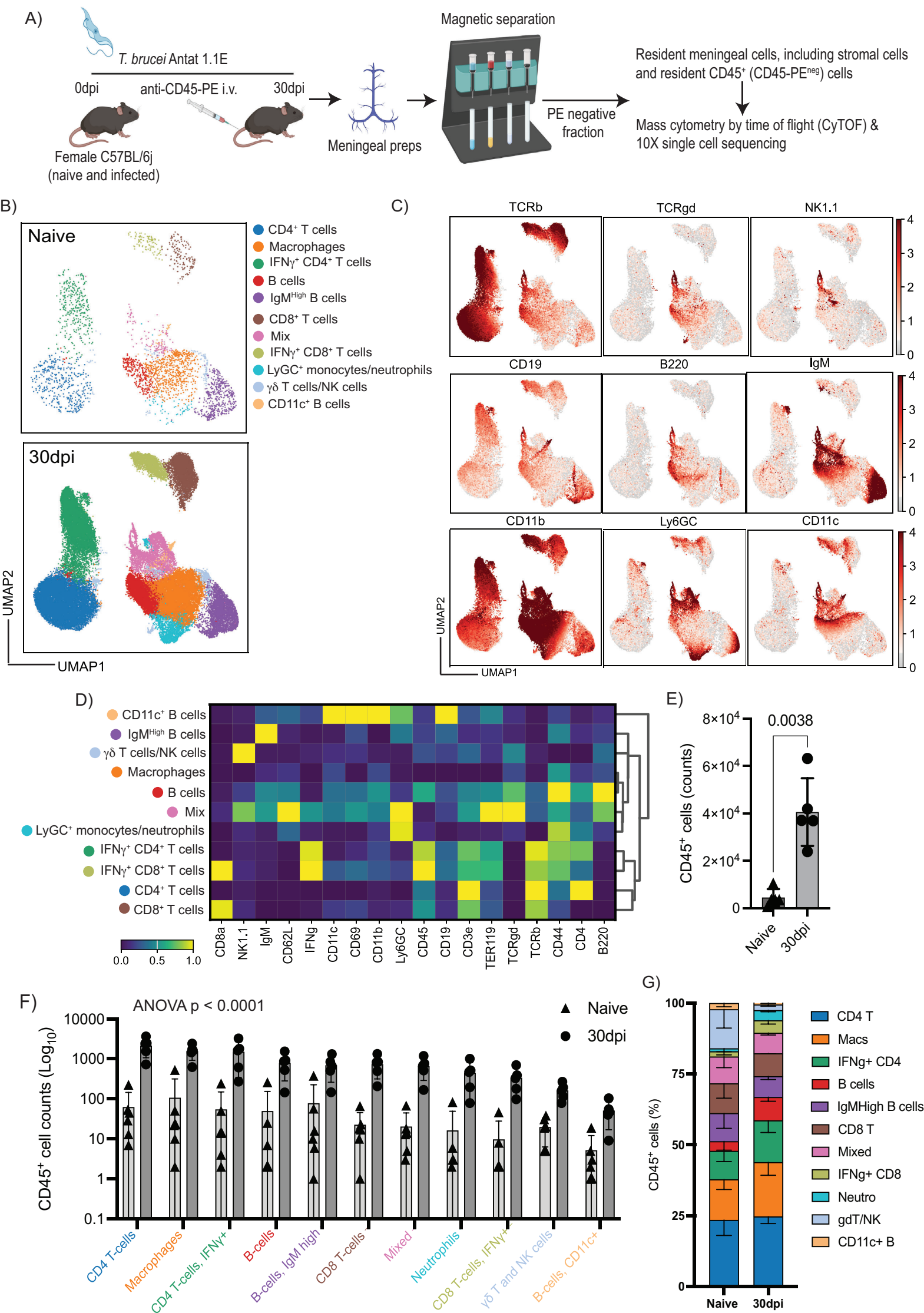
A)
T. brucei Antat 1.1E
0dpi
anti-CD45-PE i.v.
30dpi
Female C57BL/6j
(naive and infected)
Meningeal preps
Magnetic separation
PE negative fraction
Resident meningeal cells, including stromal cells and resident CD45+ (CD45-PEneg) cells
Mass cytometry by time of flight (CyTOF) & 10X single cell sequencing
B)
Naive
30dpi
UMAP2
UMAP1
CD4+ T cells
Macrophages
IFNγ+ CD4+ T cells
B cells
IgMHigh B cells
CD8+ T cells
Mix
IFNγ+ CD8+ T cells
LyGC+ monocytes/neutrophils
γδ T cells/NK cells
CD11c+ B cells
C)
TCRb
TCRgd
NK1.1
CD19
B220
IgM
CD11b
Ly6GC
CD11c
D)
CD11c+ B cells
IgMHigh B cells
γδ T cells/NK cells
Macrophages
B cells
Mix
LyGC+ monocytes/neutrophils
IFNγ+ CD4+ T cells
IFNγ+ CD8+ T cells
CD4+ T cells
CD8+ T cells
CD8a
NK1.1
IgM
CD62L
IFNg
CD11c
CD69
CD11b
Ly6GC
CD45
CD19
CD3e
TER119
TCRgd
TCRb
CD44
CD4
B220
E)
0.0038
CD45+ cells (counts)
Naive
30dpi
F)
ANOVA p < 0.0001
Naive
30dpi
CD45+ cell counts (Log10)
CD4 T-cells
Macrophages
CD4 T-cells, IFNγ+
B-cells
B-cells, IgM high
CD8 T-cells
Mixed
Neutrophils
CD8 T-cells, IFNγ+
γδ T and NK cells
B-cells, CD11c+
G)
CD45+ cells (%)
Naive
30dpi
CD4 T
Macs
IFNg+ CD4
B cells
IgMHigh B cells
CD8 T
Mixed
IFNg+ CD8
Neutro
gdT/NK
CD11c+ B

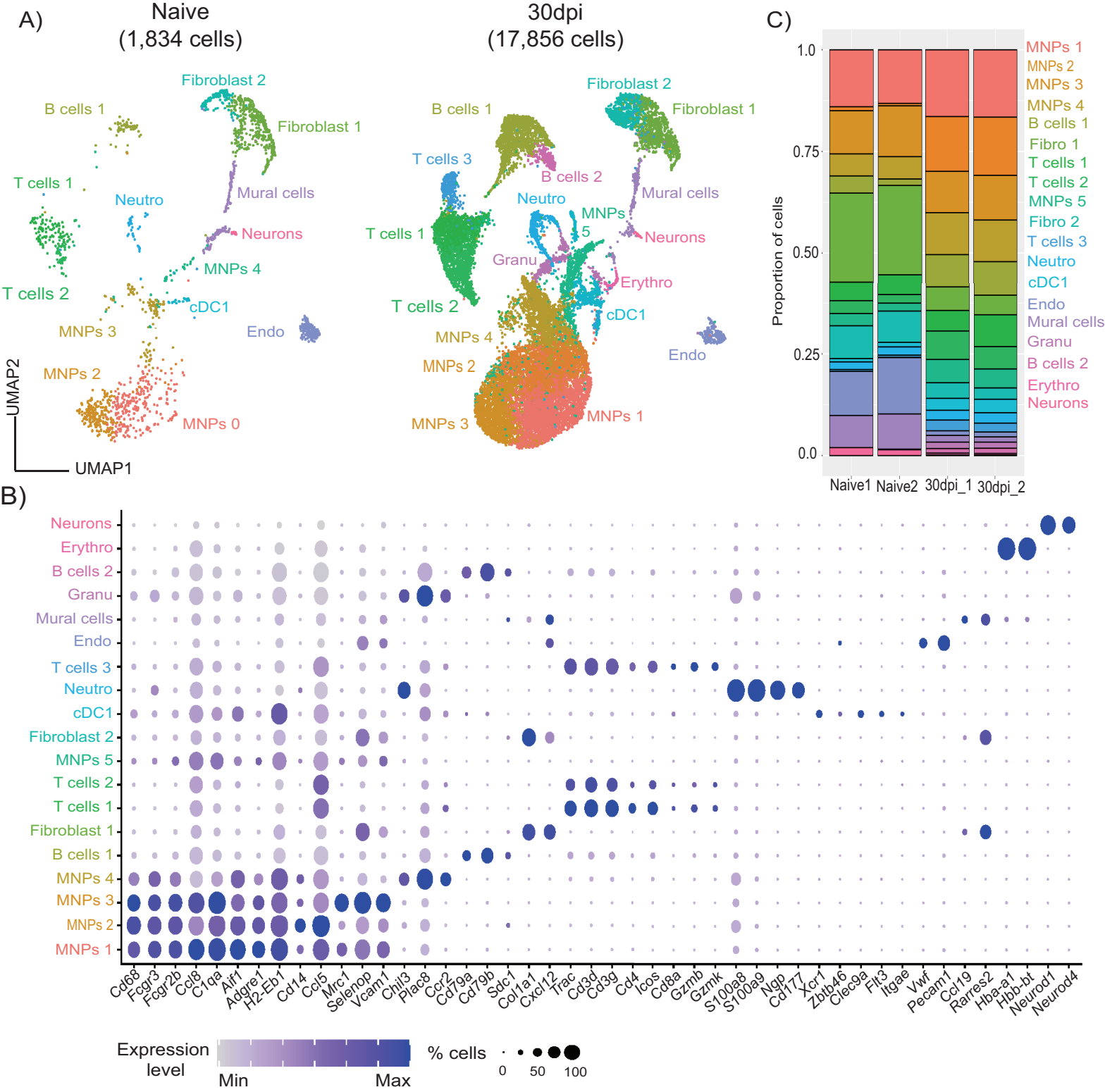
A)
Naive
(1,834 cells)
30dpi
(17,856 cells)
Fibroblast 2
B cells 1
Fibroblast 1
T cells 1
Neutro
Mural cells
Neurons
MNPs 4
T cells 2
cDC1
MNPs 3
Endo
MNPs 2
MNPs 0
UMAP2
UMAP1
T cells 3
B cells 2
MNPs 5
Granu
Erythro
MNPs 1
C)
Proportion of cells
1.0
0.75
0.50
0.25
0.0
Naive1
Naive2
30dpi_1
30dpi_2
MNPs 1
MNPs 2
MNPs 3
MNPs 4
B cells 1
Fibro 1
T cells 1
T cells 2
MNPs 5
Fibro 2
T cells 3
Neutro
cDC1
Endo
Mural cells
Granu
B cells 2
Erythro
Neurons
B)
Cd68
Fcgr3
Fcgr2b
Ccl8
C1qa
Aif1
Adgre1
H2-Eb1
Cd14
Ccl5
Mrc1
Selenop
Vcam1
Chil3
Plac8
Ccr2
Cd79a
Cd79b
Sdc1
Col1a1
Cxcl12
Trac
Cd3d
Cd3g
Cd4
Icos
Cd8a
Gzmb
Gzmk
S100a8
S100a9
Ngp
Cd177
Xcr1
Zbtb46
Clec9a
Flt3
Itgae
Vwf
Pecam1
Ccl19
Rarres2
Hba-a1
Hbb-bt
Neurod1
Neurod4
Expression level
Min
Max
% cells
0
50
100

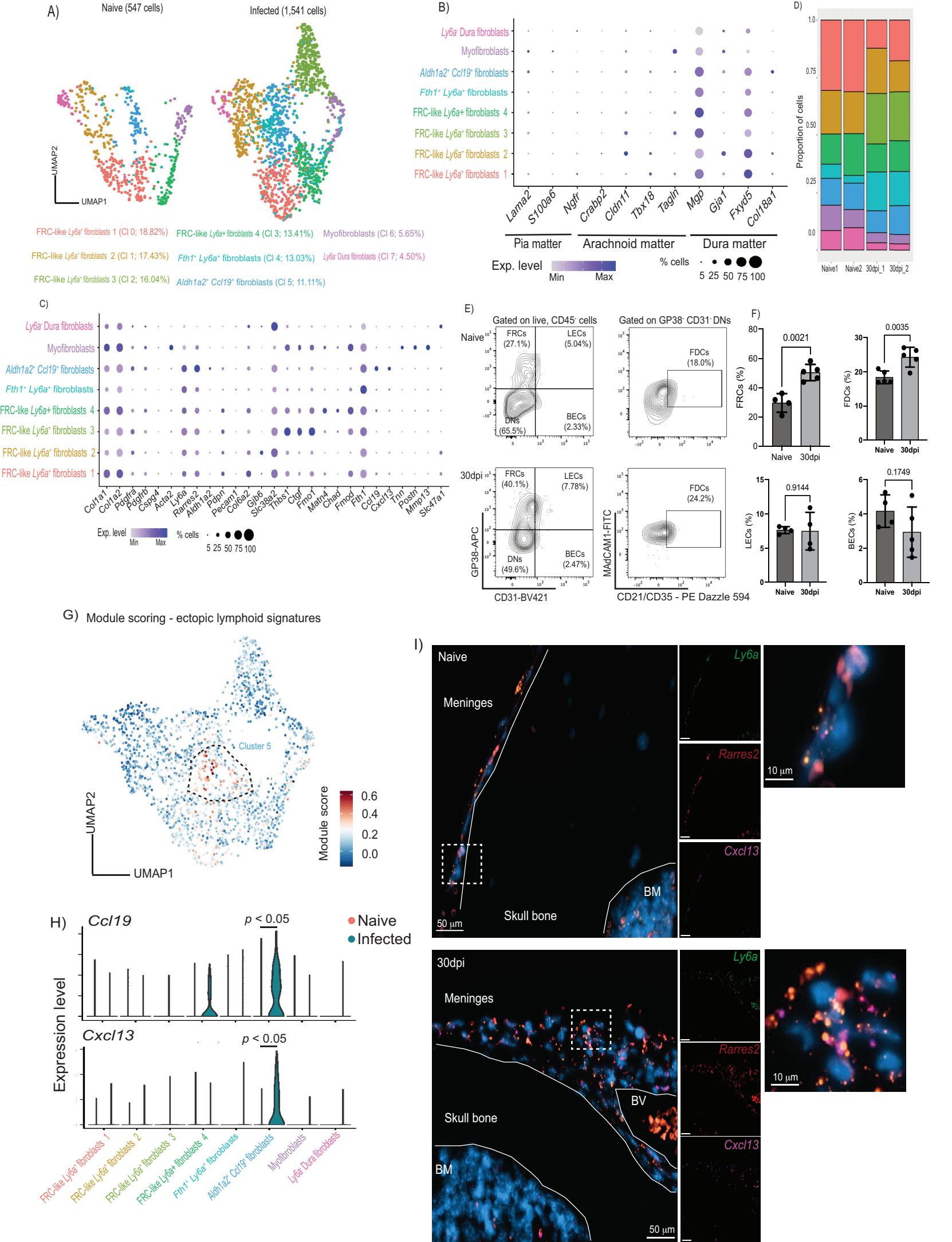
A)
Naive (547 cells)
Infected (1,541 cells)
UMAP2
UMAP1
FRC-like Ly6a+ fibroblasts 1 (Cl 0; 18.82%)
FRC-like Ly6a+ fibroblasts 2 (Cl 1; 17.43%)
FRC-like Ly6a+ fibroblasts 3 (Cl 2; 16.04%)
FRC-like Ly6a+ fibroblasts 4 (Cl 3; 13.41%)
Fth1+ Ly6a+ fibroblasts (Cl 4; 13.03%)
Aldh1a2+ Ccl19+ fibroblasts (Cl 5; 11.11%)
Myofibroblasts (Cl 6; 5.65%)
Ly6a- Dura fibroblasts (Cl 7; 4.50%)
B)
Ly6a- Dura fibroblasts
Myofibroblasts
Aldh1a2+ Ccl19+ fibroblasts
Fth1+ Ly6a+ fibroblasts
FRC-like Ly6a+ fibroblasts 4
FRC-like Ly6a+ fibroblasts 3
FRC-like Ly6a+ fibroblasts 2
FRC-like Ly6a+ fibroblasts 1
Lama2
S100a6
Ngfr
Crabp2
Cldn11
Tbx18
Tagln
Mgp
Gja1
Fxyd5
Col18a1
Pia matter
Arachnoid matter
Dura matter
Exp. level
Min
Max
% cells
5 25 50 75 100
D)
Proportion of cells
Naive1
Naive2
30dpi_1
30dpi_2
C)
Ly6a- Dura fibroblasts
Myofibroblasts
Aldh1a2+ Ccl19+ fibroblasts
Fth1+ Ly6a+ fibroblasts
FRC-like Ly6a+ fibroblasts 4
FRC-like Ly6a+ fibroblasts 3
FRC-like Ly6a+ fibroblasts 2
FRC-like Ly6a+ fibroblasts 1
Col1a1
Col1a2
Pdgfra
Pdgfrb
Cspg4
Acta2
Ly6a
Rarres2
Aldh1a2
Pdpn
Pecam1
Col6a2
Glb6
Slc38a2
Thbs1
Ctgf
Fmo1
Matn4
Chad
Fmod
Fth1
Ccl19
Cxcl13
Tnn
Postn
Mmp13
Slc47a1
Exp. level
Min
Max
% cells
5 25 50 75 100
E)
Gated on live, CD45- cells
Gated on GP38- CD31- DNs
Naive
FRCs (27.1%)
LECs (5.04%)
DNs (65.5%)
BECs (2.33%)
FDCs (18.0%)
30dpi
FRCs (40.1%)
LECs (7.78%)
DNs (49.6%)
BECs (2.47%)
FDCs (24.2%)
GP38-APC
CD31-BV421
MAdCAM1-FITC
CD21/CD35 - PE Dazzle 594
F)
FRCs (%)
0.0021
FDCs (%)
0.0035
LECs (%)
0.9144
BECs (%)
0.1749
Naive
30dpi
G) Module scoring - ectopic lymphoid signatures
Cluster 5
UMAP2
UMAP1
Module score
0.6
0.4
0.2
0.0
H)
Ccl19
p < 0.05
Naive
Infected
Cxcl13
p < 0.05
Expression level
FRC-like Ly6a+ fibroblasts 1
FRC-like Ly6a+ fibroblasts 2
FRC-like Ly6a+ fibroblasts 3
FRC-like Ly6a+ fibroblasts 4
Fth1+ Ly6a+ fibroblasts
Aldh1a2+ Ccl19+ fibroblasts
Myofibroblasts
Ly6a- Dura fibroblasts
I)
Naive
Meninges
Skull bone
BM
50 µm
Ly6a
Rarres2
Cxcl13
10 µm
30dpi
Meninges
Skull bone
BV
BM
50 µm
Ly6a
Rarres2
Cxcl13
10 µm

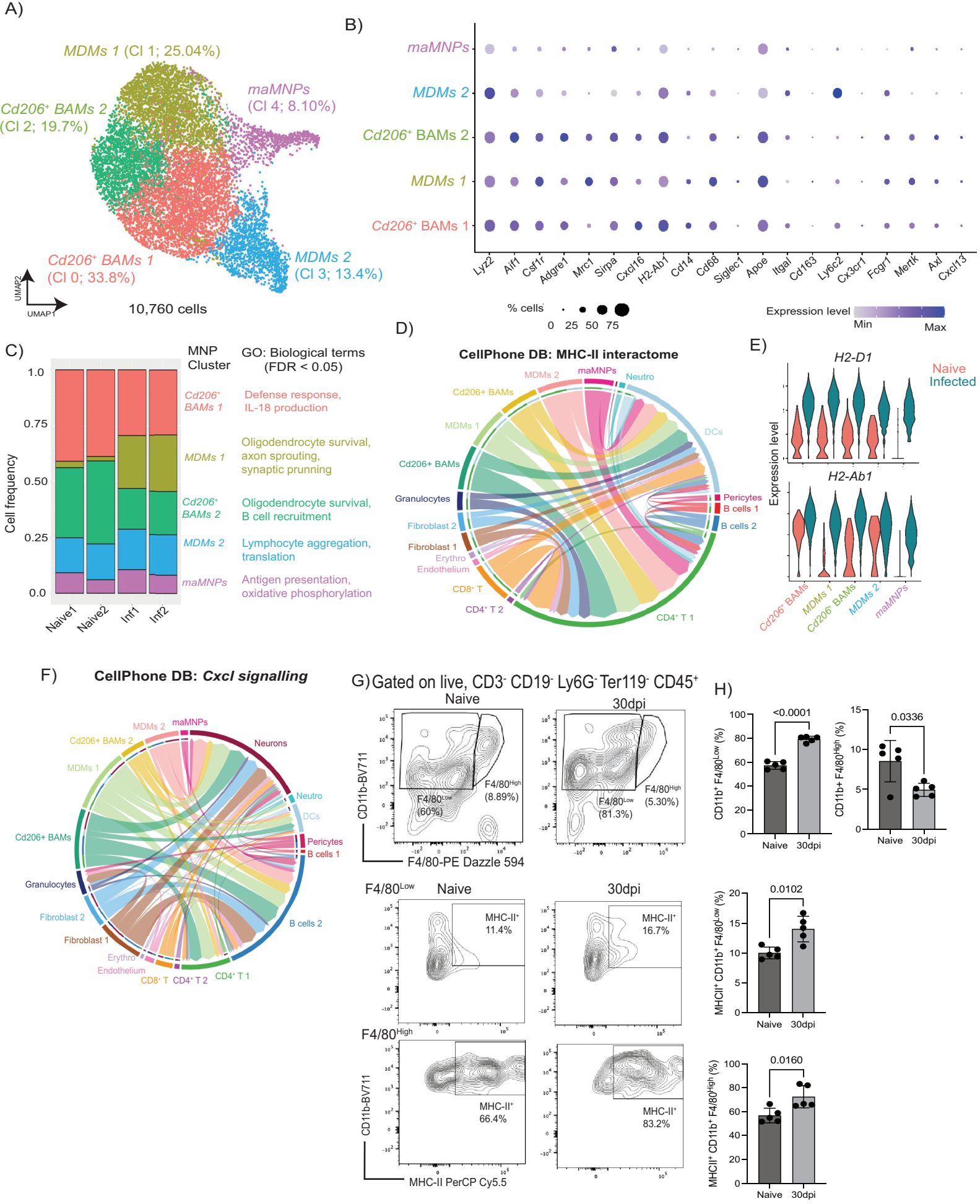
A)
MDMs 1 (Cl 1; 25.04%)
maMNPs (Cl 4; 8.10%)
Cd206+ BAMs 2 (Cl 2; 19.7%)
Cd206+ BAMs 1 (Cl 0; 33.8%)
MDMs 2 (Cl 3; 13.4%)
UMAP2
UMAP1
10,760 cells
B)
maMNPs
MDMs 2
Cd206+ BAMs 2
MDMs 1
Cd206+ BAMs 1
Lyz2 Aif1 Csf1r Adgre1 Mrc1 Sirpa Cxcl16 H2-Ab1 Cd14 Cd68 Siglec1 Apoe Itgal Cd163 Ly6c2 Cx3cr1 Fcgr1 Mertk Axl Cxcl13
% cells
0 25 50 75
Expression level
Min
Max
C)
MNP Cluster
GO: Biological terms (FDR < 0.05)
Cell frequency
1.0
0.75
0.50
0.25
0.0
Naive1 Naive2 Inf1 Inf2
Cd206+ BAMs 1
Defense response, IL-18 production
MDMs 1
Oligodendrocyte survival, axon sprouting, synaptic prunning
Cd206+ BAMs 2
Oligodendrocyte survival, B cell recruitment
MDMs 2
Lymphocyte aggregation, translation
maMNPs
Antigen presentation, oxidative phosphorylation
D)
CellPhone DB: MHC-II interactome
MDMs 2
maMNPs
Neutro
Cd206+ BAMs
MDMs 1
DCs
Cd206+ BAMs
Granulocytes
Pericytes
B cells 1
B cells 2
Fibroblast 2
Fibroblast 1
Erythro
Endothelium
CD8+ T
CD4+ T 2
CD4+ T 1
E)
H2-D1
H2-Ab1
Naive
Infected
Expression level
Cd206+ BAMs
MDMs 1
Cd206- BAMs
MDMs 2
maMNPs
F)
CellPhone DB: Cxcl signalling
MDMs 2
maMNPs
Cd206+ BAMs 2
Neurons
MDMs 1
Neutro
DCs
Cd206+ BAMs
Pericytes
B cells 1
Granulocytes
Fibroblast 2
B cells 2
Fibroblast 1
Erythro
Endothelium
CD8+ T
CD4+ T 2
CD4+ T 1
G) Gated on live, CD3- CD19- Ly6G- Ter119- CD45+
Naive
30dpi
CD11b-BV711
F4/80-PE Dazzle 594
F4/80High (8.89%)
F4/80Low (60%)
F4/80High (5.30%)
F4/80Low (81.3%)
F4/80Low
F4/80High
MHC-II+ 11.4%
MHC-II+ 16.7%
MHC-II+ 66.4%
MHC-II+ 83.2%
MHC-II PerCP Cy5.5
H)
<0.0001
0.0336
0.0102
0.0160
CD11b+ F4/80Low (%)
CD11b+ F4/80High (%)
MHCII+ CD11b+ F4/80Low (%)
MHCII+ CD11b+ F4/80High (%)
Naive
30dpi

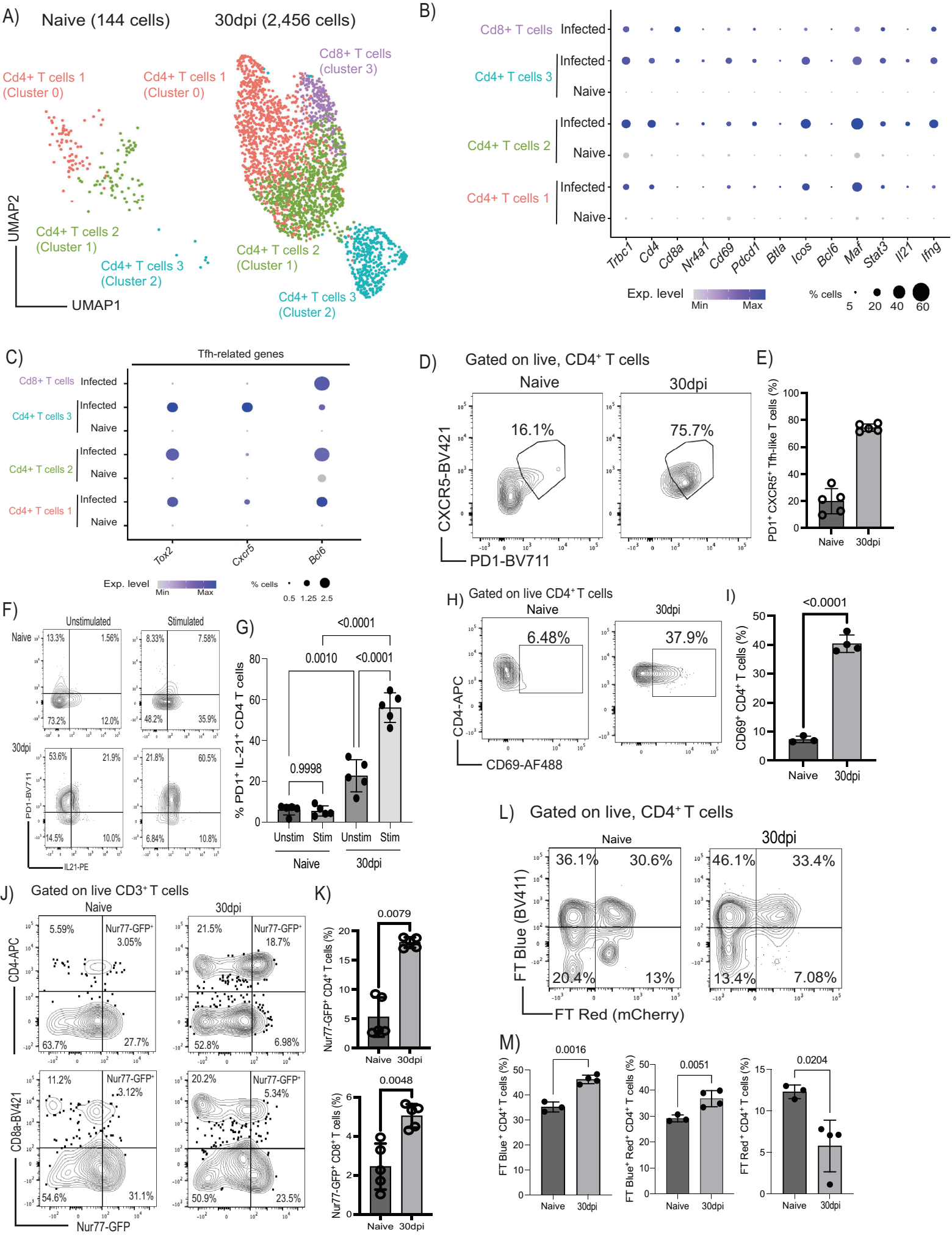
A)
Naive (144 cells)
30dpi (2,456 cells)
Cd4+ T cells 1 (Cluster 0)
Cd4+ T cells 1 (Cluster 0)
Cd8+ T cells (cluster 3)
Cd4+ T cells 2 (Cluster 1)
Cd4+ T cells 3 (Cluster 2)
Cd4+ T cells 2 (Cluster 1)
Cd4+ T cells 3 (Cluster 2)
UMAP2
UMAP1
B)
Cd8+ T cells Infected
Cd4+ T cells 3 Infected Naive
Cd4+ T cells 2 Infected Naive
Cd4+ T cells 1 Infected Naive
Tribc1 Cd4 Cd8a Nr4a1 Cd69 Pdcd1 Btla Icos Bcl6 Maf Stat3 Il21 Ifng
Exp. level Min Max
% cells 5 20 40 60
C)
Tfh-related genes
Cd8+ T cells Infected
Cd4+ T cells 3 Infected Naive
Cd4+ T cells 2 Infected Naive
Cd4+ T cells 1 Infected Naive
Tox2 Cxcr5 Bcl6
Exp. level Min Max
% cells 0.5 1.25 2.5
D)
Gated on live, CD4+ T cells
Naive
30dpi
16.1%
75.7%
CXCR5-BV421
PD1-BV711
E)
PD1+ CXCR5+ Tfh-like T cells (%)
Naive 30dpi
F)
Unstimulated
Stimulated
Naive
30dpi
13.3% 1.56% 73.2% 12.0%
8.33% 7.58% 48.2% 35.9%
53.6% 21.9% 14.5% 10.0%
21.8% 60.5% 6.84% 10.8%
PD1-BV711
IL21-PE
G)
% PD1+ IL-21+ CD4 T cells
<0.0001
0.0010
<0.0001
0.9998
Unstim Stim Unstim Stim
Naive 30dpi
H)
Gated on live CD4+ T cells
Naive
30dpi
6.48%
37.9%
CD4-APC
CD69-AF488
I)
<0.0001
CD69+ CD4+ T cells (%)
Naive 30dpi
J)
Gated on live CD3+ T cells
Naive
30dpi
5.59% Nur77-GFP+ 3.05% 63.7% 27.7%
21.5% Nur77-GFP+ 18.7% 52.8% 6.98%
11.2% Nur77-GFP+ 3.12% 54.6% 31.1%
20.2% Nur77-GFP+ 5.34% 50.9% 23.5%
CD4-APC
CD8a-BV421
Nur77-GFP
K)
0.0079
Nur77-GFP+ CD4+ T cells (%)
Naive 30dpi
0.0048
Nur77-GFP+ CD8+ T cells (%)
Naive 30dpi
L)
Gated on live, CD4+ T cells
Naive
30dpi
36.1% 30.6% 20.4% 13%
46.1% 33.4% 13.4% 7.08%
FT Blue (BV411)
FT Red (mCherry)
M)
0.0016
FT Blue+ CD4+ T cells (%)
Naive 30dpi
0.0051
FT Blue+ Red+ CD4+ T cells (%)
Naive 30dpi
0.0204
FT Red+ CD4+ T cells (%)
Naive 30dpi

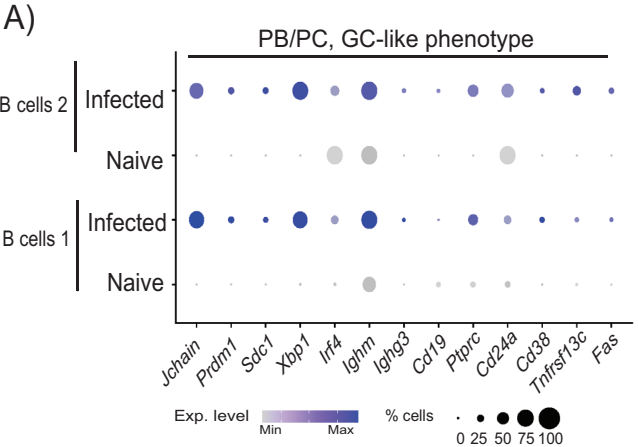
A)
PB/PC, GC-like phenotype
B cells 2
Infected
Naive
B cells 1
Infected
Naive
Jchain
Prdm1
Sdc1
Xbp1
Irf4
Ighm
Ighg3
Cd19
Ptprc
Cd24a
Cd38
Tnfrsf13c
Fas
Exp. level
Min
Max
% cells
0 25 50 75 100

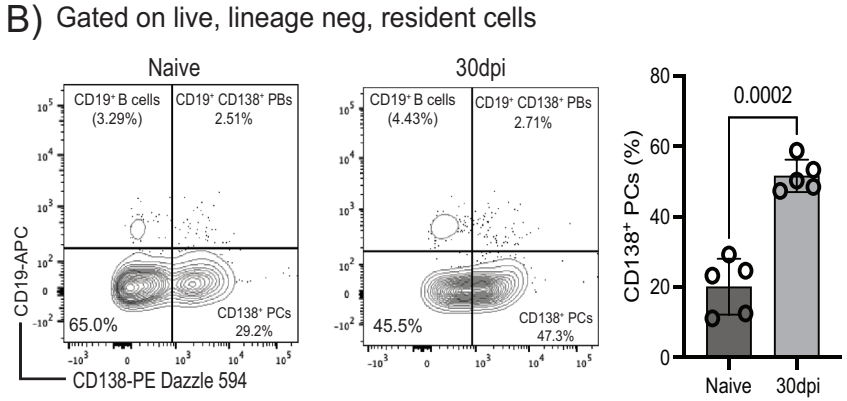
B) Gated on live, lineage neg, resident cells
Naive
30dpi
CD19+ B cells (3.29%)
CD19+ CD138+ PBs 2.51%
65.0%
CD138+ PCs 29.2%
CD19+ B cells (4.43%)
CD19+ CD138+ PBs 2.71%
45.5%
CD138+ PCs 47.3%
CD19-APC
CD138-PE Dazzle 594
0.0002
CD138+ PCs (%)
Naive
30dpi

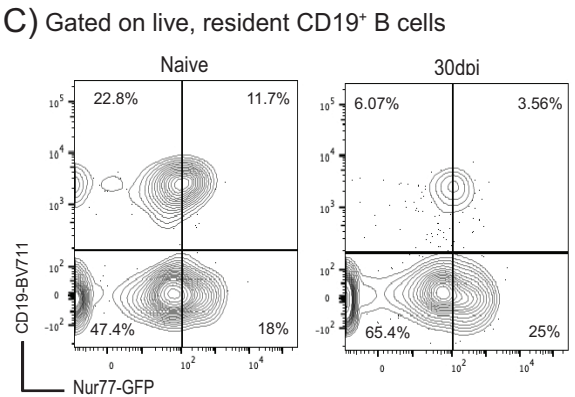
C) Gated on live, resident CD19+ B cells
Naive
30dpi
22.8%
11.7%
47.4%
18%
6.07%
3.56%
65.4%
25%
CD19-BV711
Nur77-GFP

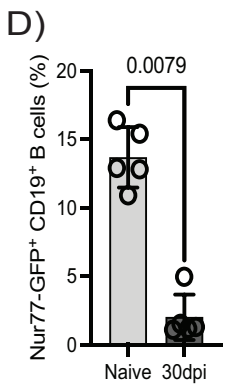
D)
0.0079
Nur77-GFP+ CD19+ B cells (%)
Naive
30dpi

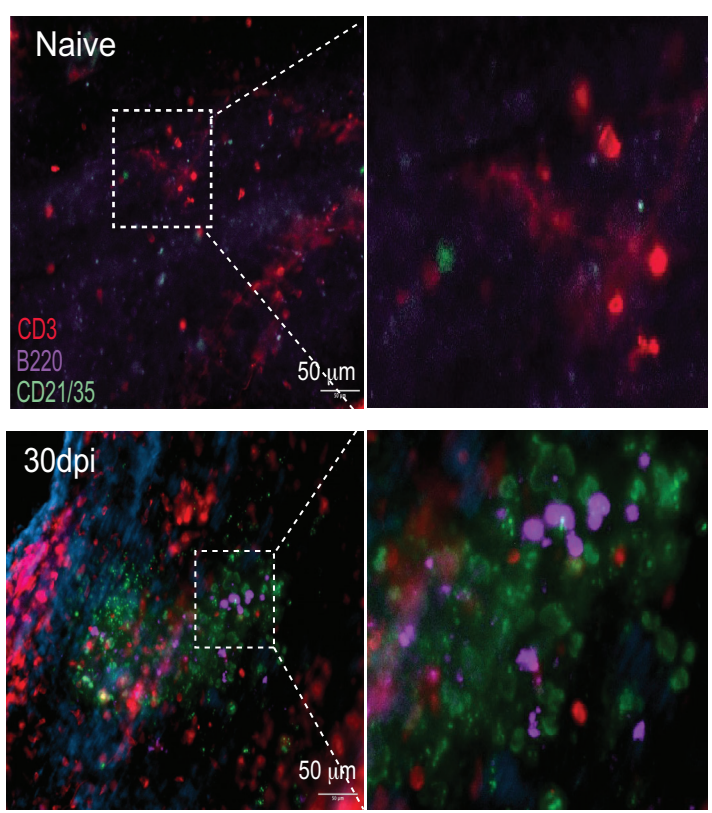
I)
Naive
CD3
B220
CD21/35
50 µm
30dpi
50 µm

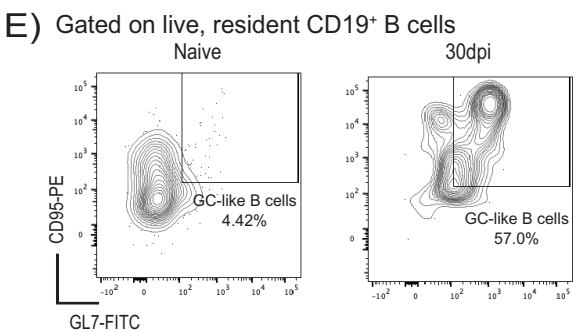
E) Gated on live, resident CD19+ B cells
Naive
30dpi
GC-like B cells 4.42%
GC-like B cells 57.0%
CD95-PE
GL7-FITC

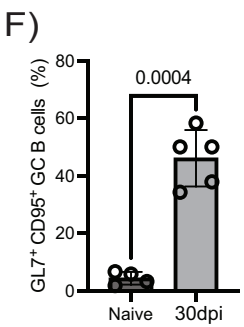
F)
0.0004
GL7+ CD95+ GC B cells (%)
Naive
30dpi

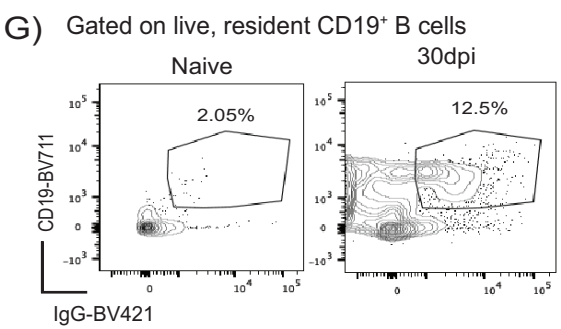
G) Gated on live, resident CD19+ B cells
Naive
30dpi
2.05%
12.5%
CD19-BV711
IgG-BV421

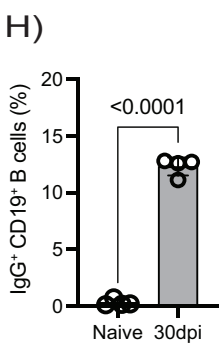
H)
<0.0001
IgG+ CD19+ B cells (%)
Naive
30dpi

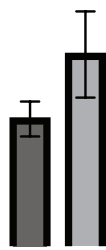

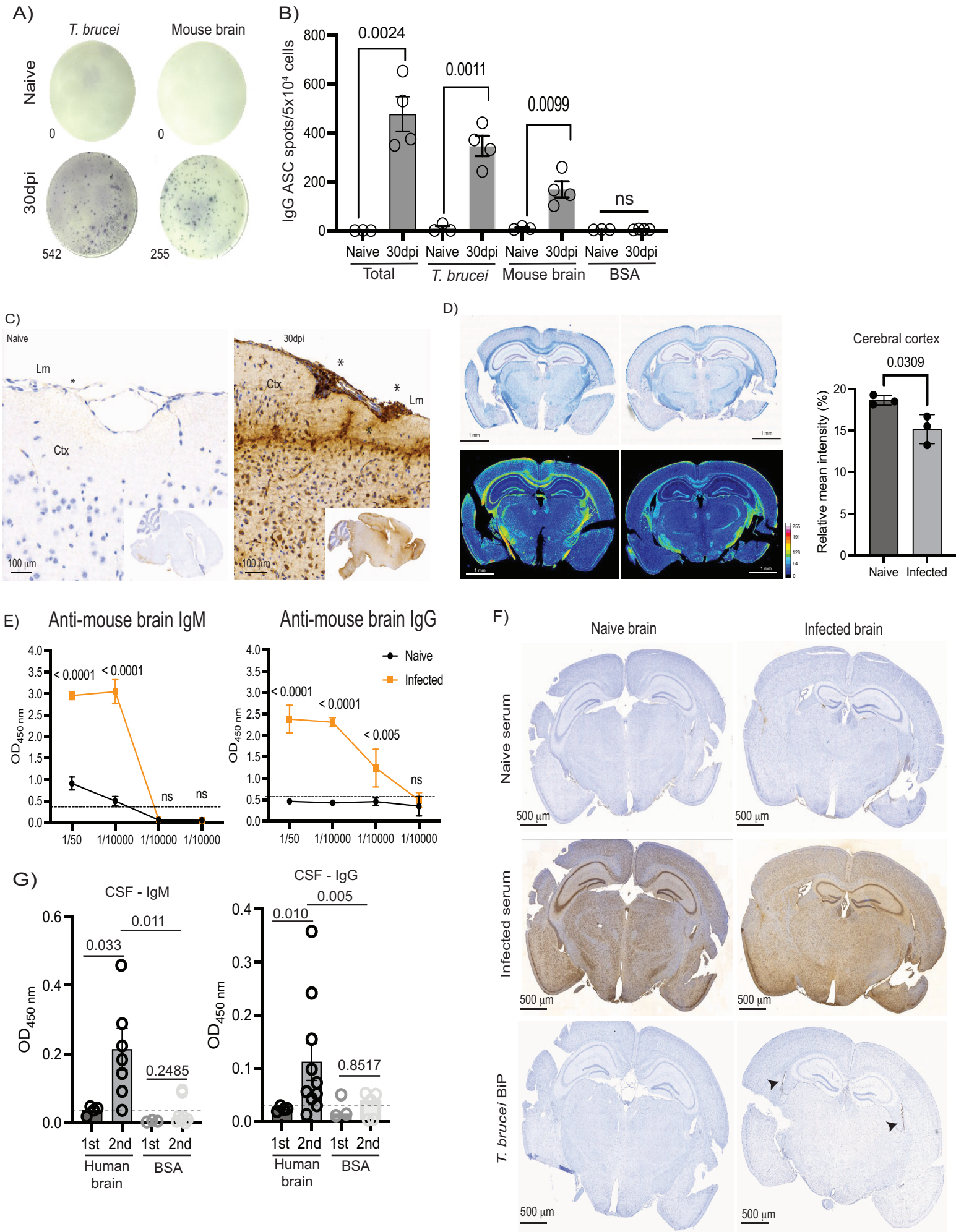
A)
T. brucei
Mouse brain
Naive
30dpi
0
0
542
255
B)
IgG ASC spots/5x10⁴ cells
0.0024
0.0011
0.0099
ns
Naive 30dpi Naive 30dpi Naive 30dpi Naive 30dpi
Total
T. brucei
Mouse brain
BSA
C)
Naive
Lm
Ctx
100 µm
30dpi
Ctx
Lm
100 µm
D)
Cerebral cortex
0.0309
Relative mean intensity (%)
Naive
Infected
E)
Anti-mouse brain IgM
Anti-mouse brain IgG
OD450 nm
< 0.0001
< 0.0001
ns
ns
< 0.0001
< 0.0001
< 0.005
ns
Naive
Infected
1/50
1/10000
1/10000
1/10000
F)
Naive brain
Infected brain
Naive serum
Infected serum
T. brucei BiP
500 µm
G)
CSF - IgM
CSF - IgG
OD450 nm
0.033
0.011
0.2485
0.010
0.005
0.8517
1st 2nd 1st 2nd
Human brain
BSA

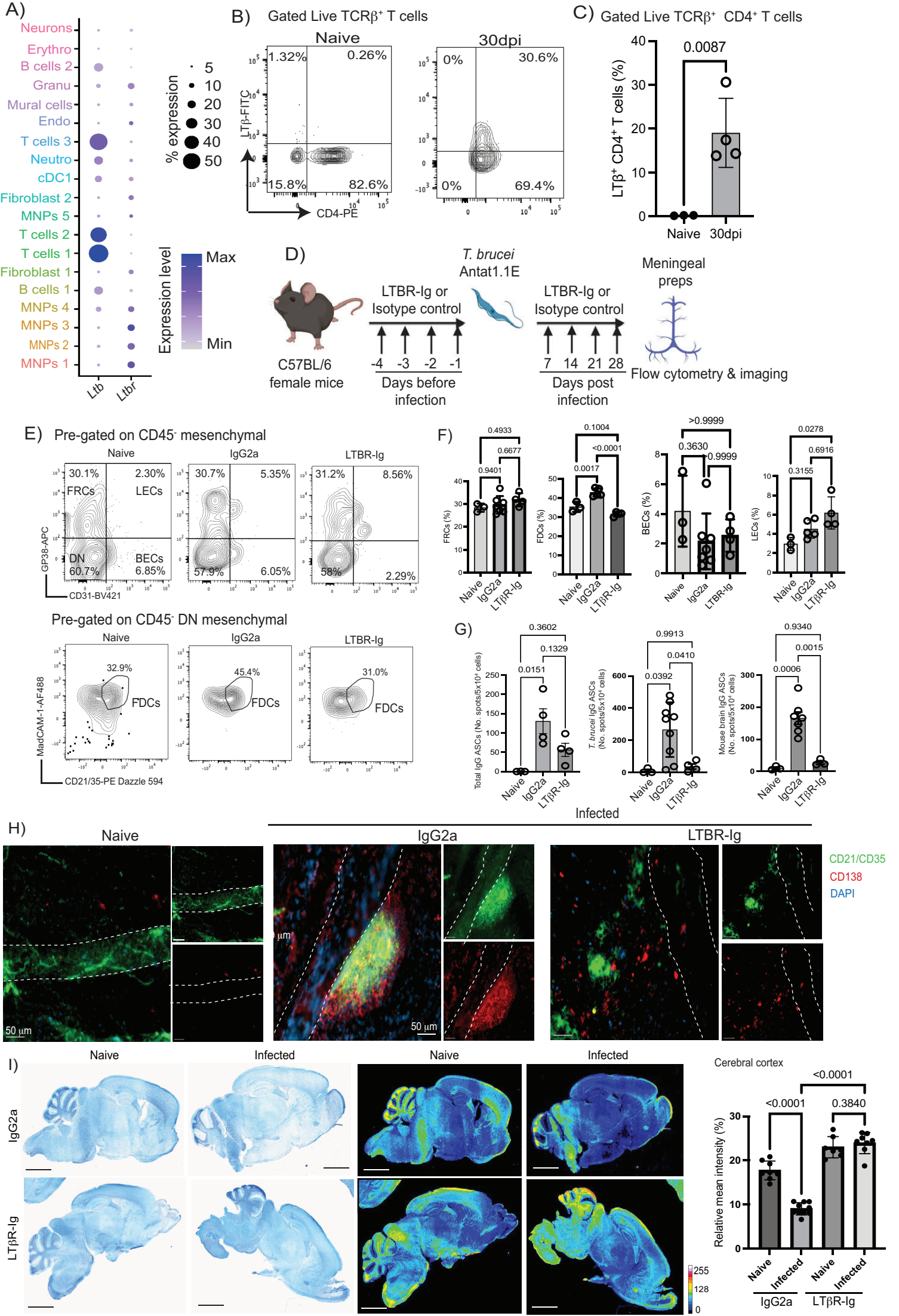
A)
Neurons
Erythro
B cells 2
Granu
Mural cells
Endo
T cells 3
Neutro
cDC1
Fibroblast 2
MNPs 5
T cells 2
T cells 1
Fibroblast 1
B cells 1
MNPs 4
MNPs 3
MNPs 2
MNPs 1
Ltb
Ltbr
% expression
5
10
20
30
40
50
Expression level
Max
Min
B) Gated Live TCRβ+ T cells
Naive
30dpi
1.32%
0.26%
15.8%
82.6%
0%
30.6%
0%
69.4%
LTβ-FITC
CD4-PE
C) Gated Live TCRβ+ CD4+ T cells
LTβ+ CD4+ T cells (%)
0.0087
Naive
30dpi
D)
C57BL/6
female mice
LTBR-Ig or
Isotype control
-4 -3 -2 -1
Days before
infection
T. brucei
Antat1.1E
LTBR-Ig or
Isotype control
7 14 21 28
Days post
infection
Meningeal
preps
Flow cytometry & imaging
E) Pre-gated on CD45- mesenchymal
Naive
IgG2a
LTBR-Ig
30.1%
2.30%
FRCs
LECs
DN
60.7%
BECs
6.85%
30.7%
5.35%
57.9%
6.05%
31.2%
8.56%
58%
2.29%
GP38-APC
CD31-BV421
Pre-gated on CD45- DN mesenchymal
32.9%
45.4%
31.0%
FDCs
MadCAM-1-AF488
CD21/35-PE Dazzle 594
F)
FRCs (%)
FDCs (%)
BECs (%)
LECs (%)
0.4933
0.6677
0.9401
0.1004
<0.0001
0.0017
>0.9999
0.3630
0.9999
0.0278
0.6916
0.3155
Naive
IgG2a
LTβR-Ig
G)
Total IgG ASCs (No. spots/5x10⁴ cells)
T. brucei IgG ASCs (No. spots/5x10⁴ cells)
Mouse brain IgG ASCs (No. spots/5x10⁴ cells)
0.3602
0.1329
0.0151
0.9913
0.0410
0.0392
0.9340
0.0015
0.0006
Infected
H)
Naive
IgG2a
LTBR-Ig
CD21/CD35
CD138
DAPI
50 µm
I)
Naive
Infected
IgG2a
LTβR-Ig
Cerebral cortex
Relative mean intensity (%)
<0.0001
<0.0001
0.3840
255
128
0

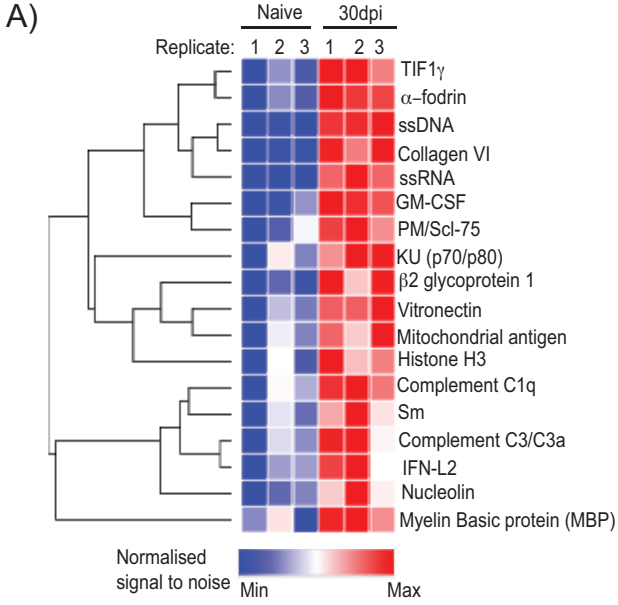

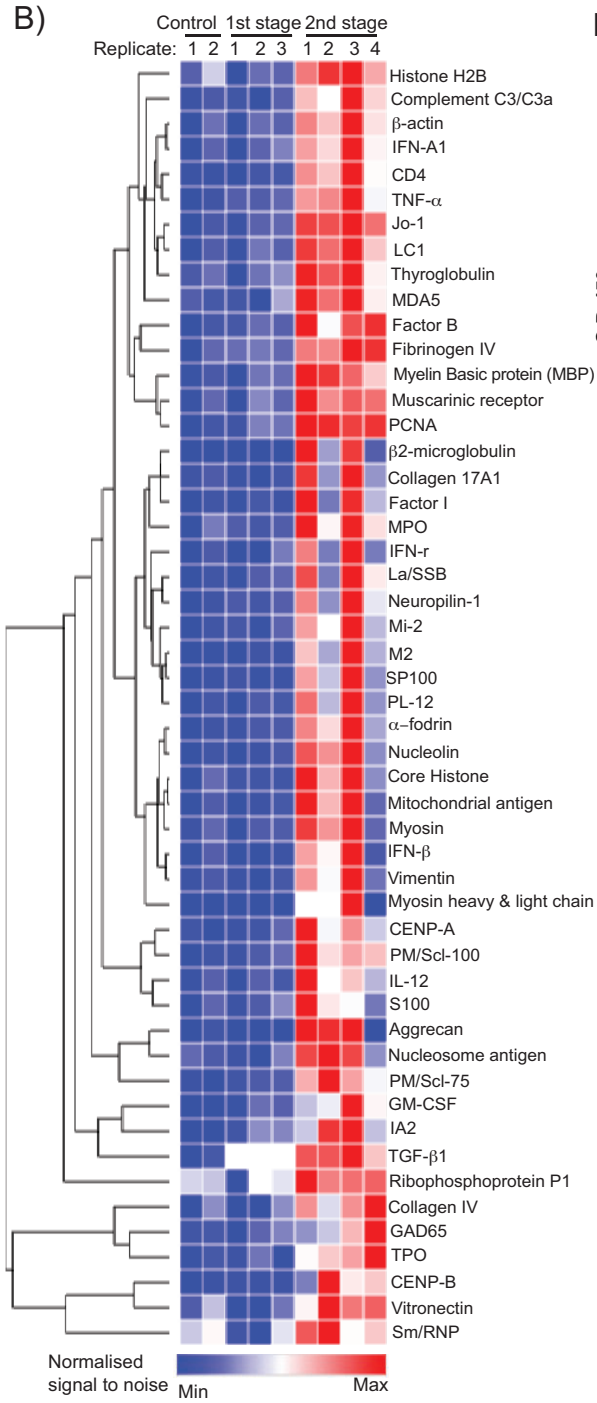

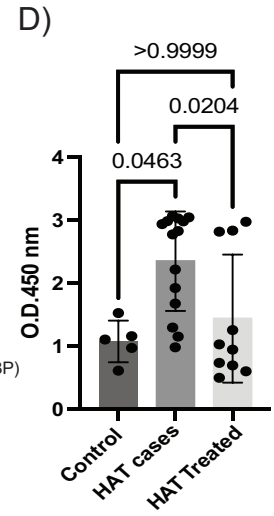

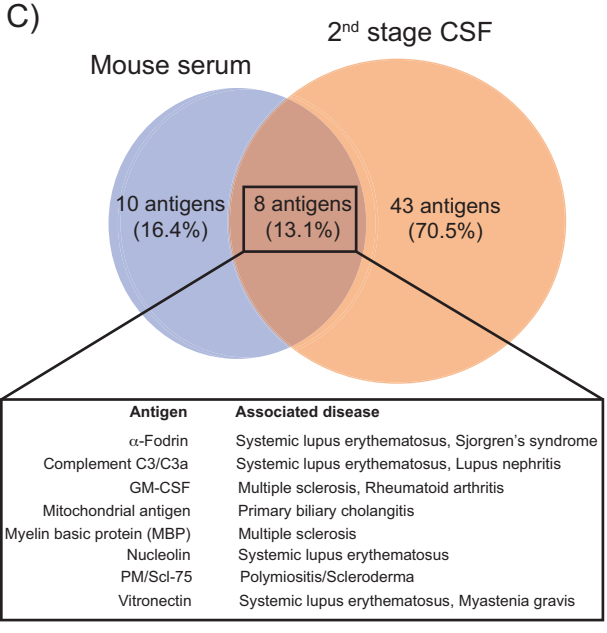

Antigen	Associated disease
α-Fodrin	Systemic lupus erythematosus, Sjorgren's syndrome
Complement C3/C3a	Systemic lupus erythematosus, Lupus nephritis
GM-CSF	Multiple sclerosis, Rheumatoid arthritis
Mitochondrial antigen	Primary biliary cholangitis
Myelin basic protein (MBP)	Multiple sclerosis
Nucleolin	Systemic lupus erythematosus
PM/Scl-75	Polymiositis/Scleroderma
Vitronectin	Systemic lupus erythematosus, Myastenia gravis

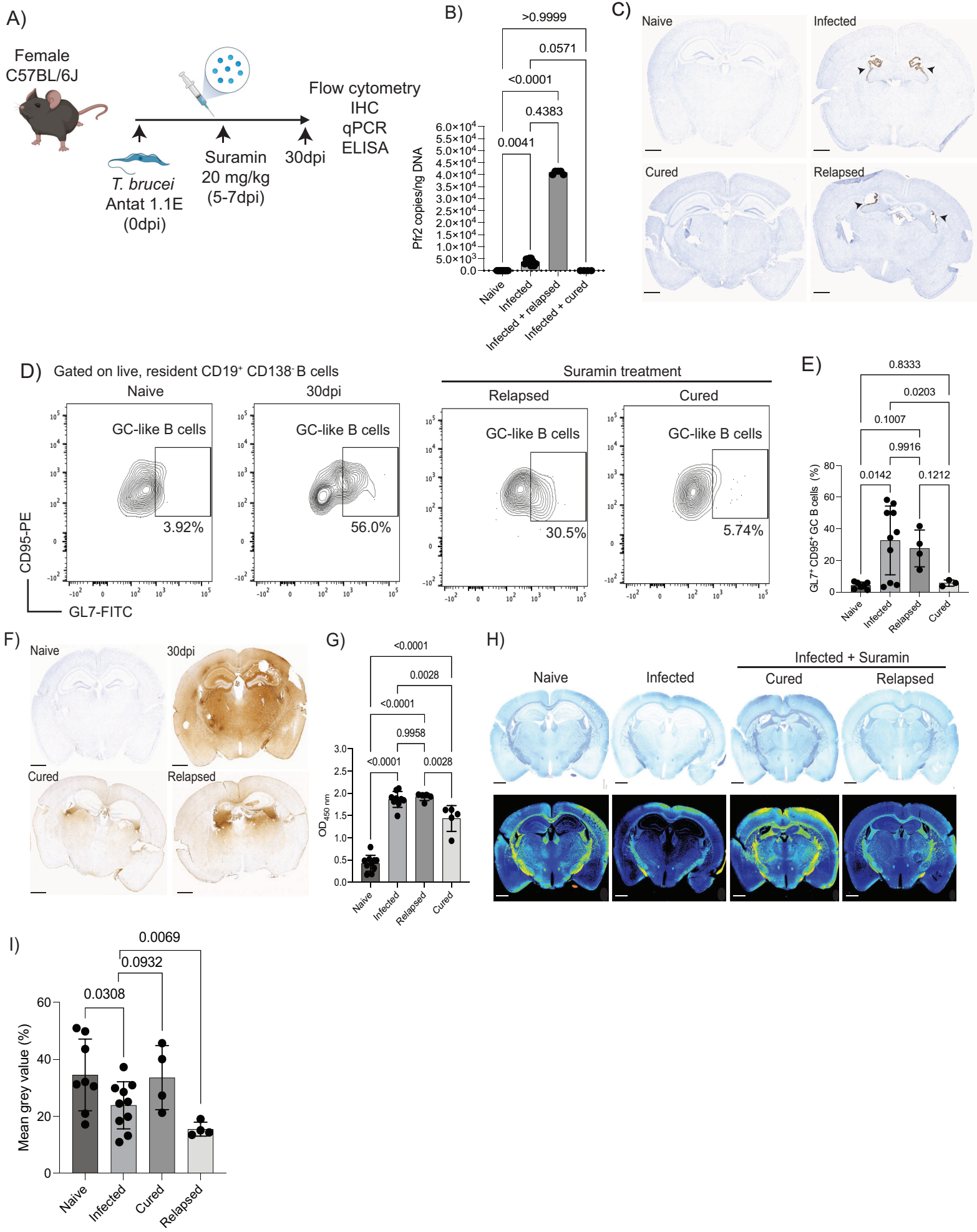
A)
Female
C57BL/6J
T. brucei
Antat 1.1E
(0dpi)
Suramin
20 mg/kg
(5-7dpi)
30dpi
Flow cytometry
IHC
qPCR
ELISA
B)
Pfr2 copies/ng DNA
>0.9999
0.0571
<0.0001
0.4383
0.0041
Naive
Infected
Infected + relapsed
Infected + cured
C)
Naive
Infected
Cured
Relapsed
D)
Gated on live, resident CD19+ CD138- B cells
Naive
30dpi
Suramin treatment
Relapsed
Cured
GC-like B cells
3.92%
56.0%
30.5%
5.74%
CD95-PE
GL7-FITC
E)
GL7+ CD95+ GC B cells (%)
0.8333
0.0203
0.1007
0.9916
0.0142
0.1212
Naive
Infected
Relapsed
Cured
F)
Naive
30dpi
Cured
Relapsed
G)
OD450 nm
<0.0001
0.0028
<0.0001
0.9958
<0.0001
0.0028
Naive
Infected
Relapsed
Cured
H)
Naive
Infected
Infected + Suramin
Cured
Relapsed
I)
Mean grey value (%)
0.0069
0.0932
0.0308
Naive
Infected
Cured
Relapsed

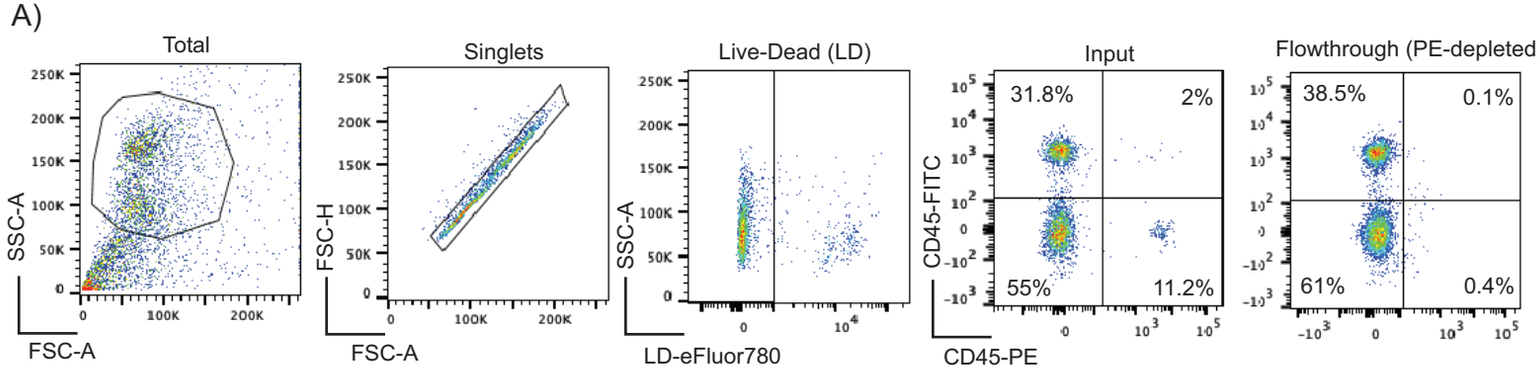
A)
Total
Singlets
Live-Dead (LD)
Input
Flowthrough (PE-depleted)
SSC-A
FSC-A
FSC-H
LD-eFluor780
CD45-FITC
CD45-PE
31.8%
2%
55%
11.2%
38.5%
0.1%
61%
0.4%

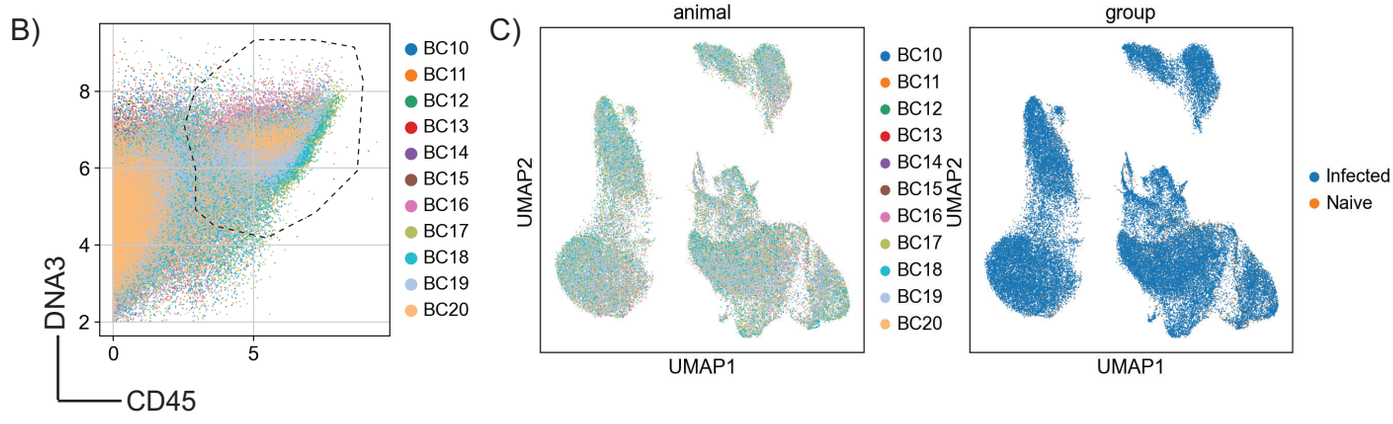
B)
DNA3
CD45
BC10
BC11
BC12
BC13
BC14
BC15
BC16
BC17
BC18
BC19
BC20
C)
animal
group
UMAP1
UMAP2
Infected
Naive

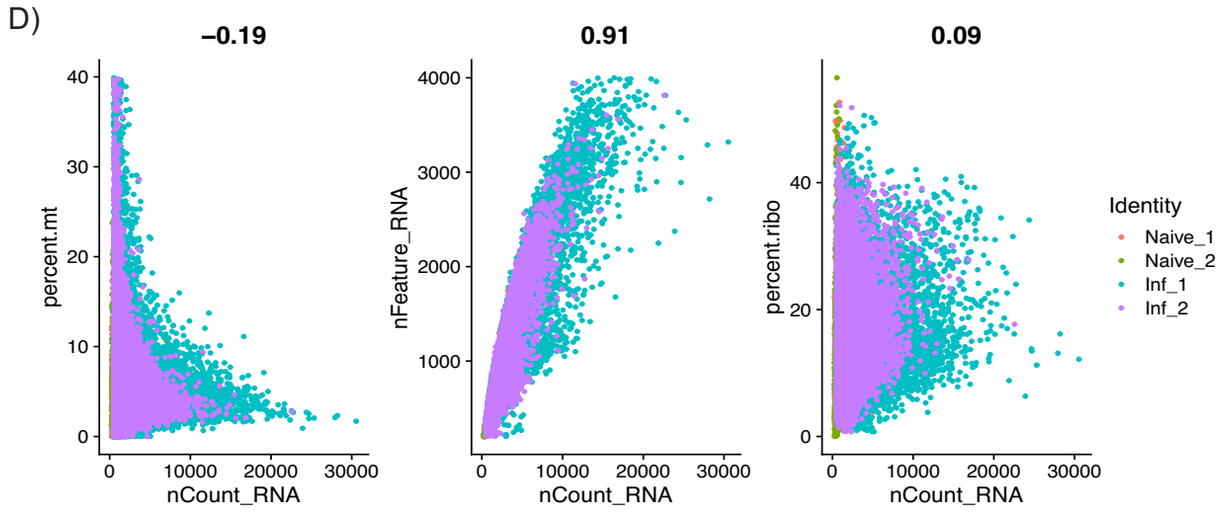
D)
−0.19
0.91
0.09
percent.mt
nFeature_RNA
percent.ribo
nCount_RNA
Identity
Naive_1
Naive_2
Inf_1
Inf_2

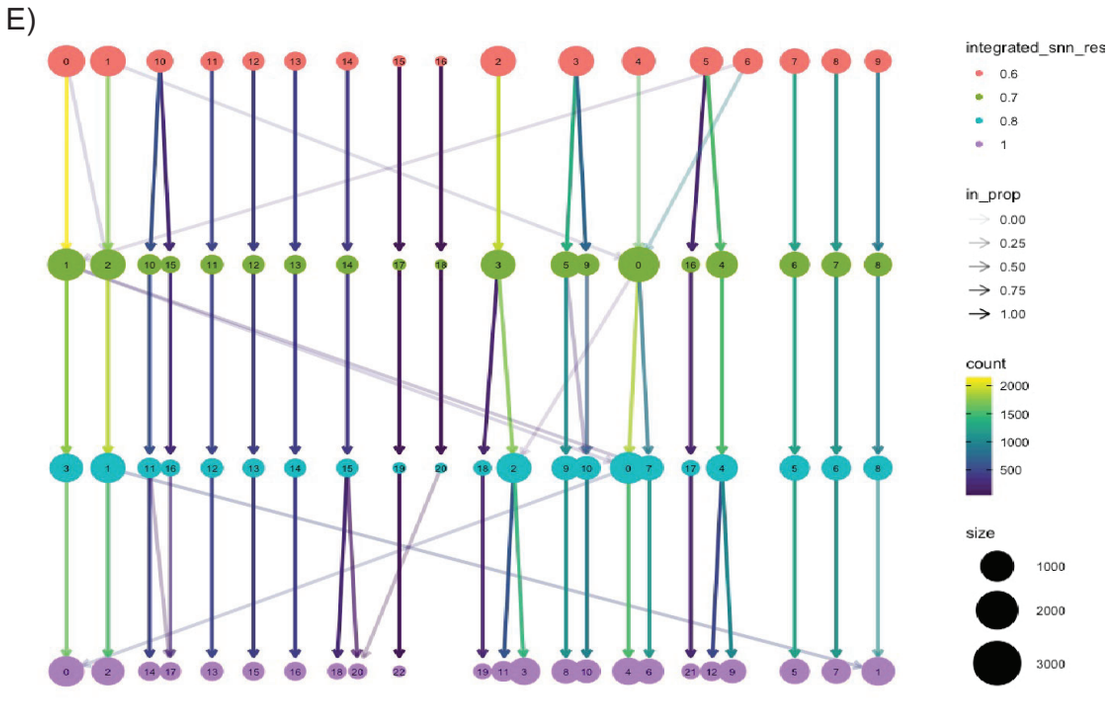
E)
integrated_snn_res
0.6
0.7
0.8
1
in_prop
0.00
0.25
0.50
0.75
1.00
count
2000
1500
1000
500
size
1000
2000
3000

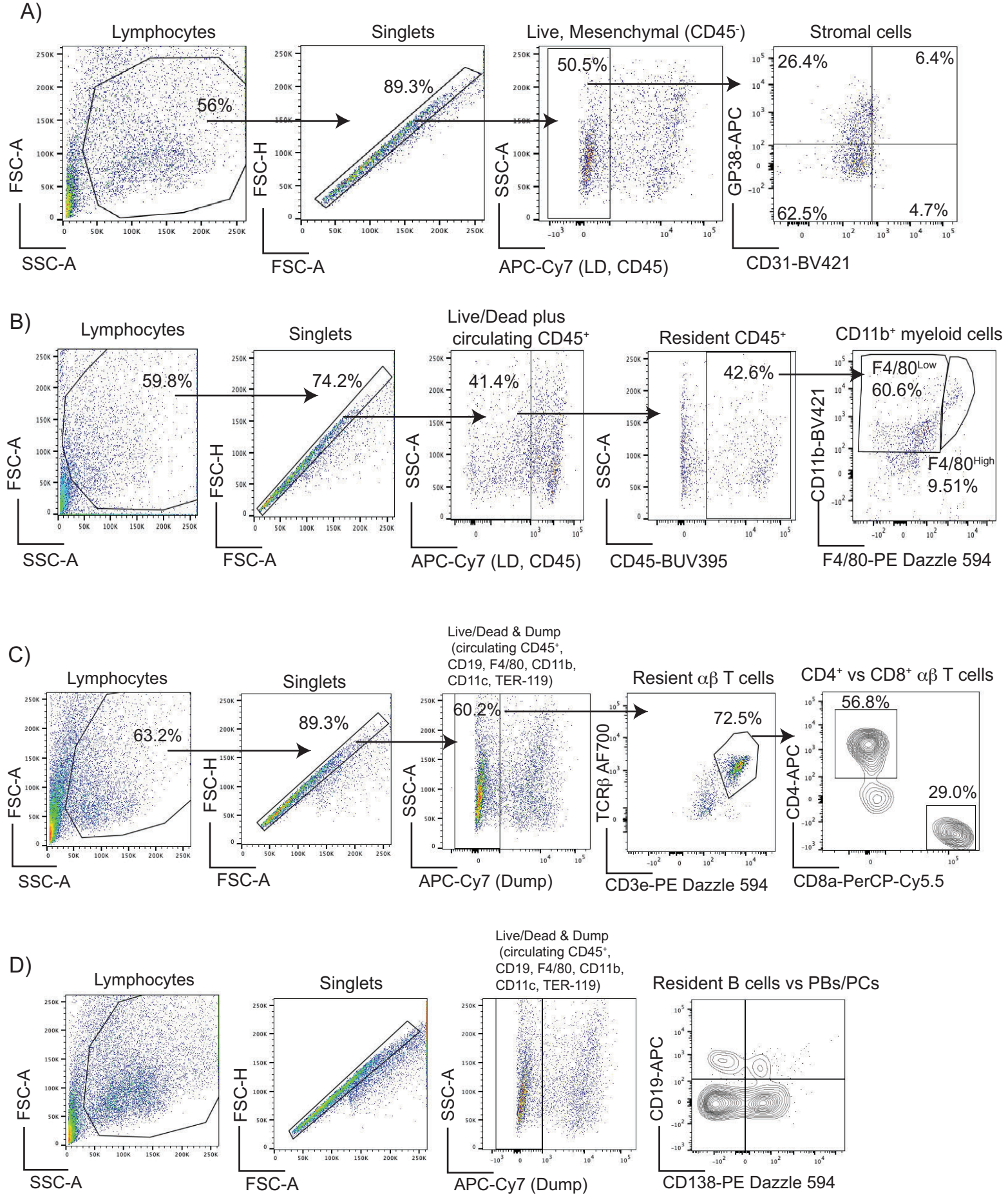
A)
Lymphocytes
56%
FSC-A
SSC-A
Singlets
89.3%
FSC-H
FSC-A
Live, Mesenchymal (CD45-)
50.5%
SSC-A
APC-Cy7 (LD, CD45)
Stromal cells
26.4%
6.4%
62.5%
4.7%
GP38-APC
CD31-BV421
B)
Lymphocytes
59.8%
FSC-A
SSC-A
Singlets
74.2%
FSC-H
FSC-A
Live/Dead plus circulating CD45+
41.4%
SSC-A
APC-Cy7 (LD, CD45)
Resident CD45+
42.6%
SSC-A
CD45-BUV395
CD11b+ myeloid cells
F4/80Low
60.6%
F4/80High
9.51%
CD11b-BV421
F4/80-PE Dazzle 594
C)
Lymphocytes
63.2%
FSC-A
SSC-A
Singlets
89.3%
FSC-H
FSC-A
Live/Dead & Dump (circulating CD45+, CD19, F4/80, CD11b, CD11c, TER-119)
60.2%
SSC-A
APC-Cy7 (Dump)
Resient αβ T cells
72.5%
TCRβ AF700
CD3e-PE Dazzle 594
CD4+ vs CD8+ αβ T cells
56.8%
29.0%
CD4-APC
CD8a-PerCP-Cy5.5
D)
Lymphocytes
FSC-A
SSC-A
Singlets
FSC-H
FSC-A
Live/Dead & Dump (circulating CD45+, CD19, F4/80, CD11b, CD11c, TER-119)
SSC-A
APC-Cy7 (Dump)
Resident B cells vs PBs/PCs
CD19-APC
CD138-PE Dazzle 594

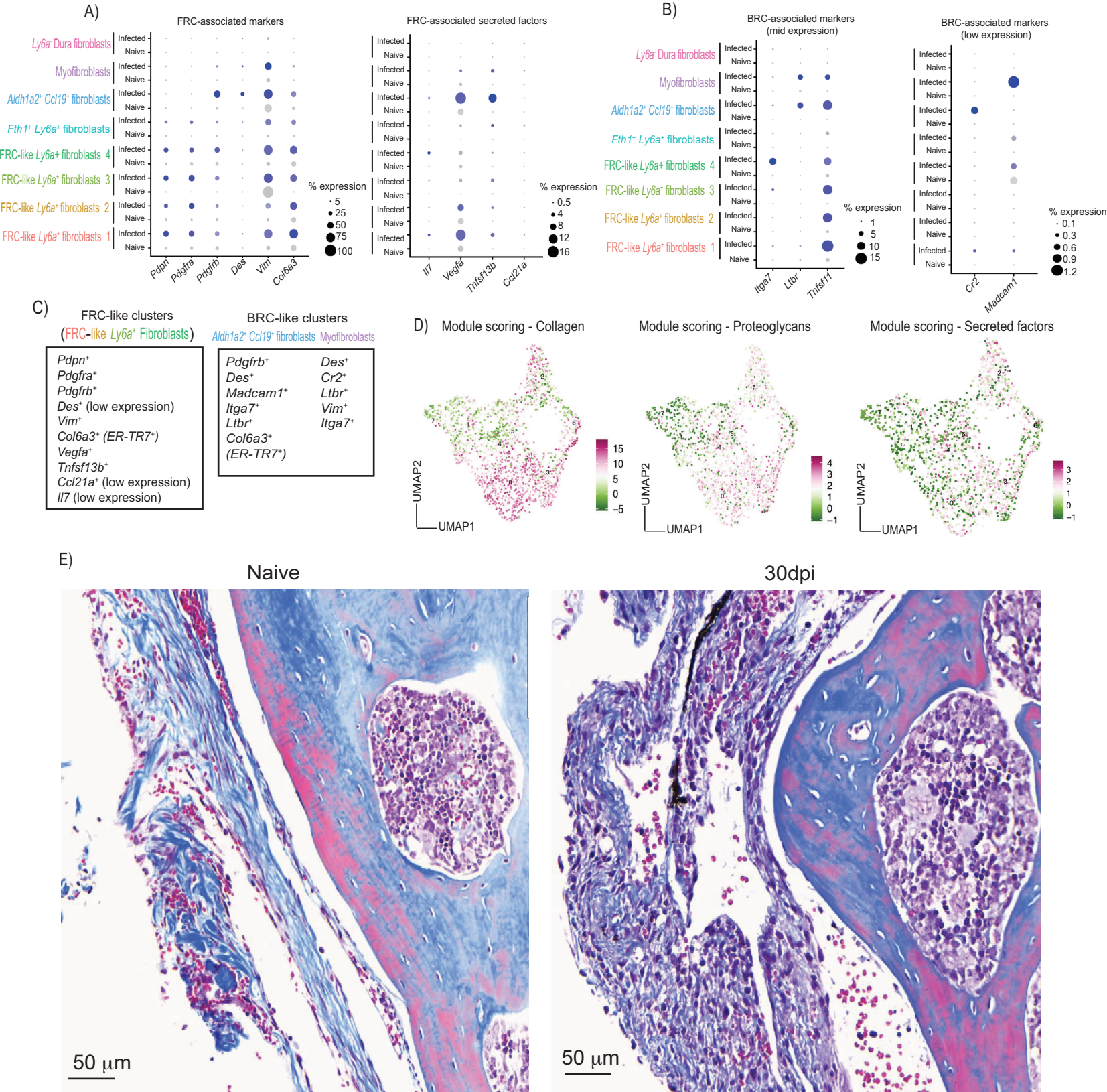
A)
FRC-associated markers
FRC-associated secreted factors
Ly6a- Dura fibroblasts
Myofibroblasts
Aldh1a2+ Ccl19+ fibroblasts
Fth1+ Ly6a+ fibroblasts
FRC-like Ly6a+ fibroblasts 4
FRC-like Ly6a+ fibroblasts 3
FRC-like Ly6a+ fibroblasts 2
FRC-like Ly6a+ fibroblasts 1
Infected
Naive
Pdpn
Pdgfra
Pdgfrb
Des
Vim
Col6a3
% expression
5
25
50
75
100
Il7
Vegfa
Tnfsf13b
Ccl21a
0.5
4
8
12
16
B)
BRC-associated markers (mid expression)
BRC-associated markers (low expression)
Itga7
Ltbr
Tnfsf11
1
5
10
15
Cr2
Madcam1
0.1
0.3
0.6
0.9
1.2
C)
FRC-like clusters
(FRC-like Ly6a+ Fibroblasts)
Pdpn+
Pdgfra+
Pdgfrb+
Des+ (low expression)
Vim+
Col6a3+ (ER-TR7+)
Vegfa+
Tnfsf13b+
Ccl21a+ (low expression)
Il7 (low expression)
BRC-like clusters
Aldh1a2+ Ccl19+ fibroblasts
Myofibroblasts
Pdgfrb+
Des+
Madcam1+
Itga7+
Ltbr+
Col6a3+
(ER-TR7+)
Des+
Cr2+
Ltbr+
Vim+
Itga7+
D)
Module scoring - Collagen
Module scoring - Proteoglycans
Module scoring - Secreted factors
UMAP1
UMAP2
15
10
5
0
−5
4
3
2
1
0
−1
3
2
1
0
−1
E)
Naive
30dpi
50 μm
50 μm

A) Gated on live, CD8⁺ T cells

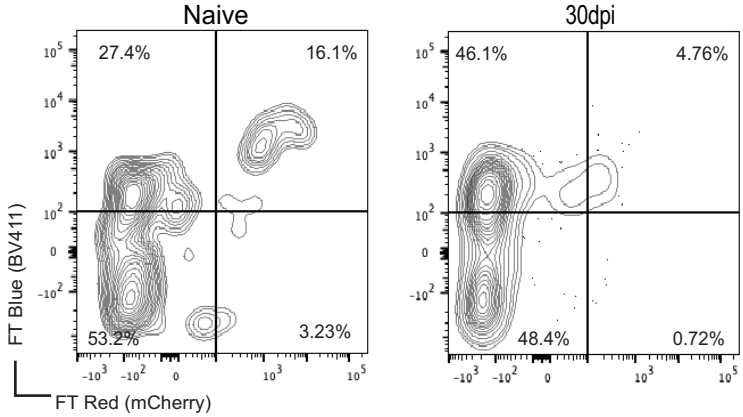

B)

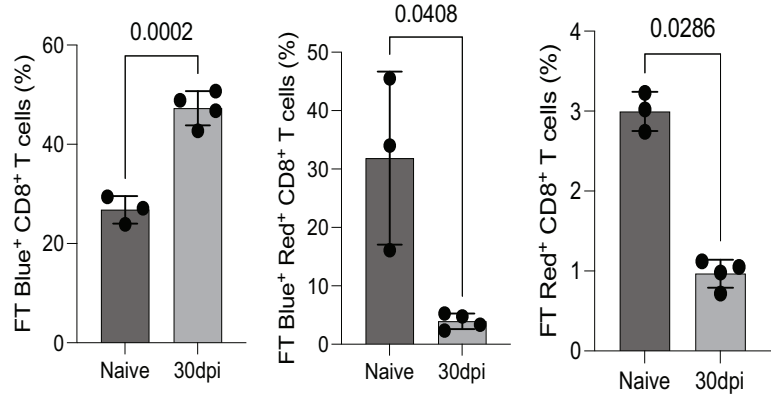

C) Gated on live, CD69⁺ CD4⁺ T cells

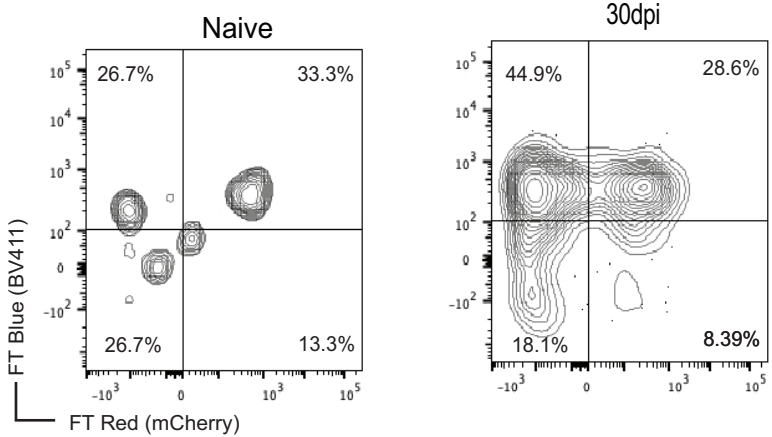

D)

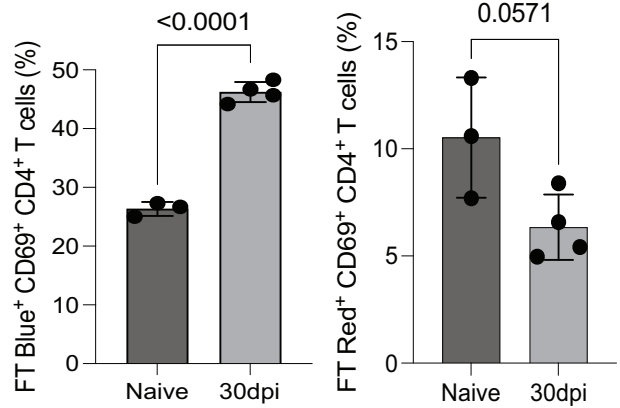

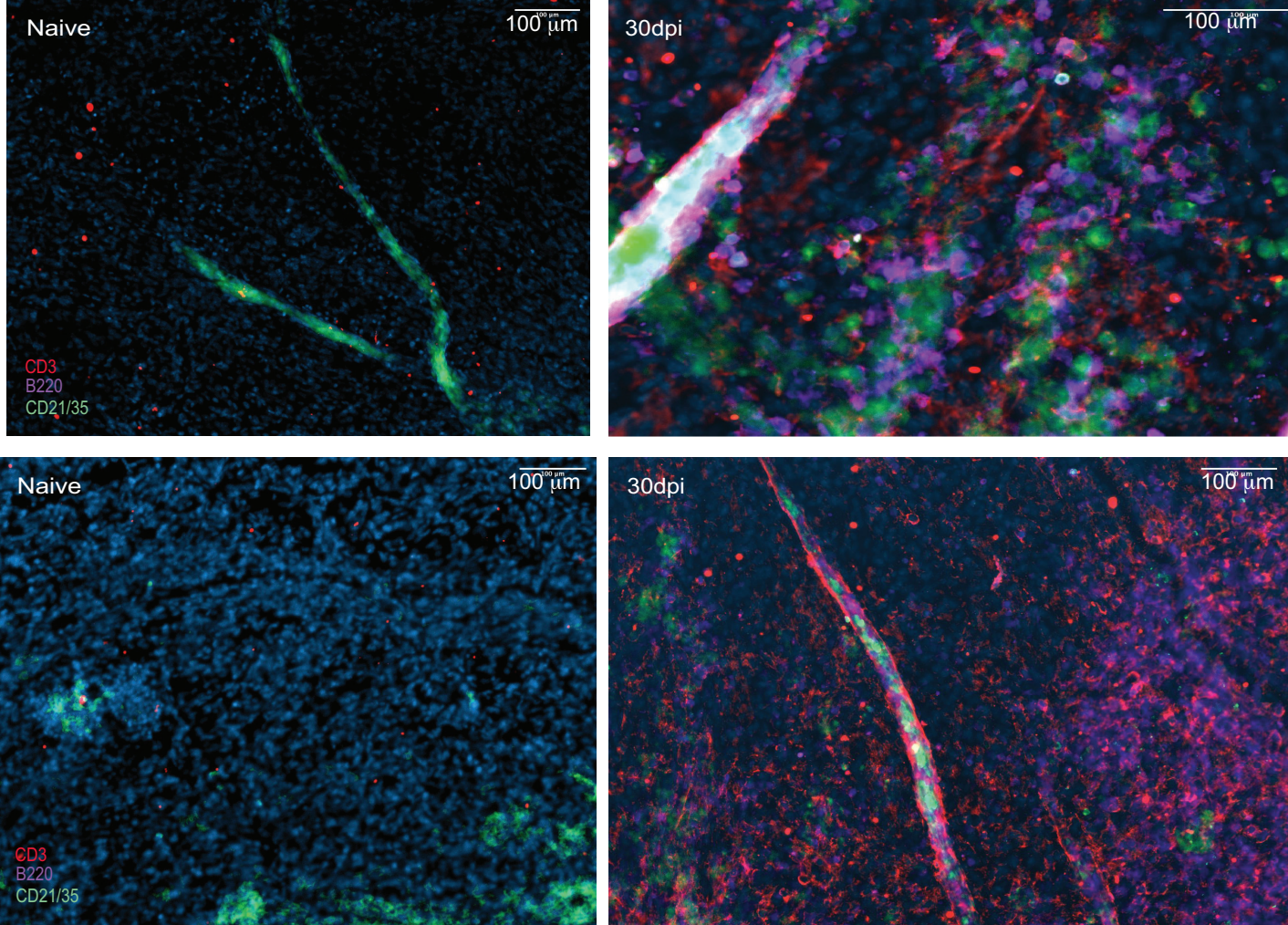
Naive
100 µm
CD3
B220
CD21/35
30dpi
100 µm
Naive
100 µm
CD3
B220
CD21/35
30dpi
100 µm

A)

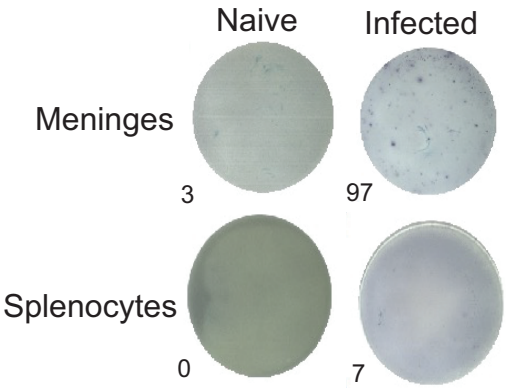

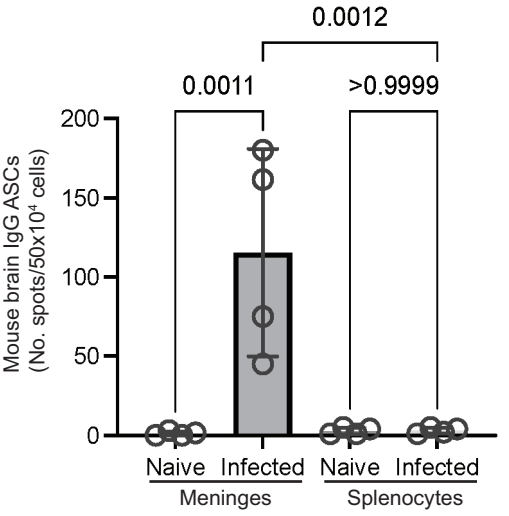

B) Naive brain

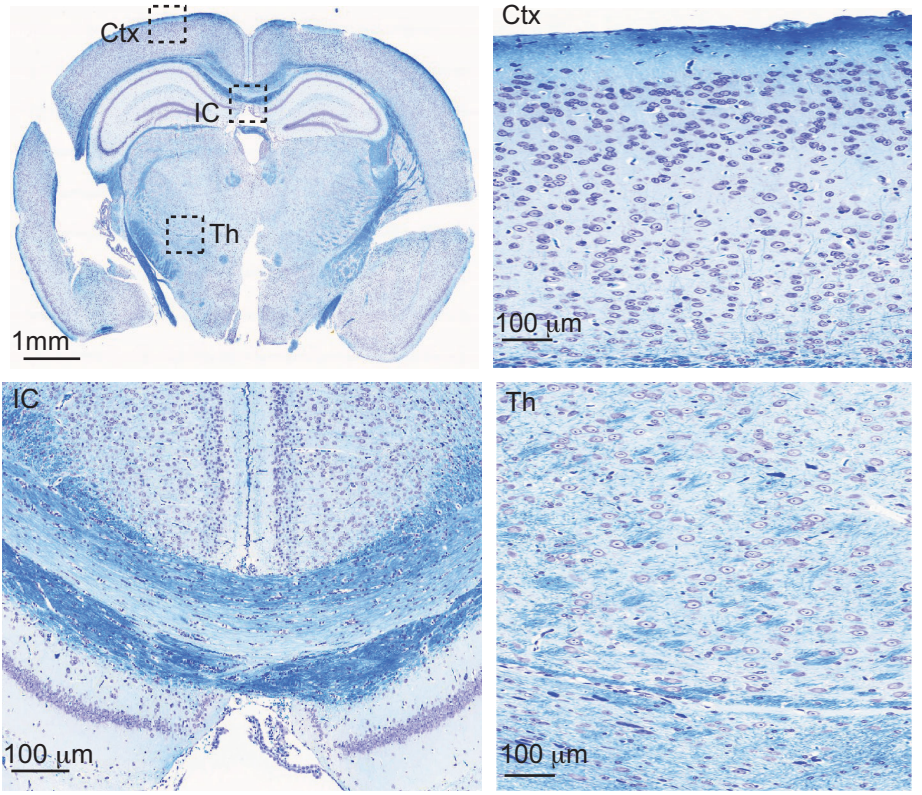

C) Infected brain

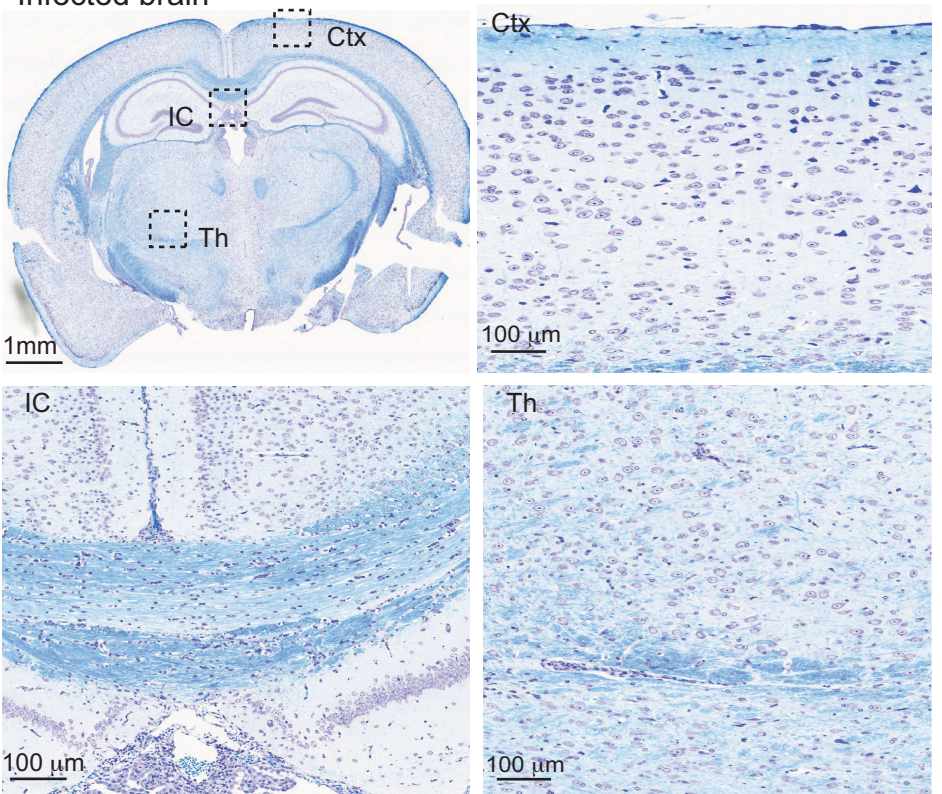

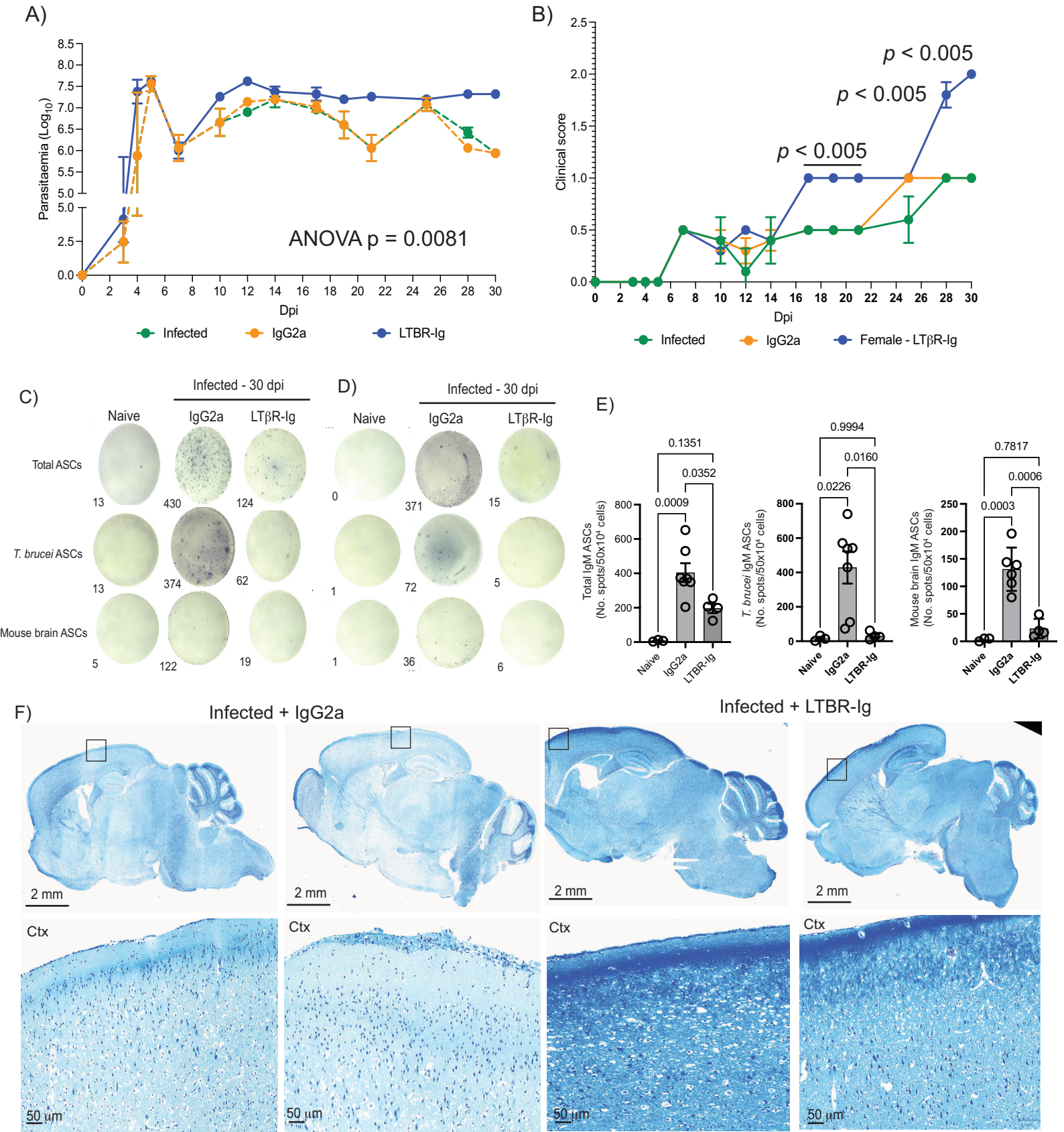
A)
Parasitaemia (Log10)
ANOVA p = 0.0081
Dpi
Infected
IgG2a
LTBR-Ig
B)
Clinical score
p < 0.005
p < 0.005
p < 0.005
Dpi
Infected
IgG2a
Female - LTβR-Ig
C)
Infected - 30 dpi
Naive
IgG2a
LTβR-Ig
Total ASCs
T. brucei ASCs
Mouse brain ASCs
13
430
124
13
374
62
5
122
19
D)
Infected - 30 dpi
Naive
IgG2a
LTβR-Ig
0
371
15
1
72
5
1
36
6
E)
Total IgM ASCs (No. spots/50x10⁴ cells)
0.1351
0.0352
0.0009
T. brucei IgM ASCs (No. spots/50x10⁴ cells)
0.9994
0.0160
0.0226
Mouse brain IgM ASCs (No. spots/50x10⁴ cells)
0.7817
0.0006
0.0003
Naive
IgG2a
LTBR-Ig
F)
Infected + IgG2a
Infected + LTBR-Ig
2 mm
Ctx
50 µm

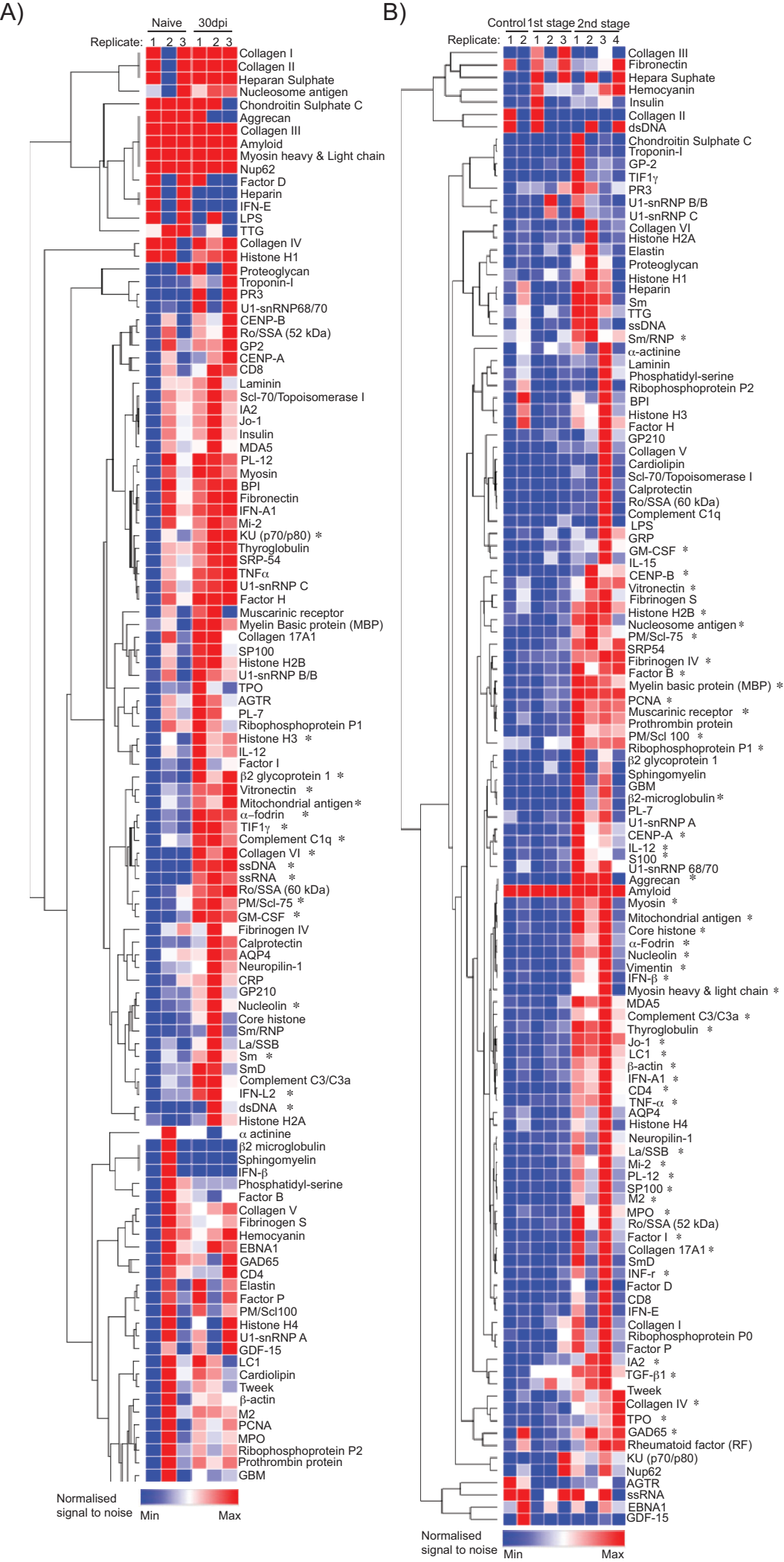
A)
Naive
30dpi
Replicate: 1 2 3 1 2 3
Collagen I
Collagen II
Heparan Sulphate
Nucleosome antigen
Chondroitin Sulphate C
Aggrecan
Collagen III
Amyloid
Myosin heavy & Light chain
Nup62
Factor D
Heparin
IFN-E
LPS
TTG
Collagen IV
Histone H1
Proteoglycan
Troponin-I
PR3
U1-snRNP68/70
CENP-B
Ro/SSA (52 kDa)
GP2
CENP-A
CD8
Laminin
Scl-70/Topoisomerase I
IA2
Jo-1
Insulin
MDA5
PL-12
Myosin
BPI
Fibronectin
IFN-A1
Mi-2
KU (p70/p80) *
Thyroglobulin
SRP-54
TNFα
U1-snRNP C
Factor H
Muscarinic receptor
Myelin Basic protein (MBP)
Collagen 17A1
SP100
Histone H2B
U1-snRNP B/B
TPO
AGTR
PL-7
Ribophosphoprotein P1
Histone H3 *
IL-12
Factor I
β2 glycoprotein 1 *
Vitronectin *
Mitochondrial antigen *
α–fodrin *
TIF1γ *
Complement C1q *
Collagen VI *
ssDNA *
ssRNA *
Ro/SSA (60 kDa)
PM/Scl-75 *
GM-CSF *
Fibrinogen IV
Calprotectin
AQP4
Neuropilin-1
CRP
GP210
Nucleolin *
Core histone
Sm/RNP
La/SSB
Sm *
SmD
Complement C3/C3a
IFN-L2 *
dsDNA *
Histone H2A
α actinine
β2 microglobulin
Sphingomyelin
IFN-β
Phosphatidyl-serine
Factor B
Collagen V
Fibrinogen S
Hemocyanin
EBNA1
GAD65
CD4
Elastin
Factor P
PM/Scl100
Histone H4
U1-snRNP A
GDF-15
LC1
Cardiolipin
Tweek
β-actin
M2
PCNA
MPO
Ribophosphoprotein P2
Prothrombin protein
GBM
Normalised signal to noise
Min
Max
B)
Control 1st stage 2nd stage
Replicate: 1 2 1 2 3 1 2 3 4
Collagen III
Fibronectin
Hepara Suphate
Hemocyanin
Insulin
Collagen II
dsDNA
Chondroitin Sulphate C
Troponin-I
GP-2
TIF1γ
PR3
U1-snRNP B/B
U1-snRNP C
Collagen VI
Histone H2A
Elastin
Proteoglycan
Histone H1
Heparin
Sm
TTG
ssDNA
Sm/RNP *
α-actinine
Laminin
Phosphatidyl-serine
Ribophosphoprotein P2
BPI
Histone H3
Factor H
GP210
Collagen V
Cardiolipin
Scl-70/Topoisomerase I
Calprotectin
Ro/SSA (60 kDa)
Complement C1q
LPS
GRP
GM-CSF *
IL-15
CENP-B *
Vitronectin *
Fibrinogen S
Histone H2B *
Nucleosome antigen *
PM/Scl-75 *
SRP54
Fibrinogen IV *
Factor B *
Myelin basic protein (MBP) *
PCNA *
Muscarinic receptor *
Prothrombin protein
PM/Scl 100 *
Ribophosphoprotein P1 *
β2 glycoprotein 1
Sphingomyelin
GBM
β2-microglobulin *
PL-7
U1-snRNP A
CENP-A *
IL-12 *
S100 *
U1-snRNP 68/70
Aggrecan *
Amyloid
Myosin *
Mitochondrial antigen *
Core histone *
α-Fodrin *
Nucleolin *
Vimentin *
IFN-β *
Myosin heavy & light chain *
MDA5
Complement C3/C3a *
Thyroglobulin *
Jo-1 *
LC1 *
β-actin *
IFN-A1 *
CD4 *
TNF-α *
AQP4
Histone H4
Neuropilin-1
La/SSB *
Mi-2 *
PL-12 *
SP100 *
M2 *
MPO *
Ro/SSA (52 kDa)
Factor I *
Collagen 17A1 *
SmD
INF-r *
Factor D
CD8
IFN-E
Collagen I
Ribophosphoprotein P0
Factor P
IA2 *
TGF-β1 *
Tweek
Collagen IV *
TPO *
GAD65 *
Rheumatoid factor (RF)
KU (p70/p80)
Nup62
AGTR
ssRNA
EBNA1
GDF-15
Normalised signal to noise
Min
Max